ELECTRON CHANNELLING CONTRAST IMAGING OF NITRIDE SEMICONDUCTOR THIN FILMS

A Thesis Submitted to

The Department of Physics

University of Strathclyde

For the Degree of

Doctor of Philosophy

By

Naresh Kumar Gunasekar

December 2012

Declaration of Author's Rights

Signed:

Date:

Abstract

This work reports on the development of a scanning electron microscopy based technique known as electron channelling contrast imaging for characterising extended defects in nitride semiconductors. Extended defects in nitride semiconductors act as scattering centres for light and charge carriers and thus limit the performance of optoelectronic devices. Developing the capability to rapidly analyse extended defects, namely threading dislocation and stacking fault densities without any sample preparation represents a real step forward in the development of more efficient nitride–based semiconductor devices.

In electron channelling contrast imaging, changes in crystallographic orientation, or changes in lattice constant due to local strain, are revealed by changes in grey scale in an image constructed by monitoring the intensity of backscattered electrons as an electron beam is scanned over a suitably oriented sample. Extremely small orientation changes are detectable, enabling small angle tilt and rotation boundaries and extended defects to be imaged. Images with a resolution of tens of nanometres are obtainable with electron channelling contrast imaging.

Vertical threading dislocations are revealed as spots with black–white contrast in electron channelling contrast imaging. A simple geometric procedure was developed which exploits the differences observed in the direction of this black–white contrast for screw, edge, and mixed dislocations for two electron channelling contrast images acquired from two symmetrically equivalent crystal planes. By using this procedure, an order of magnitude reduction in the time required to obtain quantitative information on dislocations is envisaged compared to the presently

available techniques. The use of electron channelling contrast imaging to reveal and characterise basal plane stacking faults and partial dislocations in m–InGaN thin films and quantifying threading dislocations in InAlN thin films is also demonstrated. Preliminary work on combining electron channelling contrast imaging and cathodoluminescence imaging has been demonstrated for the first time to understand the effect of threading dislocations on light emission characteristics in nitride semiconductors.

Acknowledgements

Completing a PhD is beyond doubt an epic event, and I would not have been able to complete this expedition without the aid and support of countless people over the past four years.

I must first express my gratitude towards my advisor, Dr. Carol Trager–Cowan for her support, guidance and continuous encouragement for the successful completion of this thesis. Her attention to detail, hard work, and immense knowledge on electron microscopy is invaluable which has helped in my research work.

I have been very much privileged with my project supervisors, especially my second supervisor Dr. Ben Hourahine for his valuable suggestions throughout my research work with many fruitful discussions on various research topics.

I would also thank Dr. Paul Edwards in sharing his vast expertise on scanning electron microscope and David Clark for helping me to fix the detectors with his magic hands.

I am grateful to Prof. Robert Martin and Prof. Kevin O'Donnell for their fruitful discussions during the group meetings.

I also thank some of my fellow PhD students: Simon, Jochen, Lethy, Michael, Franziska, Jennifer, Aline, Nikhil, Filipo, Electra, Elaine and Martin for their wonderful time during coffee breaks. They each helped make my time in Scotland more fun and interesting.

Over the years, I have enjoyed travelling all over Europe with the aid of Marie Curie fellowship through EU–ITN RAINBOW project which has funded my PhD work. I would like to thank all the members in the RAINBOW project especially

Prof. Pierre Ruterana, Dr. Arantxa Vilalta–Clemente, Daria and Piero for exchanging samples and discussing results.

I sincerely thank many collaborators Prof. Peter Parbrook, Dr. Christof Mauder, Dr. Philip Shields, Dr. Rachel Oliver, Dr. Wang Wang, Dr. Hannes Behmenburg, for providing samples to characterise and Dr. Kwang–Ru Wang for HR–TEM measurements.

I would also like to thank other collaborators namely, Dr. Austin Day, Dr. Aimo Winkelmann, Dr. Gordon England and Dr. Angus Wilkinson by providing valuable suggestions and for helping out in performing and analysing electron channelling contrast images.

Consistent support from my best friends, Regis–Michael, Balaji and my sister Tharani during my difficult times is greatly acknowledged.

I would like to thank my wife Pallavi for her love and support which helped me a lot to complete my thesis.

Lastly, and most importantly, I wish to thank my father Gunasekar–Venugopal and I dedicate this thesis for my mother, Indira who has always been supportive in my life.

Naresh Kumar

6 th December 2012

List of abbreviations

AE	Auger electrons
AFM	Atomic force microscopy
B-W	Black–white
BSE	Backscattered electrons
BSFs	Basal plane stacking faults
CL	Cathodoluminescence
DBR	Distributed Bragg reflector
2–DEG	Two dimensional electron gas
EBIC	Electron beam induced current
EBSD	Electron backscattered diffraction
EBSPs	Electron backscattered diffraction patterns
ECCI	Electron channelling contrast imaging
ECPs	Electron channelling patterns
ELOG	Epitaxial laterally overgrown
FEG	Field emission gun
FSE	Forescattered electrons
HEMT	High electron mobility transistor
HVPE	Halide vapour phase epitaxy
LDs	Lasers diodes
LED	Light emitting diode
MBE	Molecular beam epitaxy

MOVPE	Metal organic vapour phase epitaxy
MQW	Multi quantum well
NPE	Nano pendeo epitaxy
PC	Pattern centre
PDs	Partial dislocations
PL	Photoluminescence
PSFs	Prismatic stacking faults
QW	Quantum well
SE	Secondary electrons
SEM	Scanning electron microscopy
SFs	Stacking faults
STEM	Scanning transmission electron microscope
TDs	Threading dislocations
TEM	Transmission electron microscopy
TMAl	TriMethyl–Aluminum
TMGa	TriMethyl–Gallium
TMIn	TriMethyl–Indium
XRD	X–ray diffraction

Table of contents

Chapter 4 Characterisation of InAlN/GaN heterostructures

Chapter 5 ECCI of GaN thin films grown by nanopendeo coalescence overgrowth

Chapter 1

Introduction

1.1 Motivation:

The main objective of the work presented in this thesis was to develop a rapid and non–destructive structural characterisation technique to study extended defects in III–nitride semiconductors. The motivation for developing such a technique arises due to the fact that reducing extended defects is the key to the optimisation of new electronic and optoelectronic devices. Presently available techniques can be time consuming, destructive and provide limited information on extended defects. Developing the capability to analyse defects and determine their densities rapidly to produce statistically significant data, with negligible sample preparation and without damaging the material under investigation, would represent a significant step forward for the development of high quality material and will accelerate the production of new devices.

The method applied, is the scanning electron microscopy (SEM) based technique known as electron channelling contrast imaging (ECCI). The work described in this thesis was mainly focussed on revealing and identifying extended defects in III–nitride semiconductors with the wurtzite crystal structure. However the technique could also be adapted for characterising a multitude of materials with other crystal structures. In the course of this work, a new method to identify dislocation types in wurtzite materials was demonstrated.

1.2 Thesis overview:

This *first chapter* contains a brief discussion on extended defects in III–nitrides, the growth of III–nitrides and an introduction to SEM and history of electron diffraction. The *Second chapter* describes electron channelling in a scanning electron microscope and the method developed to unambiguously identify different types of dislocations. Using ECCI to reveal stacking faults (SFs) is discussed in *chapter three*. *Chapter four* describes the application of ECCI for characterising III–nitride device structures. The *fifth chapter* describes the application of ECCI for characterising GaN thin films grown by a relatively new growth technique, namely nano pendeo epitaxy (NPE). *Chapter six* discusses the possibility of combining ECCI with another characterisation technique, namely cathodoluminescence (CL) spectroscopy. *Chapter seven* summarises the conclusions of the thesis and suggestions for further work.

1.3 Introduction to III-nitrides:

Compounds of group III elements such as Gallium (Ga), Aluminium (Al) and Indium (In) with Nitrogen (N) are referred to as nitride semiconductors. GaN, AlN, InN are binary compounds, and alloys of these binaries forms ternaries such as InGaN, InAlN, AlGaN and InAlGaN quaternary materials. Hereafter in the rest of the thesis, the term nitrides will be used to refer to the III–nitrides. Nitrides are the only class of commercially available inorganic semiconducting materials with the potential to emit light from the infrared to the UV (with commercial devices available in the green to the ultraviolet part of the spectrum) with direct band gaps ranging from 0.7eV for InN to 6.2eV for AlN [1]. This is shown in Fig. 1.1 where the

band gap energy (E_g) is plotted against the lattice constant (a_0) for nitrides at room temperature.

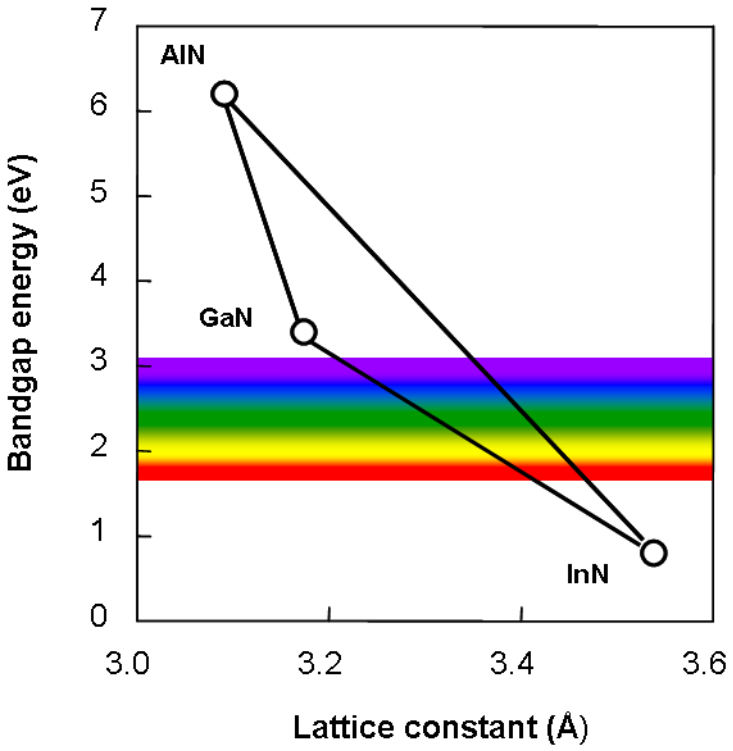

Figure 1.1 Band gap energy (E_g) versus lattice constant (a_0) of wurtzite nitride semiconductors at room temperature.

The band gap is the energy difference between the top of the valence band and the bottom of the conduction band in solids. This is equivalent to the energy required to produce an electron which can move freely within the solid material. The band structure of a material can be used to explain many physical properties of solids, namely electrical conductivity/resistivity and optical absorption, emission. The band gap of a semiconductor is classified into two types, direct and indirect band gap. In

the case of direct band gap, the momentum of electrons and holes is same in both the conduction and valence band, thus an electron can directly recombine with a hole resulting in the emission of a photon. In an indirect band gap, a photon cannot be directly emitted as the electron has to pass through an intermediate state and transfer the momentum to the crystal lattice. Hence direct band gap materials are preferred for solid state lighting. In addition to the direct and large band gap nature of nitrides, their intrinsic high carrier mobility, superior radiation hardness compared to other electronic materials such as Si or GaAs and the capability to form heterostructures have allowed nitrides to dominate the photonic and electronics device market [1].

1.3.1 Applications of nitride semiconductors:

In the last two decades, a wide variety of nitride–based photonic and electronic devices have opened a new epoch in the field of semiconductor research. Nitride semiconductors are mainly used in light emitters, photodiodes and high–speed/high–power electronic devices [2, 3]. For these reasons, research on nitrides has attracted much attention in both the consumer product industries as well as the defence industries.

InGaN and AlGaN based light emitters have revolutionised the field of solid state lighting in decorating buildings, streets and illuminating airport runways. In addition to visible light illumination, ultra high efficient UV light sources are expected to provide new applications in the area of bio sensing and water sterilisation as most biological molecules contain chemical bonds having strong optical resonance within the UV spectral range at approximately 270 nm to 350 nm [4, 5]. There are also future possibilities of using nitrides for commercial solar cell applications [6].

Figure 1.2 shows an overview of current day to day applications and some of the potential future applications of nitrides.

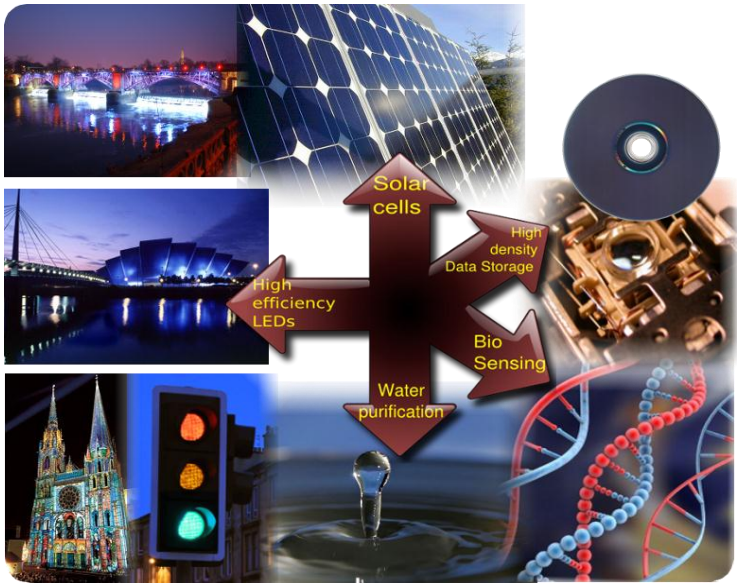

Figure 1.2: Some of the current applications of nitrides in daily life ranging from traffic lights to memory storage devices and future applications including water purification, bio–sensing and solar cells. (*Courtesy of Simon Kraeusel*).

1.3.2 Crystallography of nitrides:

In general, nitrides crystallise in two different polytypes: wurtzite and zincblende. However under very high pressure, the rocksalt structure can also be formed [7]. Thermodynamically (at ambient conditions) the most stable form is the wurtzite crystal structure [3]. The wurtzite structure can be represented as a hexagonal non–primitive unit cell and hence two lattice constants ***'a'*** and ***'c'*** [3]. Figure 1.3 shows the commonly used non–primitive unit cell which contains 6 atoms

of each type and consists of two interpenetrating hexagonal closed packed sublattices, each with one type of atoms as shown in Fig. 1.3. It is clear from Fig. 1.3 that the wurtzite structure has an **ABABAB** stacking sequence along ***c*** direction. In the case of an ideal wurtzite GaN structure, the ***'a'*** and ***'c'*** lattice parameters are 3.188 A° and 5.185 A° respectively at room temperature [8].

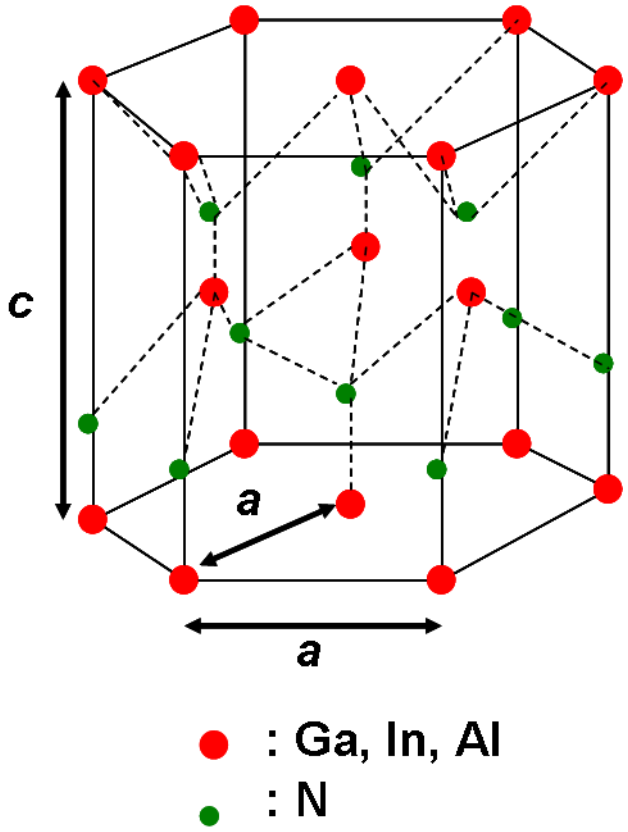

Figure 1.3: Schematic of the unit cell for the wurtzite nitrides.

Among the group V elements, the N atom has the strongest electronegativity, i.e. the tendency of an atom to attract electrons. Due to the large difference in

electronegativity between N and group III elements, a strong ionic bonding component to the covalent bonding between Ga, Al, or In atoms is formed [1, 4].

1.3.3 Optical and electrical properties of nitrides:

Figure 1.4 shows the typical radiative recombination processes occurring in nitrides [9]. Intrinsic optical transitions occur between electrons in the conduction band (CB) and holes in the valence band (VB) including excitonic effects due to the Coulomb interaction. High crystalline quality samples can also exhibits transitions corresponding to free excitons (FE). The bound state of an electron and hole is known as an exciton. Excitons could be bound to neutral or charged acceptors and donors, and in nitrides the two important bound excitons (BE) are neutral shallow donor bound excitons (DBE) and neutral shallow acceptor bound (ABE) excitons. The defect related transition seen in optical spectra from nitrides can be free to bound, bound to free and bound to bound (donor-acceptor) and yellow band luminescence. The band gap energy of nitrides can be estimated from luminescence measurements. Both photoluminescence (PL) and CL spectroscopic techniques can be used to study the optical properties of nitride thin films [10]. Detailed description about CL spectroscopy is given in *chapter six*.

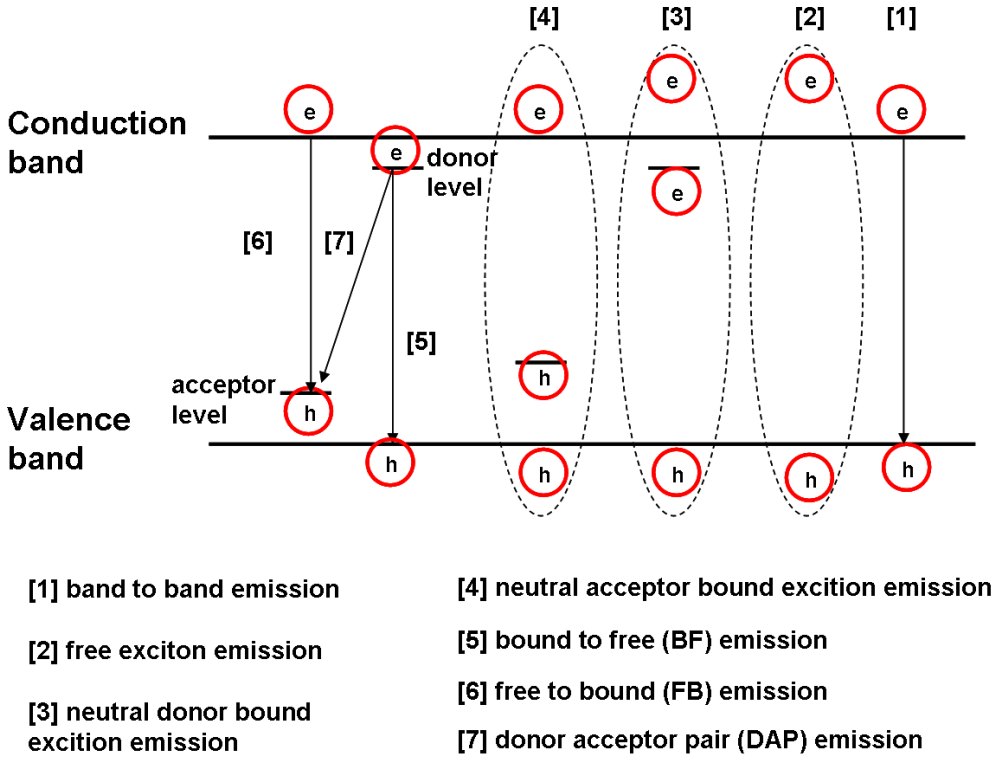

Figure 1.4: Schematic drawing showing various radiative recombination processes in nitrides preferably at low temperatures.

As mentioned earlier, one of the important requirements for materials to be used as light emitters is to have a direct band gap. Nitrides fulfil this requirement with the added advantage of tuning the band gap from 6.2 eV (≈ 200 nm) for AlN to 0.7 eV (≈ 1771 nm) for InN by alloying InN and AlN, as shown in Fig. 1.1 [1] thus forming ternary alloys. GaN has a direct band gap of around 3.5 eV at low temperature (≈10 K) and 3.42 eV at room temperature which makes them ideal for shorter wavelength (UV and blue) optoelectronic devices [11]. AlN is more preferred for deep UV devices due to its much higher band gap (6.2 eV) than GaN. On the other hand, the smaller band gap of InN makes them ideal for potential solar–cell

applications [6]. The high electron mobility of InN (4000 cm^2/Vs) makes InN based heterostructures suitable for high speed electronics applications [4].

1.4 Growth methods for nitrides:

Difference in lattice constant between two materials is known as lattice mismatch and growing materials with different lattice constant can be challenging [4]. One of the technological difficulties for growing nitrides is the limited availability of native bulk substrates which limits the growth of high quality nitride based thin film structures. Another additional difficulty is to achieve uniform p–doping of nitrides and fabrication of good quality ohmic contacts, both of which had held back the progress of GaN based devices [4].

The first report I am aware of on GaN synthesis was by Johnson and his colleagues in 1932 [12]. In the 1970s, growth of epitaxial (a method of growing thin film on a substrate which has crystallographic relation between them) GaN layers were reported and the first GaN blue light emitting diode (LED) was fabricated by Pankove et al. in 1971 [13]. In 1989, Amano et al. [14] reported p–doping and the growth of high quality epilayers, being made possible by using an AlN or GaN buffer layer grown on to the substrate prior to the growth of the GaN layers.

Even after 80 years, the growth of nitride semiconductors is still an ongoing research area, whose aim is to produce cost effective, high quality materials for the optoelectronics and electronics industries. However, recent advancements in growth techniques such as epitaxial laterally overgrowth (ELOG) [4], and nano pendeo epitaxy (NPE) [4, 6] seems to be promising for growing nitrides with superior material quality. Brief description of these growth methods are given in *chapter five*.

Still in order to utilise the full potential of nitrides, growth of nitride semiconductors has to be optimised.

The melting point of GaN is around 1700°C; hence growing GaN from a liquid melt is difficult [3]. Thus GaN is mostly grown using halide vapour phase epitaxy (HVPE), molecular beam epitaxy (MBE) or metal organic vapour phase epitaxy (MOVPE). HVPE is the most often used method to produce thick GaN layers with lower dislocation densities for subsequent over–growth by MBE and/or MOVPE by using ELOG or NPE techniques. The growth speed in HVPE is reasonably high (in the range of hundreds of μm/min) when compared to MOVPE which is in the range of tens of μm/min. $GaCl_3$ and NH_3 are used as sources for Ga and N respectively in the HVPE growth method [15, 16].

In the MBE growth method, chemical elements are heated in furnaces to produce directed beams of atoms or molecules that react on a heated substrate in ultra high vacuum (UHV) conditions [3, 4]. The sources for nitrogen can be different, either by using NH_3 (ammonia MBE) or nitrogen plasma (plasma assisted MBE). Owing to its slower growth rate (typically 0.3−1μm/h) and the need for UHV conditions, MBE is not widely used for industrial scale thin film manufacturing. However, it has the advantage of being compatible with a multitude of surface analysis techniques and the growth is generally performed at relatively low temperatures of 650°C–800°C when compared to HVPE or MOVPE [17, 8]. Low growth temperatures are generally preferred for higher InN incorporation for ternaries, quaternaries and to achieve near atomically flat surfaces. All of the samples characterised in the present work are grown by MOVPE and hence this technique is described next in more detail.

1.4.1 MOVPE growth:

Growth using the MOVPE technique involves dynamic flow of gaseous reactants which pass over a heated substrate and react chemically to form the semiconductor layer of interest [18]. MOVPE is extremely popular among thin film growers due its cheaper cost (no UHV chambers required), faster growth rate (about 2 μm/hr for GaN) and the sources of species for growth can be controlled by gas flow regulators when compared to MBE [19]. Various reactor designs have been developed to optimise the laminar flow of gases over a large area for multiwafer growth.

Figure 1.5 shows the schematic of a typical MOVPE growth system of a horizontal shower head model from Aixtron in Germany. Thermodynamically controlled vessels called bubblers contain the organic molecules (precursors) as shown in Fig. 1.5. Each bubbler and gas cylinder is fitted with filters to extract gaseous impurities with gas flow regulators which are computer controlled in present day commercial systems. A series of pipes connect individual cylinders and bubblers to the reactor chamber allowing the flow of gaseous molecules to reach the main growth chamber. The reactor chamber is fitted with induction coils to control the substrate temperature. The typical growth of GaN using MOVPE is governed by the following chemical reaction:

$$\mathbf{Ga\,(CH_3)_3}\ (\text{vapour}) + \mathbf{NH_3} \rightarrow \mathbf{GaN}\ (\text{solid}) + \mathbf{3CH_4}\ (\text{vapour})\ (\text{liquid})\ [16]$$

The intermediate chemical reactions are quite intricate, the kinetics and chemistry of nitrides MOVPE are reviewed in the references [21, 22]. In MOVPE growth, high

growth temperatures (beyond 1000°C) along with high V/III–ratios (more than 1000) and partial pressures in the order of 1–5 $\times 10^4$ Pa and high gas velocities are typically used. Precursors such as TriMethyl–Gallium (TMGa), TriMethyl–Aluminum (TMAl), and TriMethyl–Indium (TMIn) react with NH_3 on the surface of the hot substrate to form nitride layers. Additional sources are also often needed e.g. Silane (SiH_4) for n–type doping or bis–cyclopentadienyl magnesium (CP_2Mg) for p–type doping when producing electronic devices.

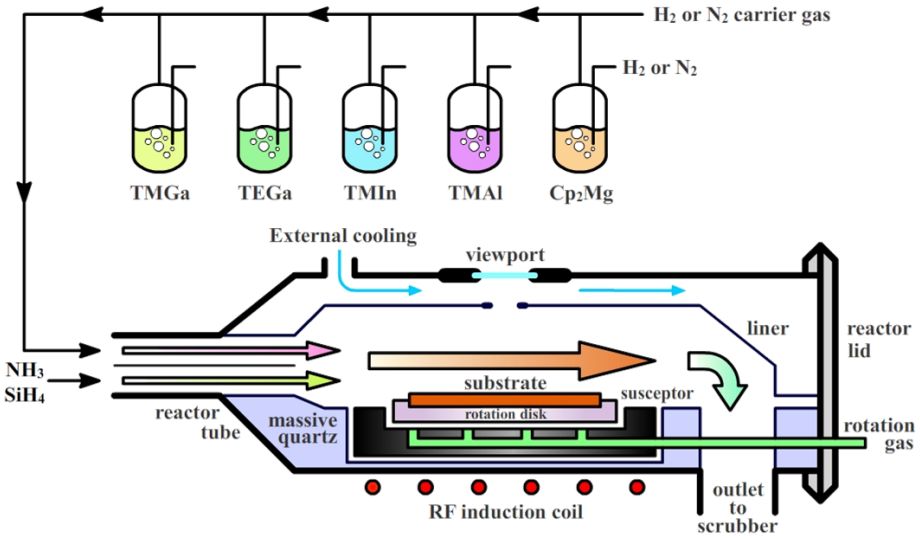

Figure 1.5: Schematic showing various components of a typical MOVPE system from the University of Aachen, Germany (*Courtesy of Dr. Christof Mauder*).

In brief, a typical MOVPE growth process consists of four basic steps. Nitridation by NH_3 for generating a thin AlN layer generally on a sapphire surface, the growth of a nucleation layer at low temperature (between 500°C and 800°C), heat treatment of the nucleation layer (causing nucleation layer to undergo a recrystallisation process) and finally the growth of the main epitaxial layer. Detailed

description on the growth of nitrides can be found in these references [6, 7, 15, and 16].

1.4.2 Substrates used for growing nitride thin films:

Substrates are critical components which are crucial in the electronics industry for processing and fabrication of thin film devices. The following qualities are essential in choosing appropriate substrates for accelerating the production of nitride based devices [1-5, 8, 15, 16, 21, and 22].

1. Low lattice–mismatch between the substrate and the layers for the devices.
2. High thermal conductivity and coefficient of thermal expansion.
3. Cost.
4. Availability with respect to size.
5. Crystal quality and residual defect density.
6. Surface, mechanical and chemical properties.
7. Wafer bowing.

Some of the commonly used substrate materials in the growth of nitrides are SiC, Sapphire, Si and γ–$LiAlO_2$. Table 1.1 shows some of the properties of the widely used substrates for growing nitrides.

Table 1.1: Lattice constants and thermal expansion coefficients (α_c and α_a) of the most commonly used substrates for the growth of GaN [8, 16].

Material	**6H-SiC**	**Al_2O_3**	**Si**
a lattice constant [A°]	3.0806	4.758	5.43
c lattice constant [A°]	15.1173	12.991	5.43
$\boldsymbol{\alpha_c}$ (Thermal expansion co-efficient) $10^{-6}[K^{-1}]$	4.7	8.5	3.59
$\boldsymbol{\alpha_a}$ (Thermal expansion co-efficient) $10^{-6}[K^{-1}]$	4.2	7.5	3.59
Lattice mismatch (%)of GaN with	3.3	14.8	16.9

Higher thermal conductivity materials such as BN and diamond are also being studied as possible substrates to grow nitride thin films. ZnO is also thought of as a potential substrate for nitrides. Although GaN is an obvious choice as a substrate material, neither conducting nor semi–insulating GaN substrates are available with sufficient size and at a reasonable price. Growing GaN on Si has recently become popular due to its ease in fabricating with the existing Si technology based platform of the microelectronics industry. In addition to free standing GaN, Si; SiC and sapphire are the most commonly used substrates for growing commercial devices. All the samples characterised in this thesis are either grown on sapphire or SiC.

Semi–insulating SiC is one of the most attractive substrate materials for nitrides due to a favourable combination of lower lattice mismatch and higher thermal conductivity. It is available with superior crystal quality and diameters of up to 4 inches. 4H and 6H–SiC polytypes and doped conducting substrates (e.g. n–SiC) are also available. High quality device performance is also achievable using quasi semi–insulating SiC substrates. Although the lattice mismatch with GaN is only

3.3% and the ability to cleave more easily when compared to sapphire, high cost reduces its usage in cheap commercial devices.

On the other hand, sapphire is one of the most widely used commercial substrate material due to its availability and lower in price when compared to SiC. Despite the lattice mismatch of 14.8 % with GaN, it is still widely used as test substrates for optimising growth conditions and the technology to grow nitrides on sapphire has become mature enough in recent years. However, there are some substrate–related issues for making device quality material which are yet to be addressed such as mechanical treatment of thinning sapphire is a great challenge for wafer processing with additional complications due to wafer bowing and extended defects.

1.4.3 Growth planes employed for growing nitrides:

Nitrides lack an inversion plane perpendicular to the c–axis, and hence their surfaces have either a group III–element (Al, Ga, or In) polarity referred as the (0001) plane or a N polarity referred as the (000-1) plane. When the wurtzite crystal structure is strained in the c–direction, the centres of positive and negative charges from the metal (Ga, Al, In)–N bond are displaced from each other, thus electric charges appear at the opposite surfaces of the crystal. This phenomenon is referred as spontaneous polarisation. Thus nitrides grown along [000±1] are generally referred to as polar nitrides. In addition to spontaneous polarisation, a strain induced piezoelectric polarisation also arises during the growth due to the lattice and thermal expansion coefficient mismatch between the thin film and the substrates. Piezoelectric fields affect the efficiency of nitride devices and thus to overcome these

problems, growth along different crystallographic directions has been explored. Figure 1.6 shows the major growth directions and planes that are employed to grow wurtzite nitride semiconductors.

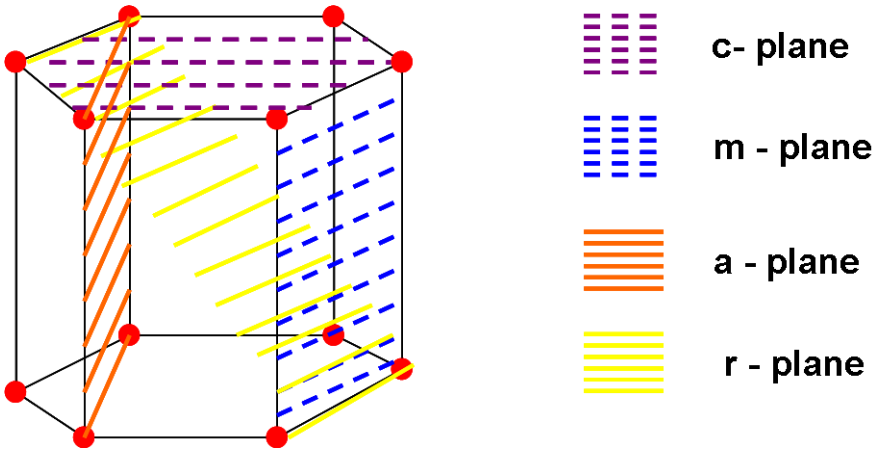

Figure 1.6 Schematic of unit cells illustrating major growth planes that are employed to grow wurtzite nitride semiconductors.

Non-polar orientations are planes perpendicular to the c–plane like the (1-100) plane (m–plane) and the (11-20) plane (a–plane) of the wurtzite crystal structure where the piezoelectric field is zero. Semi–polar orientations are any planes having a tilt angle between 0°and 90° relative to the [0001] direction. It was recently found that InN incorporation in InGaN thin films can be increased by growing on different semi–polar planes which has attracted enormous interest to grow semi–polar nitrides for green light emitters [23].

1.5 Extended defects:

Irrespective of the substrates or the growth plane employed, extended defects such as threading dislocations (TDs), stacking faults (SFs), and grain boundaries are always present in the as–grown layers. Any form of deviation from a perfect crystal lattice can be described as a simple definition for a crystalline defect. Extended defects are conveniently classified based on the number of dimensions in which they depart from the perfect structural positions. They are categorised into line (1–D), surface/planar (2–D) and volume (3–D) defects. Dislocations (1–D), stacking faults (2–D), grain boundaries (2–D) and precipitates (3–D) are commonly observed extended defects in nitrides.

1.5.1 Dislocations:

Dislocations are line defects which are characterised by a pair of vectors: ***u***, the direction along the dislocation line and ***b***, the Burgers vector defined by the Burgers circuit procedure [24]. Burgers circuit gives information on the atomic displacements which is used to explain difference in dislocation types. Figure 1.7 shows the Burger circuit depicted in blue lines and the red arrow and line depicts the ***b*** vector and the dislocation line direction, ***u***. The angle between ***u*** and ***b*** determines the form of the elastic deformation field of dislocations [24]. Edge dislocations have ***b*** perpendicular to ***u*** while screw dislocations have ***b*** and ***u*** parallel or antiparallel. This is shown in Fig. 1.7 for a simple cubic structure where the slip direction and the dislocation line direction are revealed clearly.

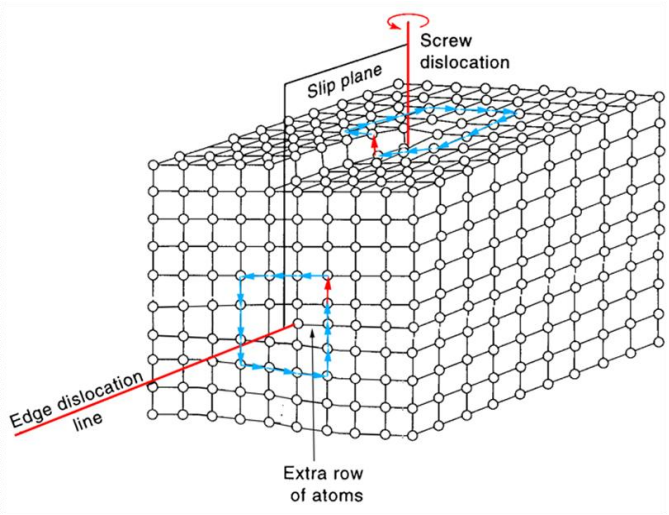

Figure 1.7: Schematic diagram showing both edge and screw dislocations. Blue arrows show Burgers circuits and the red lines show dislocation line direction. From [25].

Edge dislocations arise due to the addition of a lattice plane inserted or removed in the crystal between two adjacent lattice planes. Thus an edge dislocation is produced by shearing a portion of a slip plane in a direction perpendicular to the dislocation line direction (red line in Fig. 1.7). Screw dislocations arise when a part of the crystal is moved with respect to the rest and there is no change in the number of lattice planes. That is it can be produced by a slip over a portion of a plane in which the shear is parallel or antiparallel to the dislocation line direction. Screw dislocations turn the parallel perfect crystal planes into a spiral ramp, thus the name screw dislocation. If the Burgers circuit (blue lines in Fig. 1.7) round the dislocation advances into the crystal, where $\boldsymbol{u}$ is in the same direction of the advancement, then it's a right–handed screw in which $\boldsymbol{u}$ and $\boldsymbol{b}$ are parallel to each other. If the Burgers

circuit round the dislocation advances out of the crystal, then it's a left–handed screw in which ***u*** and ***b*** are antiparallel to each other [24].

Dislocations in nitrides are also referred as threading dislocations (TDs) as they propagate (threading) towards the sample surface. However there are also misfit dislocations which could propagate in the direction parallel to the sample surface. In this thesis only TDs will be discussed. In nitrides, TDs can be classified in to pure screw dislocations, pure edge dislocations and mixed dislocations (combination of screw and edge).

1.5.2 Stacking faults:

Stacking faults (SFs) are planar defects where the periodic sequences of atomic layers are altered. It can be a wrong layer inserted into the periodic sequence or a change in the layer sequence or altered translation between two successive layers. SFs may propagate throughout the entire crystal or affect only a finite region. There are two types of SFs that are commonly observed in nitrides, namely basal plane stacking faults (BSFs) and prismatic stacking faults (PSFs). BSFs are those which propagate through the basal plane of the crystal e.g. (0001) plane in the case of c–plane nitrides and (1-100) in m–plane nitrides. PSFs propagate through the prismatic plane (plane perpendicular to the basal plane) e.g. (1-100) plane in the case of c–plane nitrides. Generally BSFs occur more commonly when compared to PSFs [26]. BSFs can be further classified into intrinsic and extrinsic types (depending on their stacking sequence), and the intrinsic BSF can be subdivided in to type I_1 and I_2. The majority of the observed BSFs in nitrides are I_1 as they have the lowest formation energy [26]. Figure 1.8 shows a schematic of a perfect wurtzite lattice and

a BSF of type I_1. The …**ABABABAB**… stacking sequence for the perfect structure changes to …**ABABCBCBC**… with the boundary plane being terminated on its two sides by a partial dislocations (PDs).

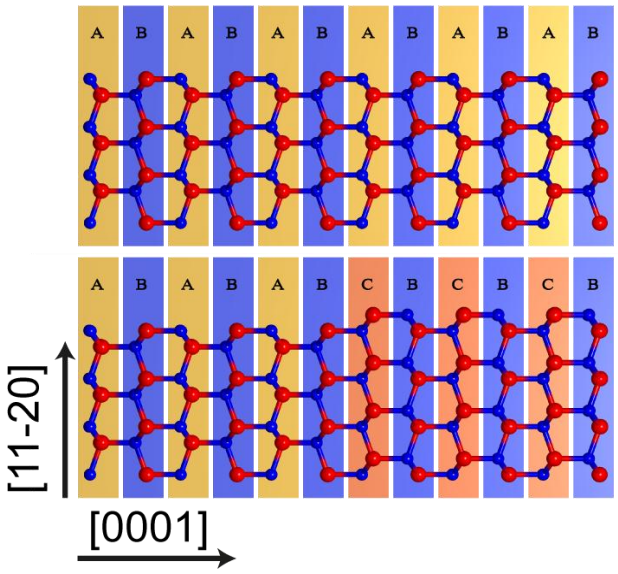

Figure 1.8: Schematic diagram of a perfect wurtzite lattice and the faulted region (I_1 BSF) introduced by replacing the bilayer A (yellow color) to C (red color). (*Courtesy of Simon Kraeusel*).

1.5.3 Grain boundaries:

A grain boundary is defined as an interface between two grains, or crystallites of different orientation. Figure 1.9 shows a schematic representation of grains and grain boundaries. Grain boundaries are classified as low angle grain boundaries or high angle grain boundaries based on the misorientation between the two grains. In low angle grain boundaries, the misorientation angle is generally below 10°, while it's greater than 10° for high angle grain boundaries [24]. Misorientation can be

caused either due to tilt or rotation of the crystal during growth or due to other defects such as twinning, inversion boundaries and voids. In the case of nitrides thin films, the misorientation is lower than 10 °, i.e. generally low angle grain boundaries are present.

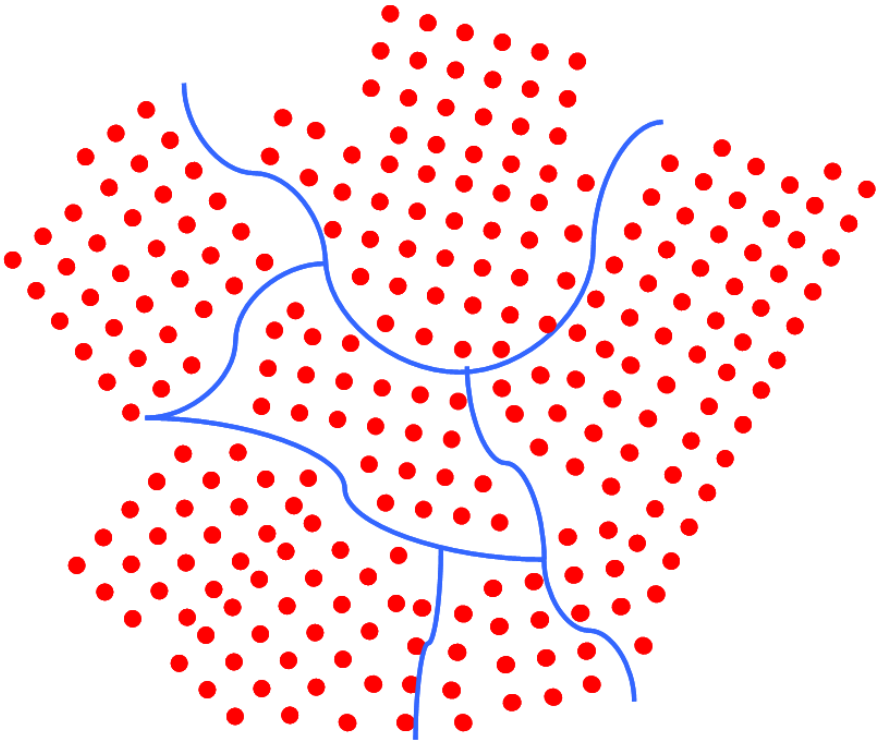

Figure 1.9: Schematic diagram of grains and grain boundary. The blue line represents the grain boundary and the region inside the boundary is an individual grain.

1.6. Defects in nitrides thin films:

Point defects such as vacancies, interstitials, impurities and line defects such as TDs and SFs could be present in nitrides [3]. Characterising extended defects in

nitrides is the main focus of this thesis and hence only they will be discussed in detail. Most of the nitrides growth is on c–plane, (0001) orientation. Figure 1.10 shows different ***b*** directions for TDs in c–plane nitrides. There are two possible ***b*** for a pure screw dislocation, along [0001] and [000-1]. Edge dislocations have six ***b*** along <11-20>, in the case of mixed dislocations; there are twelve ***b*** along <1-123> direction. In addition to TDs, there are also BSFs and PSFs. As mentioned earlier, the majority of the observed BSFs in nitrides are I_1 which involves the removal of one basal plane, displacing the crystal lattice by 1/2 [0001] and an additional slip along 1/3[1-100], which adds up to a displacement vector ***R*** of 1/6 [2-203].

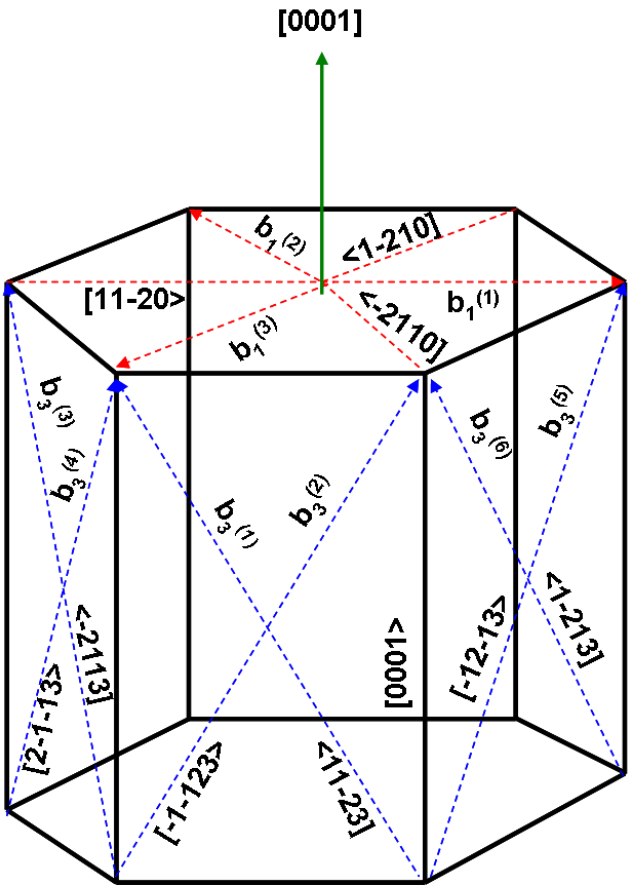

Figure 1.10 schematic illustrating different *b* for screw (green arrow), edge (red arrows) and mixed (blue arrows) TDs in nitrides.

1.6.1 Characterisation techniques for studying extended defects in nitrides:

Characterisation techniques for studying extended defects in nitrides can be broadly classified in to spectroscopic and microscopic techniques with the latter being able to image extended defects. The application of X–ray diffraction (XRD) and two–dimensional XRD reciprocal space maps also provide information on structural properties such as dislocations, grain boundaries, alloy composition from the line widths in XRD measurements [27,28]. Spectroscopic techniques such as PL and CL provide indirect information about extended defects from the peaks observed in the spectrum [29]. PL and CL measurements at various temperatures reveals SFs related emission peaks and variation in alloy fluctuation across the grown film [30, 31]. More information on the applications of CL spectroscopy / imaging is discussed in *chapter six*.

1.6.2 Microscopic techniques for characterising TDs:

At present transmission electron microscopy (TEM) is the best known technique for characterising individual dislocations [32-34]. In TEM dislocations may be identified, i.e., the ***b*** determined, by imaging a cross–sectional sample under a range of different diffraction conditions where a given type of dislocation will appear under one diffraction vector (***g***) but disappear in another. A dislocation is visible in a TEM diffraction image if its strain field has a component in the plane from which diffraction is occurring. Under certain conditions (e.g., the sample must be isotropic) it is also possible to arrange the geometry of the sample in the TEM so

that the $\boldsymbol{g}$ and the $\boldsymbol{b}$ are perpendicular and the scalar product $\boldsymbol{g}\cdot\boldsymbol{b} = 0$. Under such conditions the dislocation will become invisible; this is known as the invisibility criterion [35]. For pure screw dislocations the $\boldsymbol{g}\cdot\boldsymbol{b} = 0$ criterion is sufficient to achieve invisibility; however for dislocations with an edge component it is also necessary for the condition $\boldsymbol{g}\cdot\boldsymbol{b} \times \boldsymbol{u} = 0$ to be satisfied, where $\boldsymbol{u}$ is the edge dislocation line direction, because of the strain field component normal to the slip plane for edge dislocations [35]. Difficulties involved in sample preparation and the localised nature of the information acquired from TEM makes other microscopic imaging techniques such as atomic force microscopy (AFM), and SEM attractive complementary techniques to TEM.

In AFM, TDs in nitride thin films may be identified by small indentations within the step–flow growth surface morphology of the sample due to dislocations threading to the surface. In the case of c–plane GaN, the enlargement of dislocation induced pits by defect selective etching in hot KOH or H_3PO_4 is quite well–known [36]. Alternatively surface treating the sample with SiH_4 is also reported to form pits on defect sites of the sample surface and enhance the contrast in the AFM image [37]. Larger pits which terminate on an atomic step are associated with dislocations having a screw component (either pure screw or mixed dislocations). Pits with smaller size which are not associated with a step termination are identified as pure edge dislocations. An experienced and careful user can also discriminate between pure screw and mixed dislocations from the size and depth of the pits [38]. Due to its destructive nature and ambiguity in finding the individual dislocation types as discussed in reference [43], it becomes increasingly important to find an alternative method for characterising individual dislocation types. The use of SEM in imaging

extended defects in nitrides is very limited and hence in this thesis, the use of SEM to characterise nitrides is discussed in detail.

1.7 Introduction to scanning electron microscopy:

SEM is one of the popular techniques for structural characterisation due to its ease of use and the wealth of information it provides on the material under investigation. From the first ever commercial scanning electron microscope from the Cambridge scientific instruments company in 1965 [39], until today's state of art scanning electron microscopes from companies such as FEI, JEOL, TESCAN, HITACHI etc., they have revolutionised the field of electron microscopy for materials characterisation. Minimal sample preparation or, in some cases, no sample preparation is needed to study bulk as well as nano structures, using a multitude of analysis modes available has been one of the major advantages of using a scanning electron microscope. The work presented in this thesis is based up on using a scanning electron microscope and hence it becomes necessary to explain its working in detail.

1.7.1 Principle and operation of a scanning electron microscope:

There are four main components in a scanning electron microscope which are necessary to produce images from the specimen under investigation: an electron gun, a demagnification unit, a scan unit and a detection unit [40]. A schematic of a typical scanning electron microscope with the major components involved in producing an image is indicated in Fig. 1.11. The final probe (electron spot) size is one of the factors which determine the resolution of a scanning electron microscope and hence

it is important to have a finely focussed electron beam at the specimen [41]. A high quality electron gun produces electrons with a small spatial volume, a small angular spread and the option to vary the electron beam energy. Thermionic emitters such as tungsten filament and LaB_6 are mostly used for general imaging purposes [42]. Currently field emission guns (FEGs) with higher resolution are slowly replacing the thermionic emitters due to their small source size, low electron emission energy spread, high brightness, long–term stability and lifetime [43]. Modern scanning electron microscopes are available with both cold cathode and Schottky FEGs which are briefly described below.

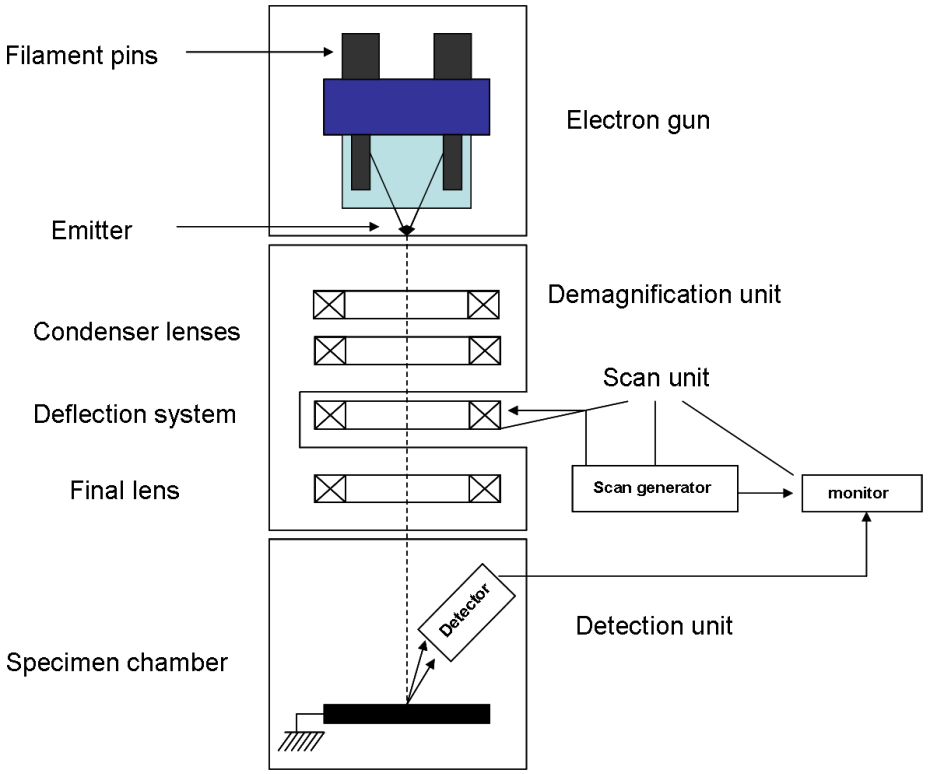

Figure 1.11: Schematic over view of the arrangement of the various components of a typical scanning electron microscope.

A FEG is simply a wire (preferably made of Tungsten) with a sharp point, supported by a hair pin where the tip emits electrons by a quantum mechanical tunnelling process when it is brought closer to a positively biased extraction electrode [44]. High electric fields make electrons tunnel through the potential barrier which is the principle behind the operation of a FEG. In a cold cathode FEG, the filament is not heated and the emission is obtained by placing the filament in a large electrical potential gradient. In the case of a Schottky FEG, a thin layer of ZrO_2 is deposited to reduce the work function, which creates high source brightness where the emission is assisted by heating the filament [45]. In order to avoid contamination on the filaments, the electron gun is always kept under ultra high vacuum typically lesser than 10^{-10} m bar.

Once the electron beam is produced from the source, the beam enters the demagnification unit comprising a series of electromagnetic lenses. The purpose of the electromagnetic lenses in the SEM is to produce a fine beam of electrons to be incident on the sample surface [40]. The focal length of electro magnetic lenses can be defined as a measure of how strongly the electron beam can be converged or diverged. The condenser lens of focal length f_c collects the emitted electrons from the filament and produces a demagnified image at a distance v_1 from the condenser lens. The distance between the electron gun and the condenser lens can be represented as u_1. If the diameter of the filament is d_0, then the diameter of the intermediate demagnified filament image (d_1) is given by the formula $d_1 = d_0 \times v_1/u_1$ [43].

The objective lens of focal length f_0 is used further to demagnify the filament image which now will produce a final probe of diameter d. This can be given by the formula $d = d_1 \times v_2/u_2$ where v_2 is the working distance (distance between the

objective lens to the sample surface) and u_2 is the distance between the demagnified image formed at the condenser lens to the demagnified image produced at the objective lens [43]. By adjusting the current in the condenser lens, u_1, v_1, u_2 and v_2 can be altered. In order to minimise spherical aberration, an aperture is used near the objective lens and hence not all electrons that pass through the condenser lens can enter the objective lens. Hence the current of the final electron beam is also dependent on the aperture size. Suppose if the semi–angle of the electron beam entering the condenser lens is α_1 and the semi–angle of the electron beam leaving the condenser lens is α_2, then the emitted current can be given by the formula $I = Io \times (\alpha_1/\alpha_2)^2$ [43], where I_o is the current of the initial electron beam produced from the gun.

The role of the deflection system is to control the electron beam on the surface of the sample [44]. Typically there are two orthogonal pairs of coils which are set to deflect the beam in opposite direction, thus the beam scans across the specimen but still passes through the optic axis of the SEM.

To image the sample surface, the incident electron beam is moved across the sample in a raster like fashion using the deflection coils under the objective lens as mentioned earlier. At each point on the sample a measure of the number of emitted electrons is detected by the detection system. The next sub–section of this chapter will explain the process involved during the electron specimen interaction and the multimode detection of various signals obtained from a SEM.

The emitted electrons (signals) are detected by a detector system which amplifies the signals and convert them in to electrical voltage. The scan generator signal is then fed to the deflection system and thus an image is acquired by scanning

the electron beam over the sample and the raster scanning of the display system is synchronised with that of the beam on the sample [44]. The magnitude of the magnification in a scanning electron microscope is defined by the ratio of the area of the display system to the area scanned by the beam on the sample. For example if the electron beam is made to scan a area of 10 µm × 10 µm on the specimen and the image formed on the display screen is 100 mm × 100 mm, then the linear magnification will be 10,000 ×. Figure 1.12 shows the picture of a Sirion 200 Schottky FEG–scanning electron microscope (as purchased–without any additional modifications) from FEI instruments which is used in the present work. All the SEM images shown in this thesis were obtained from this instrument with an acceleration voltage of 30 keV unless otherwise stated.

Figure 1.12 picture of the Sirion 200 FEG–Scanning electron microscope from the University of Strathclyde.

1.7.2 Electron–specimen interaction:

As mentioned earlier, the possibility of using a multitude of analysis modes has been one of the major advantages of using a scanning electron microscope. Six types of resultant signals can be detected when an incident electron beam interacts with the sample [44]. Light, X–rays, emitted electrons, transmitted electrons, charge collection (current) and acoustic or ultrasonic waves can be formed during electron–specimen interaction [43]. Employing suitable detectors in appropriate positions will result in different modes of operation of a scanning electron microscope. Figure 1.13 shows the schematic of possible information that could be obtained by using a scanning electron microscope.

Emitted electrons can be both inelastically and elastically scattered resulting in the formation of secondary electrons (SE) and backscattered electrons (BSE) respectively. SE provides topographic contrast where as BSE provide atomic number contrast, revealing regions of the sample composed of different materials [44]. BSE from crystalline materials may also provide information on crystallographic orientation, imaging lattice defects and strain in the sample. The combination of transmission and scanning of the electron beam over the sample in a scanning electron microscope is often referred as low–voltage scanning transmission electron microscopy. Modern scanning electron microscopes are nowadays fitted with a scanning transmission electron microscope (STEM) detector for high resolution imaging due to its larger cross section and smaller interaction volume of the incident electron beam [46].

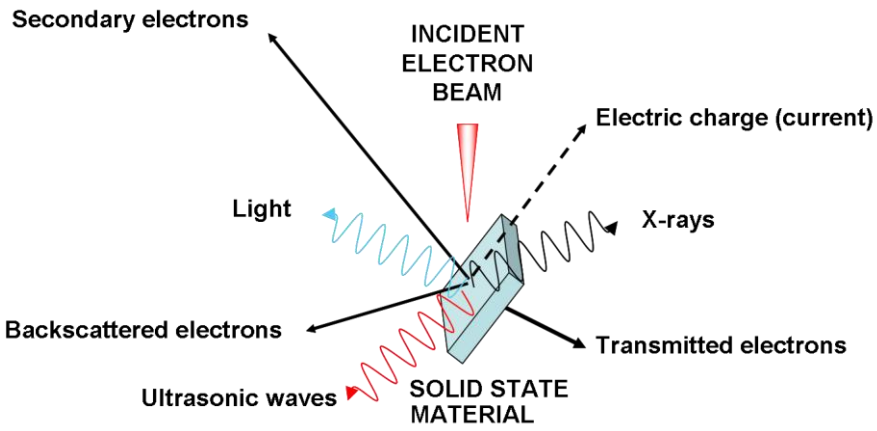

Figure 1.13 Schematic representing the electron–specimen interactions and various information that could be obtained by using a scanning electron microscope.

Energetic Auger electrons (AE) are also emitted when electrons interact with the sample and ionise its atoms, producing vacancies in the inner electronic shells. When the atom rearranges or de–excites by filling the vacancy with an electron from a lower energy shell, it emits energy in the form of X–ray photons or electrons and these electrons are referred to as AE [43, 44]. The kinetic energy of the emitted AE corresponds to the difference between the energy of the initial electronic transition and the ionisation energy of the electron shell from which the AE was emitted. By analysing these energy levels, the type of atoms and its chemical environment can be studied. AE are mainly used in surface studies as their energies are in the range of hundreds of eV and their shorter mean free path makes an UHV environment necessary [44].

Chopping the electron beams may produce acoustic waves in the specimen, which can be used to characterise thermal and elastic properties of materials [47].

The acoustic signals were used as low resolution probes to study bonding integrity in semiconductor devices in 1980s. However quantitative analysis of the images is difficult due to the various parameters included in signal formation, especially for semiconductor materials [47, 48] and hence it is not now commonly used.

Electron beams can also induce currents, especially in semiconductors where electron hole pairs are created due to the incident electron beam [44]. This is known as electron beam induced current (EBIC). The EBIC signals can be used to image semiconductor junctions below the sample surface and also to image electrically active lattice defects which influence the recombination rate of minority carriers [49]. However, sample preparation can be quite tricky, as two electrical contacts are required to perform EBIC measurements.

Light emission by electron bombardment is known as CL, which can be exploited to study a multitude of materials ranging from semiconductors to minerals and also some organic molecules [50]. By introducing a light collection system, a spectrometer and a detector to the electron microscope, CL spectroscopy can be performed [44]. Detailed description of CL spectroscopy is given in *chapter six*.

Characteristic X–rays are also produced as a result of electronic transitions occurring between the inner core levels of the atoms due to inelastic scattering when electron beam interacts with the specimen under investigation [44]. The energy or (wavelength) of the emitted X–rays is unique to the particular element that was ionised to produce them [49]. Thus elemental composition of alloys can be analysed using the emitted X–ray beams. Most modern electron microscopes provide an option for wavelength dispersive X–ray spectroscopy or energy dispersive X–ray spectroscopy. Based on the individual's requirement, a custom built scanning

electron microscope can be built to perform structural, optical and electrical characterisation all in one instrument. Thus a scanning electron microscope becomes an obvious choice for rapid structural characterisation for variety of materials.

It is also important to know the origin and the depth from which the electrons are emitted especially in the case of thin films composed of different materials. The electron specimen interaction is a complex phenomenon and it is intricate to solve by general analytical methods [44]. Monte–Carlo simulations are generally employed which are based on probability events to determine the energy loss of the electron beam and the penetration depth of electrons with specific energy [51-53].

1.7.3 History of electron diffraction:

An electron has particle and wave duality; hence aspects of both the particle and wave nature could be used to explain electron diffraction. Electron diffraction dates back to 1927 from independent experiments of Davisson and Germer from Bell laboratories [54] and Thomson from the University of Aberdeen, leading to the award of a Nobel Prize to both Davisson and Thomson in 1937 [55]. Their invention led to the study of crystal structures using electron beams and electron crystallography became highly popular among crystallographers. The earliest electron diffraction patterns from transmitted and backscattered electron beams in mica and calcite crystals were first observed by Shoji Nishikawa and Seishi Kikuchi in 1928 [56, 57]. This later became what is know as electron backscattered diffraction (EBSD) and the patterns are generally referred as electron backscattered diffraction patterns (EBSPs) or Kikuchi patterns. The EBSD technique is most often used by geologists and metallurgists, in recent times it has also been used for

characterising semiconductors [58, 59]. In 1960s electron channelling in a scanning electron microscope attracted the attention of the electron microscopy community because it could be used to rapidly identify if a given material is crystalline or amorphous [44]. A detailed description of the history and principles of electron channelling are given in *chapter two*.

1.8 Summary:

The thesis outline, the fundamental properties of nitrides relevant to the present work was discussed in this chapter. Brief descriptions of extended defects in nitrides and the characterisation techniques used for their analysis such as TEM and AFM were also given, with the importance of SEM and its working was also explained.

Chapter 2

Rapid non–destructive analysis of TDs in GaN using ECCI

2.1 Introduction:

The reduction of extended defects such as TDs is necessary for optimising new devices, as TDs act as scattering centres for light and charge carriers and give rise to nonradiative recombination and to leakage currents, severely limiting device performance [60-62]. Thus developing the capability to analyse TDs and determine their densities rapidly and without damaging the material under investigation is important for the development of new nitride based devices.

In this chapter, the principle of electron channelling and the experimental setup to perform ECCI in an FE–SEM is described. A new method for identifying TDs types using ECCI without the need to perform dynamical simulations of channelling contrast is then explained in detail [63].

2.2 History of electron channelling:

The variation of the backscattering intensity by changing the crystal orientation was reported by Laponsky and Whetten in 1959 [64] followed by Dekker in 1960 [65] which led to the production of electron channelling patterns (ECPs) in a

commercial scanning electron microscope by Booker and Coates in 1967 [66, 67] (a detailed description of ECPs is given in the next section). The acquisition of the ECPs became increasingly important due to the speed in finding the amorphous or crystalline nature of the material under investigation [68-70]. Crystal orientation and lattice parameter were also determined using ECPs with minimal sample preparation [68, 71-73]. Some of the pioneering work on ECPs and its applications were performed by Hirsch, Joy, Newbury and Humphreys in 1970s [68].

The first observation of extended defects in thin specimens recorded with BSEs in a scanning electron microscope was performed by Clarke in 1971 [74] followed by Stern and Kimoto in 1972 [75]. The importance of using a FEG was realised from their work and the first observation of dislocations using a FEG and energy filtering in bulk single crystals (molybdenite) was obtained by Pitaval et al in 1976 [76-78].

The term electron channelling contrast imaging (ECCI) was first used by Morin et al in 1979 [79] and they were able to image extended defects in semiconductors (Si) using ECCI. It was the first ever published work which discusses both ECCI and ECPs using a scanning electron microscope. Seminal work from Joy, Newbury for metals [68], Wilkinson et al to image dislocations in $Si_{1-x}Ge_x$ thin films and improvement in detector geometries have opened up the possibilities of using ECCI for variety of materials [80, 81].

Trager–Cowan and co–workers [82] were the first to apply ECCI to image TDs in nitride semiconductors. Picard et al have also used ECCI to investigate SiC [83], GaN [84, 85] and $SrTiO_3$ [86]. However until now there has been no quantitative method for characterising individual TDs in nitrides and identifying their

types using ECCI. The work discussed in this thesis takes ECCI a step further for characterising nitride semiconductor thin films, and opens up new possibilities for advanced materials characterisation.

2.3 Principle of electron channelling:

Since an electron has particle and wave duality, aspects of both the particle and wave nature can be used to explain electron channelling. In the case of crystalline materials, the BSE probability depends on the proximity and the angle of incidence of the incident electron with respect to the atomic nuclei which are involved in the scattering process. The packing density of the atoms appears to be reduced for certain angles of incidence, when the atoms line up with the incident electron direction, leading to a reduction of the BSE emission. Thus by either changing the angle of incidence of the electron beam or by changing the orientation of the crystal, the BSE intensity can be varied [64, 67-68]. Figure 2.1 shows a schematic of the direction of incident electrons and the atomic positions where some of the incident electrons channel between the atomic planes and some of them are backscattered or diffracted depending on the atomic positions.

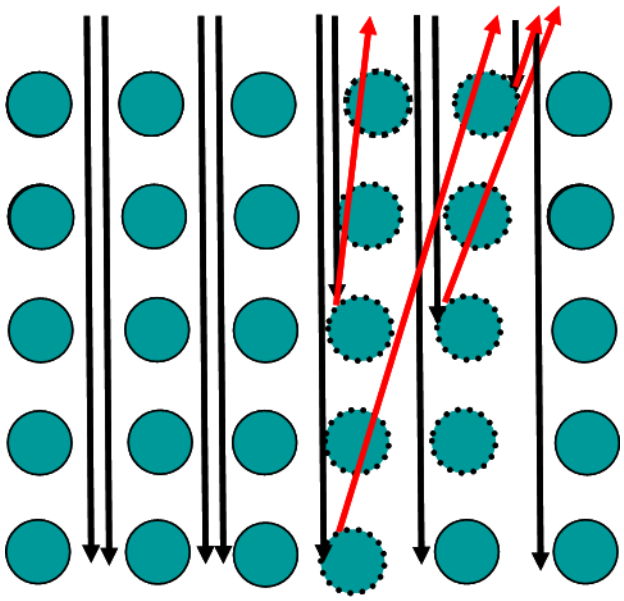

Figure 2.1: Schematic diagram showing the direction of incident electron (black arrows) and atoms (blue circle) where some of the incident electrons channels between the atomic planes and some of them are backscattered or diffracted (red lines) because the atomic positions are slightly displaced in those regions (marked by dotted circles).

This simple model is plausible in explaining electron channelling when the incident electron beam energy is high, but in the case of an incident beam energy in the range of tens of kilovolts (typical operating voltages in a SEM); the wave nature becomes significant. In the case of waves, the flux of the incident electron beam travelling through the crystal lattice can be represented mathematically as a number of standing waves, referred to as Bloch waves. Each of the Bloch waves has the periodicity of the crystal lattice. These Bloch waves are sets of plane waves propagating through the crystal from the top surface. The square of the amplitude of these Bloch waves at any point represents the local current density. The Bloch waves

can be simply classified into type I and type II based on the current travelling in the specimen. Type I Bloch waves are strongly backscattered since they are in close proximity to the atomic nuclei as the maxima of the Bloch waves lie along the columns of the atomic nuclei in the crystal. In the case of the type II Bloch waves, the electrons weakly interact with the atomic nuclei, as their intensity maxima lie halfway between the atomic planes [68, 70]. This is schematically shown in Fig. 2.2.

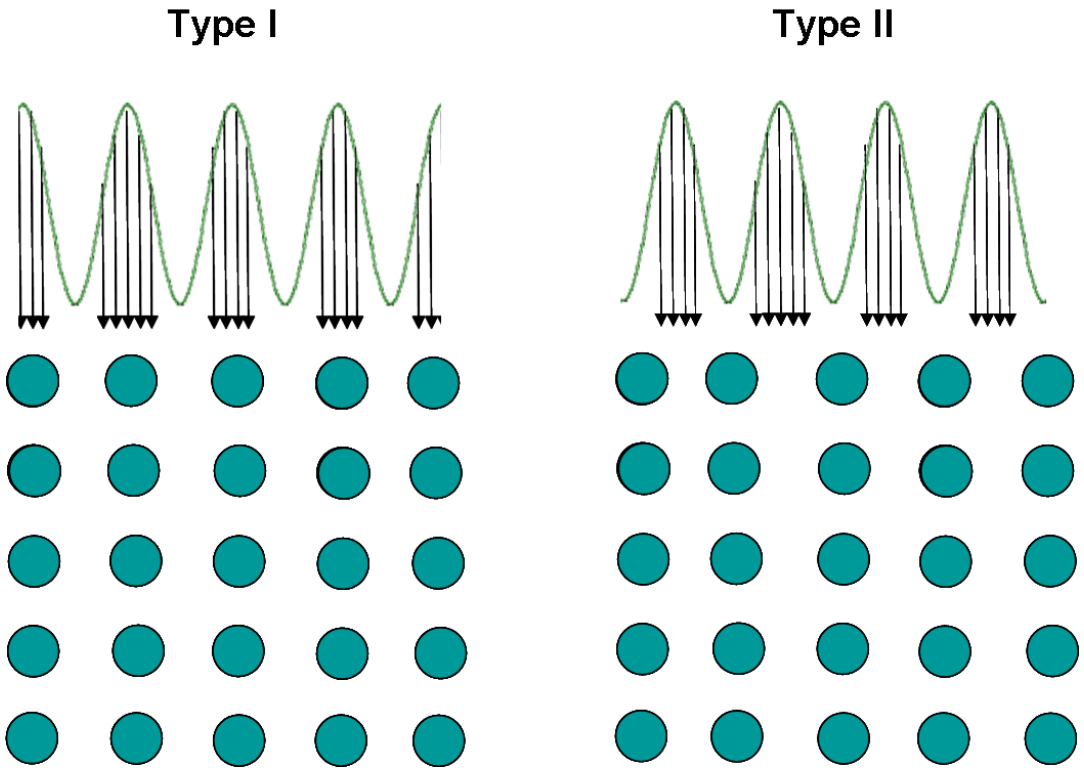

Figure 2.2: Schematic diagram showing the Bloch wave representation of standing currents in a crystal.

The ratio of the intensities of the type I and type II Bloch waves can be varied by changing the angle between the incident beam (θ) to that of crystal lattice (d is the lattice spacing) thus varying the BSE intensity. The two waves are of equal intensity at the Bragg condition ($2d \sin \theta = \lambda$) for diffraction where λ is the wavelength of the incident electron [80]. However, when $\theta < \theta_b$ (θ_b is the Bragg angle), type I Bloch waves dominate the overall intensity and when $\theta > \theta_b$, type II Bloch waves dominates. This is shown in Fig. 2.3.

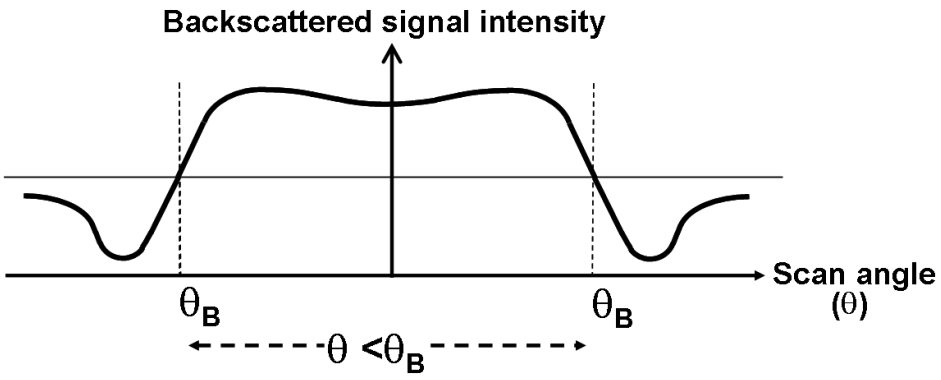

Figure 2.3: Schematic showing the effect of incident beam geometry on the backscattered electrons signal intensity [68, 70].

Contrast from electron channelling can be used in two modes of operation [70]. The first of these is the acquisition of ECPs which allows the set of planes from which the electrons are diffracted to be selected. This procedure is referred to as selecting g. This is analogous to selecting diffraction conditions in TEM (see *chapter one*).

An ECP is obtained when changes in the BSE intensity are recorded as the angle of the incident electron beam is changed relative to the surface of a single crystal area of the sample–this is referred to as *rocking* the beam. When an image is acquired at the lowest possible magnification, as the beam is scanned over the sample, it changes its angle with respect to the surface of the sample (in the present work it is around ± 2.5°) allowing an ECP to be obtained. This is generally referred to as a wide area or large area ECP as shown in Fig. 2.4 [67-70]. However, in principle by mechanically rocking the sample stage or by changing the current in the scan coils, the objective and in the condenser lenses in the SEM, small area or selected area ECPs can also be acquired [67, 87-88]. In the present work, wide area ECPs were acquired as there was no provision available to obtain small area ECPs. When the beam is rocked over the sample, different planes of the crystal satisfy the Bragg condition, giving rise to the appearance of overlapping bands of bright and dark lines (Kikuchi lines due to inelastic scattering [89]) superimposed on the image of the sample; this is the ECP, as seen in Fig. 2.4. The ECP is a 2–D projection of the crystal structure, with the Kikuchi lines corresponding to different planes in the crystal. Note that channelling and diffraction are equivalent, i.e., they are different methods of describing the same physical phenomenon. The basic difference between electron backscattered diffraction patterns and ECP is, the former gives information on the specimen orientation relative to the detector and the later gives the specimens orientation relative to the incoming electron beam. Both these patterns are related by the reciprocity principle [63, 67-70, 79-82, 90].

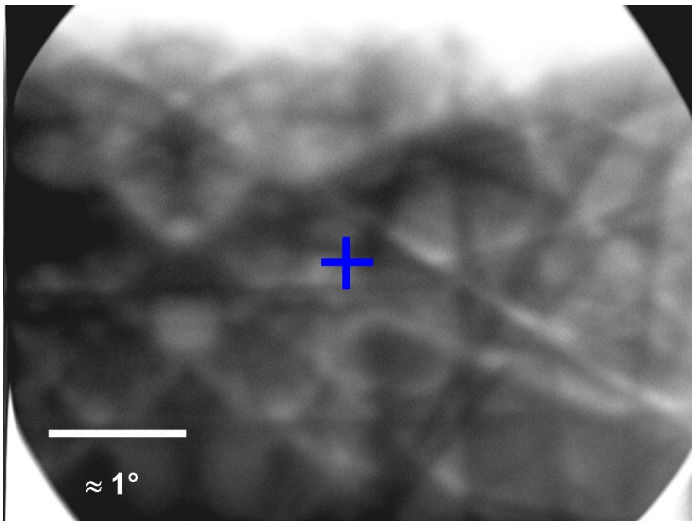

Figure 2.4 ECP from a GaN thin film acquired at 30 keV. The cross on the ECP marks the Pattern centre.

The point on the ECP around which the electron beam is *rocked* is referred to as the pattern centre (PC). This is shown as a blue cross in Fig. 2.4. If a single Kikuchi line intersects the PC, this is the plane which will provide channelling contrast in the electron channelling contrast image. Changing the tilt and/or rotation of the sample allows a different ***g*** to be selected. If only one Kikuchi line intersects the PC, this is referred to as a 2–beam diffraction condition (i.e., only the incident beam and the diffracted beam from one plane determine the contrast in the electron channelling contrast image. In practice it is extremely difficult to achieve exact 2–beam conditions, but a near 2–beam condition is possible). If more than one Kikuchi line intersects the PC then it is referred as a multi–beam diffraction condition. In general, electron channelling contrast images acquired under multi–beam conditions exhibit better signal to noise than those obtained using 2–beam conditions.

The second mode of operation is obtaining electron channelling contrast images. When the SEM is operated at a very high magnification, the angle between the scanned beam and the surface is constant. As a result, changes in crystallographic orientation or changes in lattice constant due to local strain are revealed by changes in contrast in a channelling image constructed by monitoring the intensity of BSE as an electron beam is scanned over the sample. Extremely small changes in orientation (0.01 of a degree) and strain are detectable, revealing for example low angle tilt and rotation boundaries and atomic steps and enabling dislocations to be imaged.

In ECCI, vertical TDs appear as spots with black–white (B–W) contrast; this is seen in Fig. 2.5a, an electron channelling contrast image acquired from a MOVPE grown 1600 nm thick GaN thin film grown by Prof. Peter Parbrook at the University of Sheffield, who is now at the University of Cork, Ireland. All of the electron channelling contrast images shown in this chapter was acquired from this sample, the growth conditions for which are reported elsewhere [91]. Note that the acquisition time required obtaining either an experimental electron channelling contrast image or an ECP is typically less than a minute.

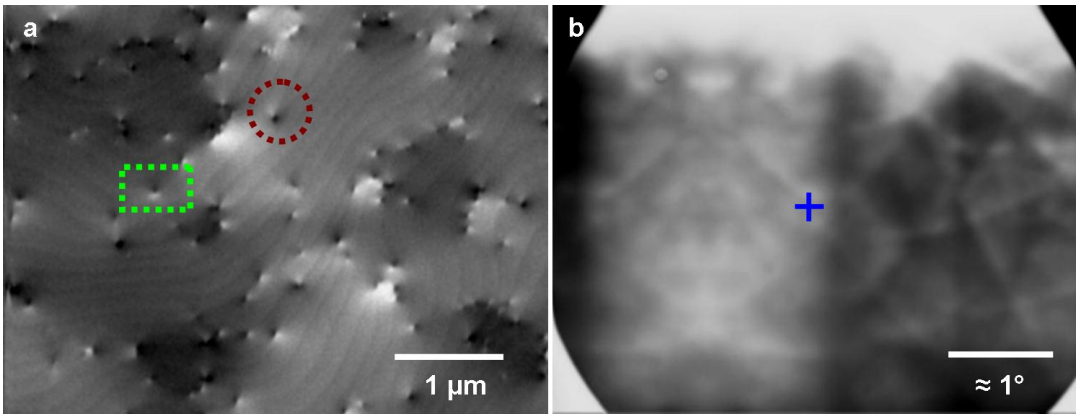

Figure 2.5 (a) Multi–beam electron channelling contrast image showing atomic steps and (b) ECP, both acquired at 30 keV. On the electron channelling contrast image, the dotted circle highlights a dislocation with a screw component and the dotted rectangle highlights an edge dislocation. The cross on the ECP marks the Pattern centre.

For bulk samples the maximum channelling contrast is ≈ 5% or less [70]. In order to observe such a low level of contrast, a minimum beam current (I_{TH}) is necessary. This is given by the below formula where C is the fractional channelling contrast and t is the time to record the image. [92].

$$I_{TH} = 4 \times 10^{-12} / (C^2 t) \text{ amps}$$

The incident current on the specimen can be given by the below formula where d is the spot size, α is the beam convergence angle and B is the electron gun brightness [92].

$$I = 2.5 d^2 \alpha^2 B \text{ amps}$$

Thus the conditions required to resolve individual dislocations in an electron channelling contrast image are quite stringent; a small (nanometres), high brightness

(nanoamps or higher), low divergence or high convergence beam (of order of a few mrad) electron beam is required [63-64, 93]. These conditions are necessary to obtain good–quality channelling contrast and they are met only in a FEG–SEM. All the channelling contrast images in the present work were acquired with an electron beam spot of ≈ 4 nm, a beam current of ≈ 2.5 nA and a beam divergence of ≈ 4 mrad.

Electron channelling contrast images can be acquired in either forescatter geometry (sample is tilted to between 30° and 70° to the impinging electron beam and the forecattered electrons detected by a diode placed in front of the sample) [82, 94] or the backscatter geometry (sample at approximately 90° degrees to the impinging electron beam with the BSE detected by an electron–sensitive diode or diodes placed on the pole pieces of the microscope). Figure 2.6a and 2.6b shows the forescatter and the backscatter geometry respectively. The backscatter geometry has the advantage that large samples, e.g., a full semiconductor wafer, may be imaged and the results obtained may be more easily compared to a TEM diffraction image. The forescatter geometry requires tilt correction of the acquired images but provides a larger channelling signal and therefore channelling images with superior signal to noise. This is shown in Fig. 2.6c where the electron channelling contrast image is acquired under multi–beam condition in the forescatter geometry which shows better signal to noise ratio when compared to backscattered geometry as shown in Fig. 2.6d. The forescatter geometry is the one used in the present work.

It is also necessary to use a detection system that allows discrimination between electrons leaving the sample which carry channelling information and those which have been diffusely scattered by the sample. An amplifier which can offset the diffuse background signal and a preamplifier to amplify the channelling signal is

required. In the present work, the forescatter Si diodes, preamplifier and a signal amplifier were provided by KE Developments Ltd.

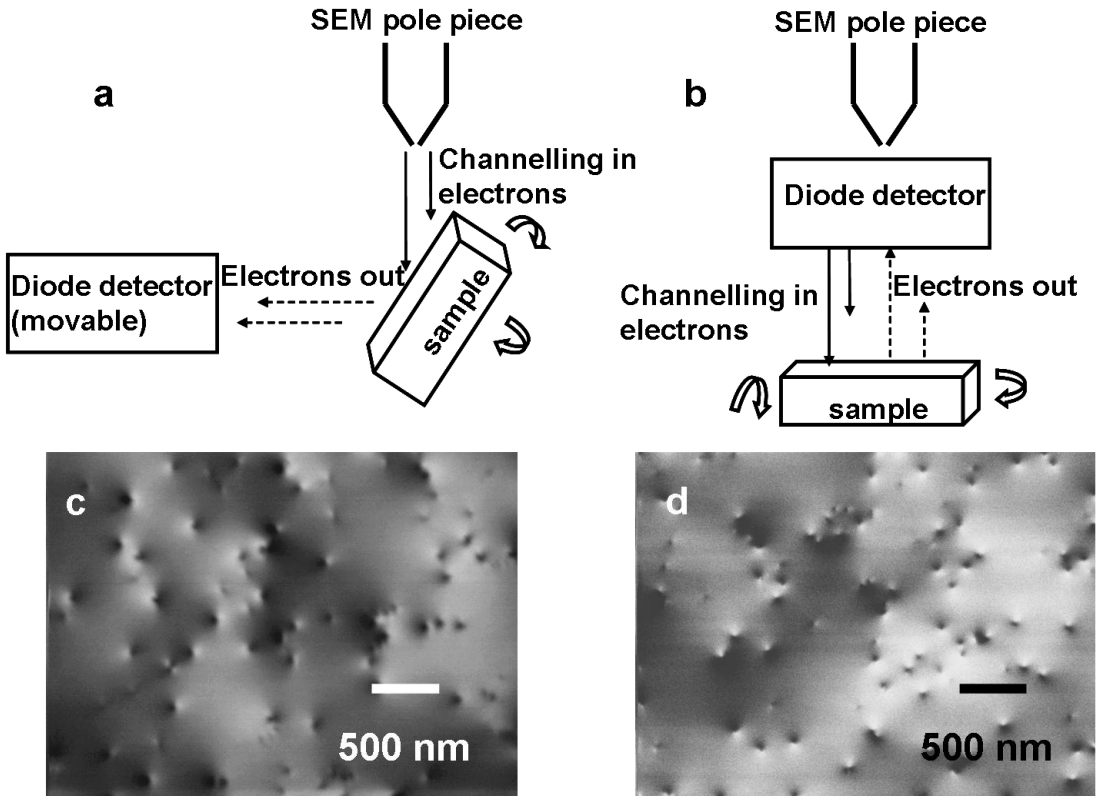

Figure 2.6 (a) experimental geometry used in the present work (forescatter geometry) , (b) backscattered geometry for performing ECCI, (c) &(d) electron channelling contrast images from forescatter and backscatter geometry respectively. Note the images are not from the same area of the sample.

Note the electron channelling contrast image shown in Fig. 2.5a was acquired under multi–beam conditions. In order to index (planes in the ECP to be identified) the acquired ECPs (see Fig. 2.5b), corresponding to the electron channelling contrast

image, both kinematical [95] and dynamical simulations [59] were performed. Kinematical simulations were performed by Dr. Austin Day from Aunt Daisy Scientific Ltd, England. Dynamical simulations were performed by Dr. Aimo Winkelmann from Max–Planck–Institut fur Mikrostrukturphysik, Germany.

In simple terms, kinematic diffraction can be defined as the situation where electrons incident on the crystal surface are elastically scattered only once by the crystal surface. In the case of dynamical diffraction, multiple scattering by the incident beam in the crystal is considered. More information of kinematical and dynamical electron diffraction can be found in the references [95, 59]. Figure 2.7 shows the comparison of experimental ECPs with dynamical and kinematical simulations.

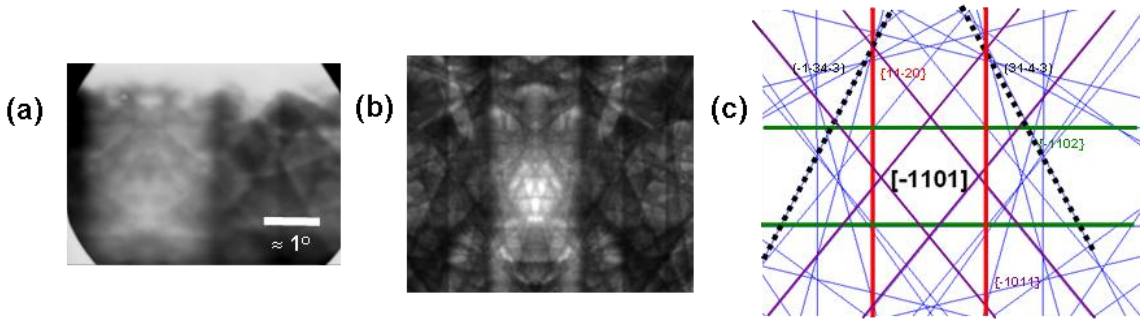

Figure 2.7 (a) Experimental ECP [same as that shown in Fig. 2.3b], (b) Dynamical simulation of ECP and (c) kinematical simulation of ECP from c–GaN (for incident electron beam energy of 30 keV).

2.4 Identifying TDs and atomic steps using ECCI:

In ECCI, it is possible to select a diffraction condition (and the position of the forescatter detector) so that atomic steps in the nitride thin films are revealed. The atomic steps are revealed due to lattice distortion at the steps. Similar step contrast is observed in resonance electron microscopy images [96, 97]. If a diffraction condition is selected so as to give strong contrast for the atomic steps and for screw, edge and mixed dislocations (normally a multi–beam condition), it is possible to differentiate between dislocations with a screw component (those which terminate a step) and pure edge dislocations (those that do not terminate a step) in an manner analogous to that used to identify dislocations in AFM images as explained in *chapter one* [98]. This is illustrated in Fig. 2.5a where the dotted red circle shows TD with a screw component and the green rectangle show an edge type TD. However this method does not allow discrimination between pure screw and mixed dislocations.

It is possible to identify dislocations in electron channelling contrast images using the invisibility criteria used in TEM (*see chapter one*) [35]. However for plan–view diffraction images of c–plane oriented wurtzite materials, it is not possible to satisfy both $\boldsymbol{g}\cdot\boldsymbol{b} = 0$ and $\boldsymbol{g}\cdot\boldsymbol{b} \times \boldsymbol{u} = 0$ for vertical threading edge dislocations ($\boldsymbol{b}$ = 1/3<11-20>), the ideal $\boldsymbol{g}$ to satisfy the invisibility criterion for all edge dislocations is (0002) which is not accessible in the plan–view geometry. For the vertical threading screw dislocations ($\boldsymbol{b}$ = <0001>) surface relaxation dominates and again the invisibility criterion cannot be applied. The surface relaxation contrast mechanism was first described by Tunstall et al [99], and results from "a non–uniform twist of the lattice about the screw dislocation, which decreases with

increasing distance from the centre of the screw". Where a screw dislocation is revealed by surface relaxation, the B–W contrast direction is perpendicular to $\boldsymbol{g}$.

As it was found not to be possible to identify the dislocations in GaN thin films by applying the standard TEM invisibility criteria, another approach had to be developed. To address this issue, a new procedure which exploits the differences observed in the direction of the B–W contrast for screw, edge and mixed dislocations on comparing two images acquired via channelling under 2–beam conditions from two symmetrically equivalent crystal planes whose $\boldsymbol{g}$ are at 120° to each other is employed. In practice it is difficult to achieve exact 2–beam conditions; however it is possible to get sufficiently close to allow quantitative analysis of the resultant electron channelling contrast images.

The diffracting planes were selected to produce similar channelling contrast for the screw, edge and mixed dislocations. The choice of symmetrically equivalent planes for the acquisition of the two images produces a simple and easily predictable change in the direction of the observed B–W contrast.

To my knowledge, there is no reported work on identifying all the different TD types in wurtzite nitride thin films using ECCI. There have been a number of seminal papers published by Picard et al [83-84, 100] in which the authors, following the work of Tunstall et al [99], identified dislocations with a screw component as those which exhibited a B–W contrast direction perpendicular to their selected $\boldsymbol{g}$. They selected their $\boldsymbol{g}$ from EBSPs. They also identified edge dislocations as those whose B–W contrast was independent of $\boldsymbol{g}$. However they were not able to differentiate between screw and mixed dislocations, and thus were not able to identify pure screw dislocations which are the most detrimental to the device

performance in a wide range of nitride semiconductors [101-104]. The ability to unambiguously differentiate all three types of dislocations places the present work in an excellent position to understand the role of screw versus mixed versus edge dislocations in the performance of a wide range of devices.

The technique used to identify dislocation types from the electron channelling contrast images is simple, but the simplicity of the technique relies on choosing appropriate crystal planes for diffraction. Two symmetrically equivalent crystal planes, (3 1 -4 -3) and (-1 -3 4 -3), with $\boldsymbol{g}$ at 120° to each are selected; (see Fig. 2.8). Figure 2.8a and 2.8b shows the electron channelling contrast images taken from the same part of the sample for the two chosen $\boldsymbol{g}$. To identify the dislocation types, changes in the direction of the B–W contrast that occurs when the direction of $\boldsymbol{g}$ is changed was monitored. Figure 2.8c & d show the ECPs which correspond to the electron channelling contrast images of Fig. 2.8a & b respectively. Note that in each case only a single crystal plane has been chosen for diffraction and hence the intensity and contrast of the observed dislocations are determined by these selected crystal planes, i.e., the imaging is performed under 2–beam diffraction conditions.

The circle, rectangle and the octagon shown in Fig. 2.8a & b highlight screw, edge and mixed dislocations respectively taken at the two selected $\boldsymbol{g}$. Note that when the diffraction conditions are changed this also changes contrast in sub–grains, i.e., regions bounded by low angle tilt or rotation boundaries. For example the brighter contrast seen in the top right corner indicated by a black arrow as shown in Fig. 2.8a changes to dark contrast indicated by a white arrow in as shown in Fig. 2.8b. The dark band which appears across the middle of the image shown in Fig 2.8b is a “shadow” cast by a particle on the surface of the sample. This particle was used to

help locate the same part of the sample when the diffraction conditions were changed.

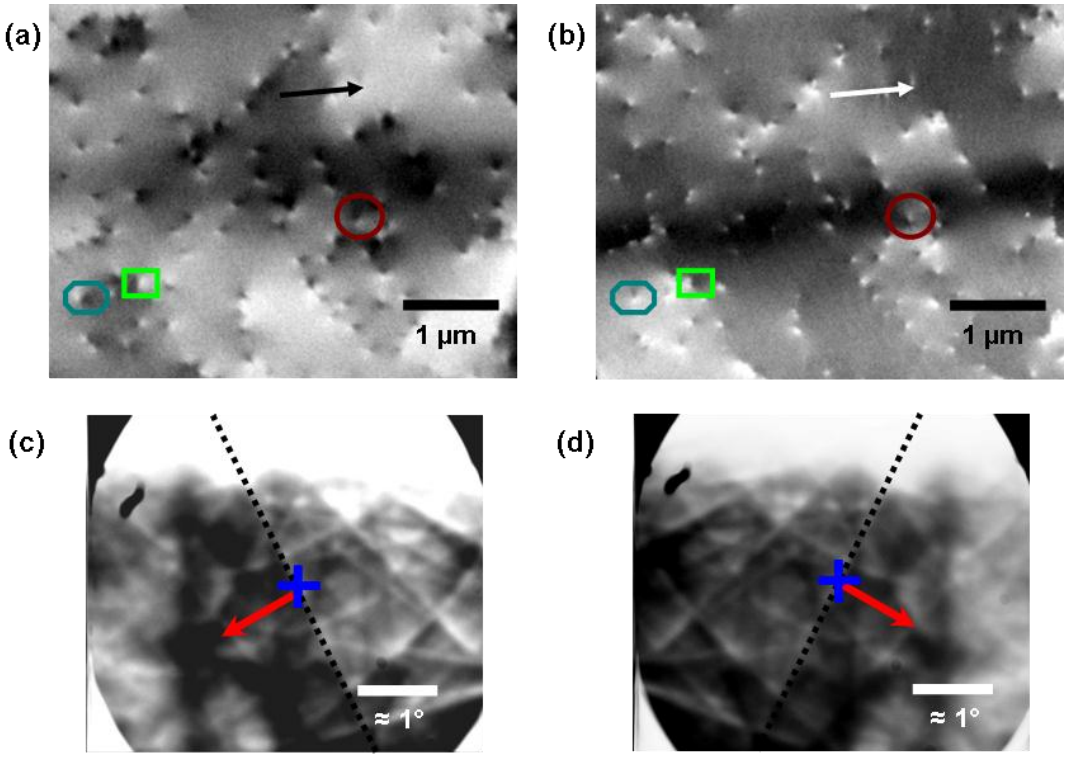

Figure 2.8: 2–beam ECC image and ECP revealing dislocation types: (a) & (b) show electron channelling contrast images from the same part of the sample acquired at *g* of (31–4–3) and (–1–34–3), respectively. The circle indicates a screw dislocation, the rectangle an edge dislocation, and the octagon a mixed dislocation. The black and white arrows highlight the change of contrast for sub grains when g is changed. (c) & (d) show the ECPs which correspond to the ECC images shown in (a) & (b). The cross shows the position of the PC, the black dotted lines highlight the diffracting planes and the red arrow shows the direction of *g*.

Figure 2.9a-h shows high magnification electron channelling contrast images of all the types of TDs. Figure 2.9a-d show images of screw dislocations and show that the direction of their B–W contrast follows ***g*** (as discussed previously) and is always orthogonal to the direction of ***g***. There are two possible directions of the B–W contrast observed for screw dislocations for a given ***g***, corresponding to screw dislocations with a ***b*** of [000±1]. Following the arguments of Edington et al. [48] for the identification of screw dislocations–that if the dark lobe (black contrast direction) lies to the left of ***g*** then it is right handed screw (***b*** [0001]) and if it lies to the left of ***g*** then it is left handed screw (***b*** [000-1]–thus one can assign a ***b*** of [000-1] to the dislocation shown in Fig. 2.9a and a ***b*** of [0001] to the dislocation shown in Fig. 2.9c. This argument is valid assuming the given ***g*** is positive.

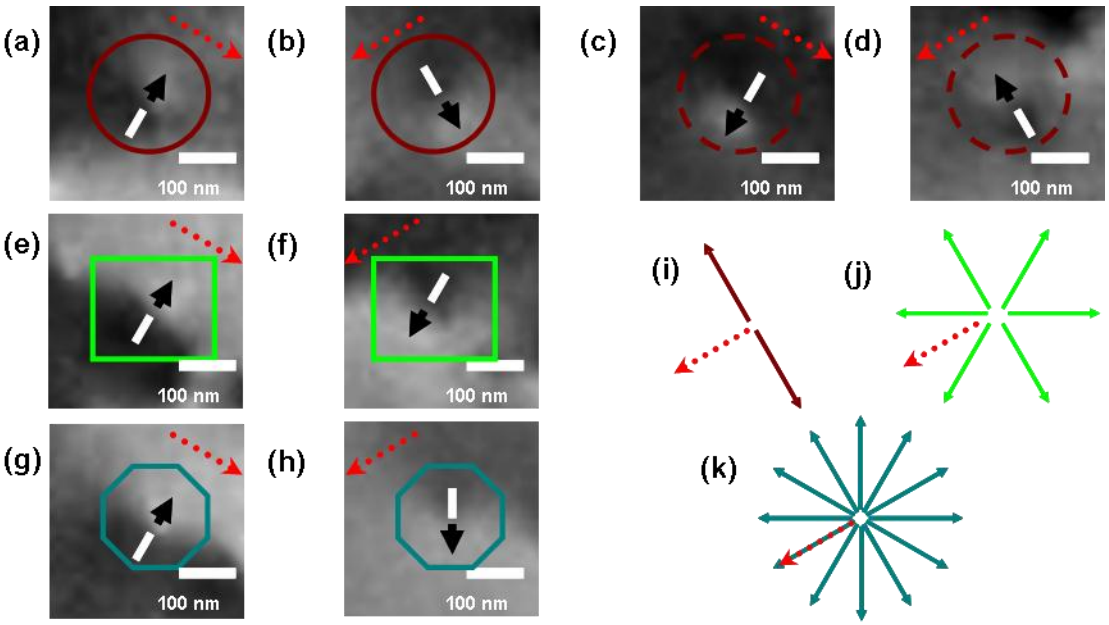

Figure 2.9: Possible B–W contrast directions for TDs: High magnification electron channelling images showing B–W contrast directions for screw (a-d), edge (e-f) and mixed (g-h) dislocations. (i-k) shows the possible directions of the B–W contrast of screw (i), edge (j) and mixed dislocations (k) for a *g* of (3 1 -4 -3). The dotted red arrow denotes the direction of *g*.

The direction of the B–W contrast for an edge dislocation depends on its ***b*** and not on ***g*** [84]. The B–W contrast simply reflects the tensile–compressive strain distribution across the edge dislocation [106]. Figure 2.8e & f show the B–W contrast direction for an edge dislocation for the two selected ***g***; note that on changing ***g*** by 120° the B–W contrast simply reverses. As GaN is a wurtzite semiconductor with six possible ***b*** (1/3<11-20>), six directions of the B–W contrast for the edge dislocations for a given ***g***, where the directions are at 60° to each other is observed. This is shown in Fig. 2.10.

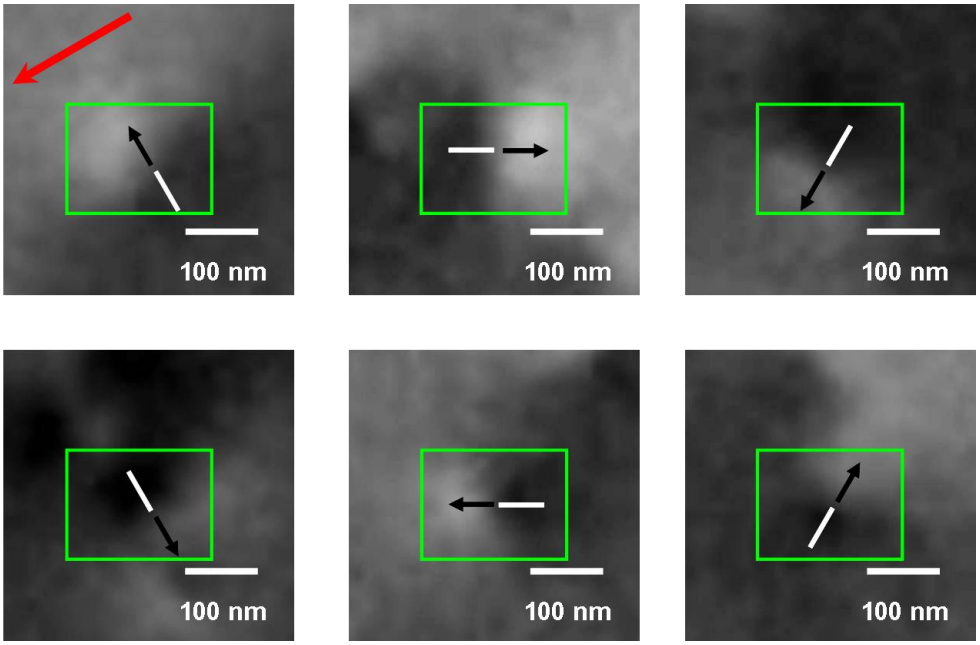

Figure 2.10: Six B–W contrast directions for edge dislocations for the given *g*. The red arrow denotes the direction of *g*.

Finally for mixed dislocations, ***b*** is the vector sum of their edge and screw components, i.e., the ***b*** are 1/3<11-23>. There are 12 possible ***b*** for mixed dislocations. All the twelve directions of the B–W contrast for the mixed dislocations for a given ***g***; with the B–W contrast directions at 30° to each other was observed. This is shown in Fig. 2.11. For the ***g*** used in the present work, six of the B–W contrast directions observed for the mixed dislocations is the same as that observed for either the screw or edge dislocations, i.e., both the screw and edge dislocations B–W contrast directions overlap with that of a mixed dislocation. Figure 2.9i-k show the schematic of possible B–W contrast directions for screw, edge and mixed dislocations respectively for one ***g*** (3 1 -4 -3). However on changing the ***g*** to

(-1 -3 4 -3), the change in B–W contrast direction for a mixed dislocation is different to that of either a screw or edge dislocation. This is illustrated in Fig. 2.9g-h where a mixed dislocation whose B–W direction is parallel to that for the screw and edge dislocations as shown in Fig. 2.9a & c, in the electron channelling contrast image acquired with a ***g*** of (3 1 -4 -3). On changing the ***g*** to (-1 -3 4 -3) the B–W contrast direction for the mixed dislocation is no longer perpendicular to that observed for a screw, and the B–W direction is also not observed to reverse its direction as observed for an edge dislocation. The B–W contrast direction for the mixed dislocation is observed to behave differently to that of a screw or edge dislocation when viewed in two images.

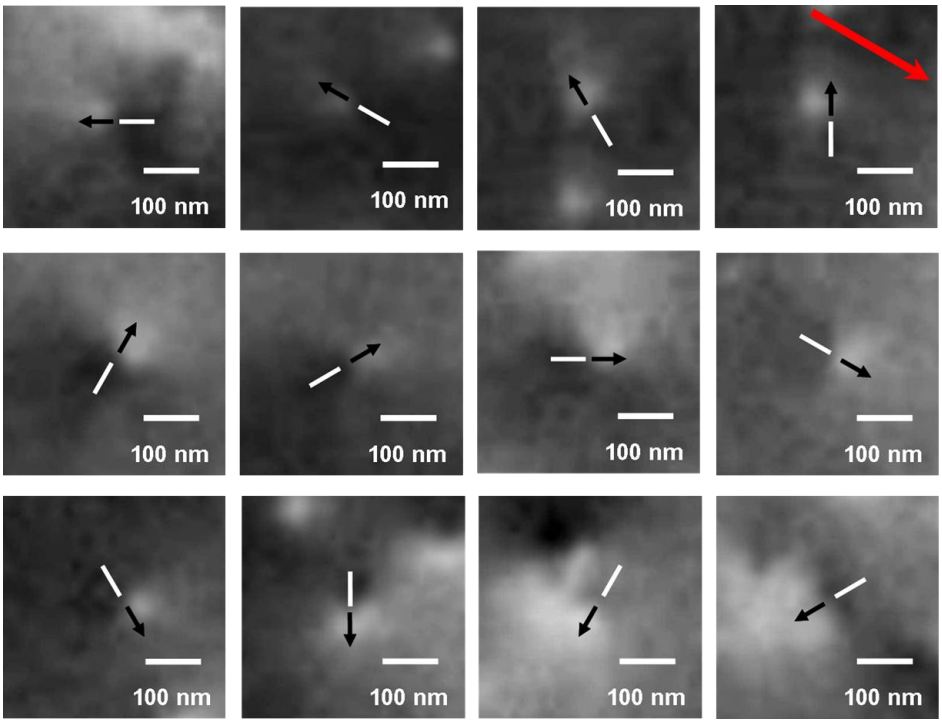

Figure 2.11: Twelve B–W contrast directions for mixed dislocations for the given *g*. The red arrow denotes the direction of *g*.

Once the dislocations have been identified (B–W contrast for nearly 300 dislocations was analysed with an uncertainty of less than 2%) it is possible to determine the relative densities of each type of dislocation. The total dislocation density was found to be $3.6 \pm 0.2 \times 10^{8}$ cm^{-2}. The percentage of pure edge dislocations was ≈ 51% followed by mixed with ≈ 42%. Pure screw dislocations accounted for only ≈ 7% of the total dislocation density. The ratio of the types of individual dislocations depends on the growth conditions and in general screw dislocations are fewer in number when compared to the mixed and edge due to the higher formation energy needed to make them stable. For this sample, the relative densities of screw to edge as determined here are of the same order (7.3:1 as compared to 5.3:1) to those estimated from X–ray diffraction measurements [107]. Similar analysis has been carried out on nitride thin films produced under different growth conditions and the results are discussed in *chapter 6*.

2.5 Summary:

ECCI proves to be an ideal non–destructive technique for the quick analysis of the dislocation densities and also gives qualitative information on tilt and twist boundaries. The approach mentioned in this work is a simple, rapid, non–destructive method which can be used to identify dislocation types in GaN and related alloys, and may also be applied to other materials, with the wurtzite crystal structure.

Chapter 3

Electron channelling contrast imaging for non–polar nitrides

3.1 Introduction:

The results presented in *chapter two* of this thesis were from c–plane GaN. Although c–plane oriented nitride devices have revolutionised the field of blue and green light emitters such as lasers diodes (LDs) and light emitting diodes (LEDs) [108-110], devices made out of c–plane nitrides are not efficient enough. An intrinsic problem with polar nitrides (c–plane orientation) is the presence of large internal electric fields which cause spatial separation of the electron and hole wavefunctions in the quantum well (QW) region (a QWs is a potential well which is used to confine charge carriers) [111]. This is one of the phenomena currently limiting the efficiencies of LDs and LEDs. As mentioned earlier in *chapter one*, to enhance the performance of GaN–based optoelectronic devices, it is necessary to eliminate the polarisation–induced electric field. In order to address this problem, growth of non–polar nitrides (m–plane and a–plane) has been introduced [111, 112].

In this chapter, structural characterisation of m–plane GaN epilayers and m–plane InGaN/GaN multi quantum well samples using ECCI is described. A brief description of presently available characterisation techniques used for determining

SF densities in the nitrides community is presented. Results from ECCI are complemented with XRD, cross–section TEM and AFM studies performed elsewhere.

3.2 Substrates used for growing non–polar nitrides:

Non–polar nitrides are grown on substrates such as γ–$LiAlO_2$ [113], 6H–SiC [114], 4H–SiC [115, 116], r–plane sapphire (1-102) [117], m–plane sapphire (1-100) [118] and (100)–$MgAl_2O_4$ [119]. Amongst these substrates, γ–$LiAlO_2$ has many advantages: It has a tetragonal crystal structure where the (100) plane of γ–$LiAlO_2$ offers similar atomic arrangement as the (1-100) plane of the wurtzite structure (see Fig. 3.1), the ***b*** lattice parameter of γ–$LiAlO_2$ is close to twice the ***a*** lattice constant of GaN with a lattice mismatch of 1.7%, while the ***a*** lattice parameter has a near perfect match to the ***c*** lattice constant of GaN (lattice mismatch 0.3%) [120, 121]. γ–$LiAlO_2$ can also be manufactured by the Czochralski method, where boules of about 20 cm in length and 50 mm in diameter can be pulled from the melt for the production of large area substrates [122].

In addition to low lattice mismatch, γ–$LiAlO_2$ offers the possibility for wet chemical etching to remove the substrate, providing a way to obtain thick and free standing m–plane GaN layers [123]. Despite its huge potential as a substrate for non–polar nitrides, it also exhibits certain drawbacks. For example, inhomogeneous etching of γ–$LiAlO_2$ by a variety of acids makes chemical polishing a complicated task. Moreover, its hydrolytic nature limits its exposure to H_2O [124]. Hence care must be taken with the choice of carrier gas during MOVPE growth on γ–$LiAlO_2$ due to the resulting hydrogen sensitivity [125].

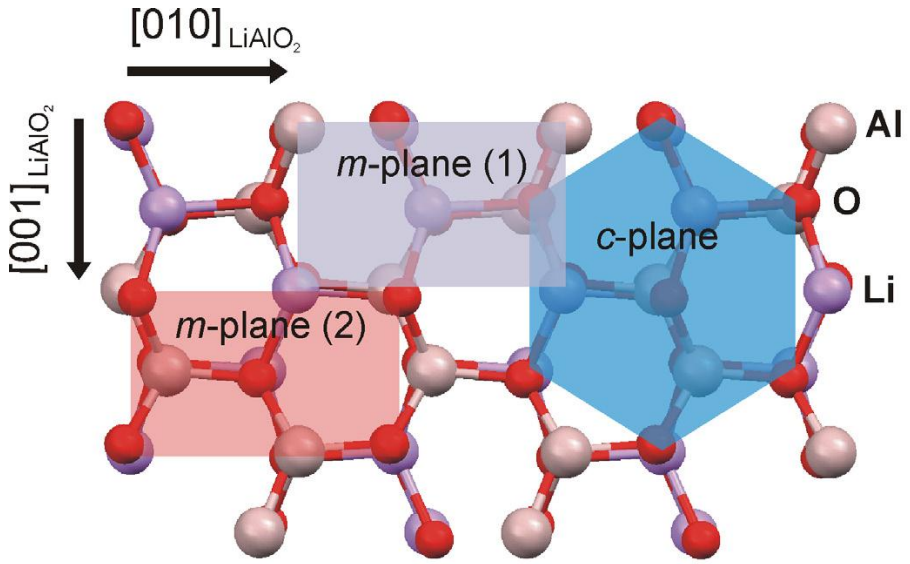

Figure 3.1 Possible GaN growth alignments on γ–$LiAlO_2$. Note that the diagram also shows it is possible for c–plane nitrides growth on γ–$LiAlO_2$. (*Courtesy of Dr. Christof Mauder*).

3.3 Characterisation techniques for studying extended defects in non–polar nitrides:

Irrespective of the substrates or the growth plane employed, extended defects such as TDs, SFs and PDs are always present even in best as–grown layers [60, 126-128]. In nonpolar materials, SFs and the associated PDs are of particular concern because of the higher densities of these defects in such materials. The capability to analyse TDs, PDs and SFs and determine their densities non–destructively, rapidly and without any sample preparation will remove a significant bottleneck to the development of high quality non–polar materials.

Recent advancements have made XRD a powerful tool for characterising nitride semiconductors, but there are several limitations in using XRD to characterise non–polar nitrides [129]. Modified Williamson–Hall analysis is a widely used method to estimate SF densities in non–polar GaN thin films [130]. However the accuracy of this technique is limited to line densities above 10^4 cm^{-1}. Moreover, the applicability of this method is questionable as other superimposing effects, such as surface morphology and wafer bowing, may produce unphysical results [131].

As discussed in *chapter two*, TEM is the most widely used technique for characterising individual dislocations and also SFs [34, 132-134]. High resolution TEM images are used to reveal the stacking sequence of the SFs and thus identify their types [135]. However, difficulties in sample preparation, and the localised nature of the information acquired from TEM make other microscopic imaging techniques worthwhile to explore.

3.4 MOVPE grown heteroepitaxial layers of m–plane GaN and m–plane InGaN/GaN MQWs:

For the present work, m–plane GaN epilayers and m–plane InGaN/GaN MQW structures where a thin layer of InGaN QW sandwiched between GaN barriers with different InN compositions were provided by Dr. Christof Mauder from Aachen University, Germany. m–plane GaN buffer layers of 0.9 µm were grown on top of (100) γ–$LiAlO_2$ substrates using MOVPE. The MQW structures consist of 5 pairs of 4 nm thick InGaN wells and 16 nm thick GaN barriers and were deposited on top of the m–plane GaN buffer at different temperatures to vary the InN content in the

QWs. A detailed description of the growth procedure and optical properties of the samples are given in the references [136, 137]. In total six samples were characterised using ECCI, one m–plane GaN epilayer (buffer layer for the MQW growth) and five m–plane InGaN MQW samples with 4%, 5%, 16%, 20% and 30 % of InN grown on top of an m–plane GaN buffer layer. The InN compositions were estimated from XRD measurements [136]. Figure 3.2 shows schematics of the samples.

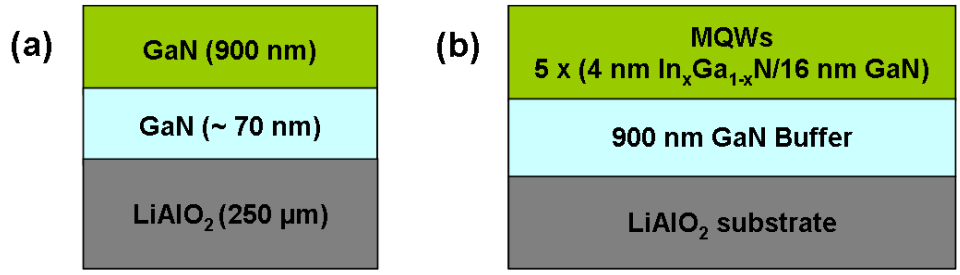

Figure 3.2 (a) Schematic diagram of an m–plane GaN buffer layer for growing MQWs (b) m–plane InGaN MQWs with four alternating layers of InGaN/GaN with varying InN content.

3.5 ECCI for m–GaN and m-InGaN MQWs:

Figure 3.3a shows the schematic of I_1 type stacking fault which was discussed earlier in *chapter one*. The majority of the observed SFs in nitrides are of I_1 type. Figure 3.3b shows an electron channelling contrast image for the m–plane GaN buffer layer revealing a striated pattern along [0001] which is related to the anisotropic growth mode of m–plane GaN on $LiAlO_2$ [119, 138]. BSFs in ECCI appear as lines with a PD terminating each end, and TDs appear as spots with B–W contrast (as described in *chapter two*).

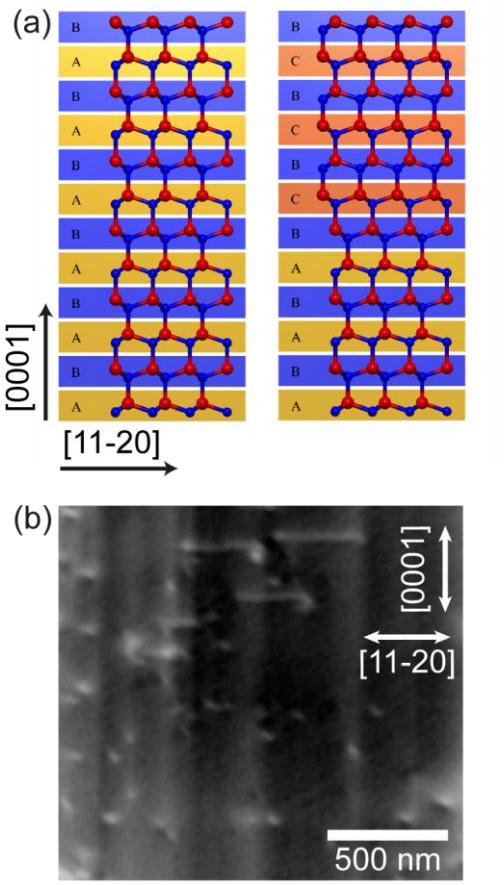

Figure 3.3: (a) Schematic diagram of a perfect wurtzite lattice and the faulted region (I_1 BSF) introduced by replacing the bilayer A (yellow color) to C (red color). (b) ECCI of m–plane GaN layer exhibiting BSFs and TDs. The stripe direction was determined by XRD measurements.

A high magnification image of BSFs running along [11-20] (which is the basal plane direction for m–plane GaN), from an m–plane $In_{0.04}Ga_{0.96}N$/GaN MQW, is shown in Fig. 3.4a. The contrast mechanism for BSFs is similar to TDs as both of them strain the crystal lattice. BSFs can either appear as a line with B–W contrast as shown in Fig. 3.3b or just as a black or white line as marked with dashed and dotted white circles in Fig. 3.4a. Dislocations and SFs are crystallographic features and generally

do not appear in SE images which are sensitive primarily to topography. Figure 3.4b shows the corresponding SE image taken from the same region as the channelling contrast image shown in Fig. 3.4a. While the stripes along [0001] (and along [11-20], discussed later) are clearly discernible in the SE image due to their topography, on comparing the two images it becomes clear that BSFs only show observable contrast in the electron channelling contrast images. The contrast for TDs and BSFs is due to channelling; if the sample is tilted or rotated (moved away) from the channelling conditions the TDs and BSFs disappear, confirming that these features are indeed imaged by channelled electrons. Note that it is also possible to observe channelling contrast in SE images, but in general, due to detection conditions, the contrast is low and difficult to discern.

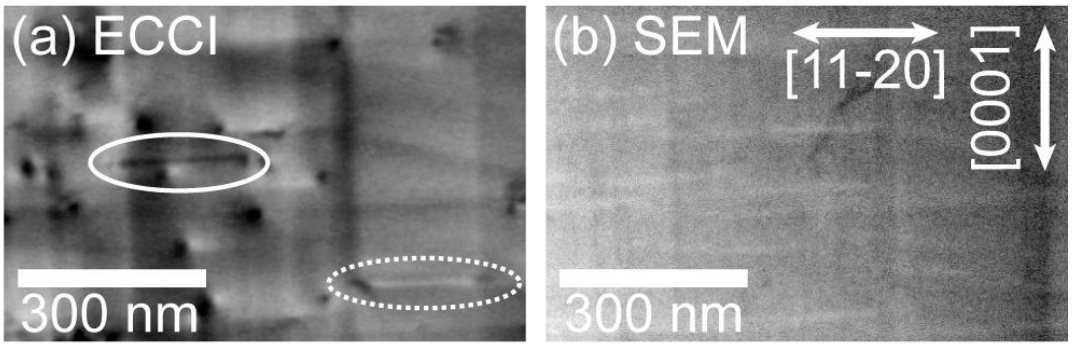

Figure 3.4: (a) High magnification ECC image of $In_{0.04}Ga_{0.96}N$/GaN MQW, (b) SEM image of the same area. The dashed and dotted ellipses shows the BSF regions.

3.5.1 HR–TEM for m–plane $In_{0.10}Ga_{0.96}N$/GaN MQWs:

In order to confirm the type of BSFs which are present in the analysed samples, cross–sectional TEM was performed on an m–plane $In_{0.10}Ga_{0.90}N$/GaN MQW at the Paul–Drude institute in Berlin by Dr. Wang using a JEOL 3010 transmission electron microscope. Samples were prepared by standard mechanical polishing and Ar ion beam thinning at 3 keV. Figure 3.5 shows a high resolution cross–sectional TEM lattice image which shows the stacking sequence of crystal planes. The circles highlight the stacking sequence for an I_1 SF. No other types of BSF were observed in this structure for the area analysed using TEM. Moreover, the lateral extension of BSFs revealed by ECCI is always in the same range (of the order of 300 nm in length), so it can be assumed that all BSFs observed by ECCI are of the same type, namely I_1.

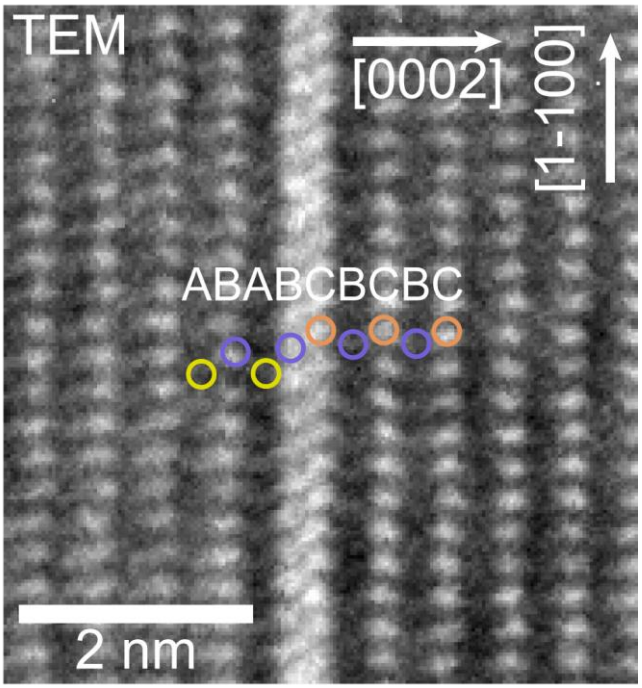

Figure 3.5: High resolution cross-sectional TEM image showing the stacking mismatch. The atomic layers are indicated by similar colors as those used in Fig. 3.3a (*courtesy of Dr. Wang*).

3.5.2 Estimation of SF and TD densities:

Care has to be taken when counting TDs and SFs to build up statistically significant values for the TD and BSF densities. Series of electron channelling contrast images from random locations on the samples were acquired for this purpose. SF densities are typically represented as line densities (cm^{-1}) which are calculated by dividing the SF area by the probed volume of the sample. In TEM, BSF densities can be measured from plan view and/or cross–sectional images, whereas in ECCI the BSF densities are estimated purely from plan view images. As ECCI can yield information from a larger field of view, up to of order 500 μm^2, statistically

significant numbers for defect densities can be estimated. In the present work, TD, BSF and PD densities were estimated from several images each with an area of $\approx 5\ \mu m^2$, similar to the electron channelling contrast image shown in Fig. 3.3b. The TD density for the m–plane GaN buffer layer was found to be $2.1 \pm 0.3 \times 10^9\ cm^{-2}$. Assuming the BSFs propagate through the entire sample, their line density was estimated to be $\approx 0.6 \times 10^4\ cm^{-1}$.

The BSF densities obtained using ECCI was compared to that estimated by XRD. XRD measurements were performed by Dr. Christof Mauder from Aachen University, using a PANalytical X'Pert MRD Pro in open detector geometry. An estimation of BSF density was obtained by applying the XRD Williamson–Hall method employing the (1-100) and (2-200) ω–scan peak [130]. This provides an estimated BSF density of $\approx 1 \times 10^4\ cm^{-1}$ which is of similar order of magnitude to the ECCI value.

In order to increase the reliability of the analysis without any assumptions, BSF number densities (area densities) were also estimated by simply counting the total number of BSFs appearing in the entire field of view in the ECCI images. For the m–plane GaN buffer layer, the BSF number density was found to be $9 \pm 2.5 \times 10^7\ cm^{-2}$ with a corresponding PD density of $1.8 \pm 0.5 \times 10^8\ cm^{-2}$; this is an order of magnitude lower than the TD density.

The TD density and the BSF number densities for an m–plane $In_{0.04}Ga_{0.96}N$/GaN MQW structure (the high magnification image shown in Fig. 3.4a is from this sample) were found to be $2.5 \pm 0.3 \times 10^9\ cm^{-2}$ and $9.5 \pm 4 \times 10^7\ cm^{-2}$ respectively and thus in a very similar range to that of the m–plane GaN buffer layer.

The BSF line density was estimated to be ≈ 0.9×10^4 cm^{-1}. For this structure it was not possible to obtain an estimate of the BSF line density by XRD.

3.5.3 Striated features along [11-20]:

For the MQW structures, in addition to the striated features along [0001] which stem from the GaN buffer layer, another type of stripe (surface steps) are observed along [11-20] as shown in Fig. 3.4 (best observed in Fig. 3.6a). These features are only observed for the MQW samples, which indicate that they are either related to the lower growth temperature (required for the growth of InGaN) or the presence of In during growth. An induced change in the anisotropic barrier height for adatom diffusion on the surface may be considered as an explanation for the observation of these features, but the exact origin is still under investigation. Although the direction of these features is identical to the BSF extension, the local positions of BSFs were found to be independent of the surface striations along [11-20] as revealed by the electron channeling contrast image shown in Fig. 3.4a. It is therefore very unlikely that these striated features are related to the BSFs.

The density of the striated features along [11-20] and also the overall surface roughness increases with InN content. This makes it difficult to identify BSFs for samples with MQWs containing more than 5% InN. Although the surface roughness is of the order of 2 nm for a $1 \times 1\mu m^2$ area estimated from AFM images shown in Fig. 3.7, it was still possible to estimate the TD densities by ECCI. The AFM images were acquired by Dr. Christof Mauder from Aachen University.

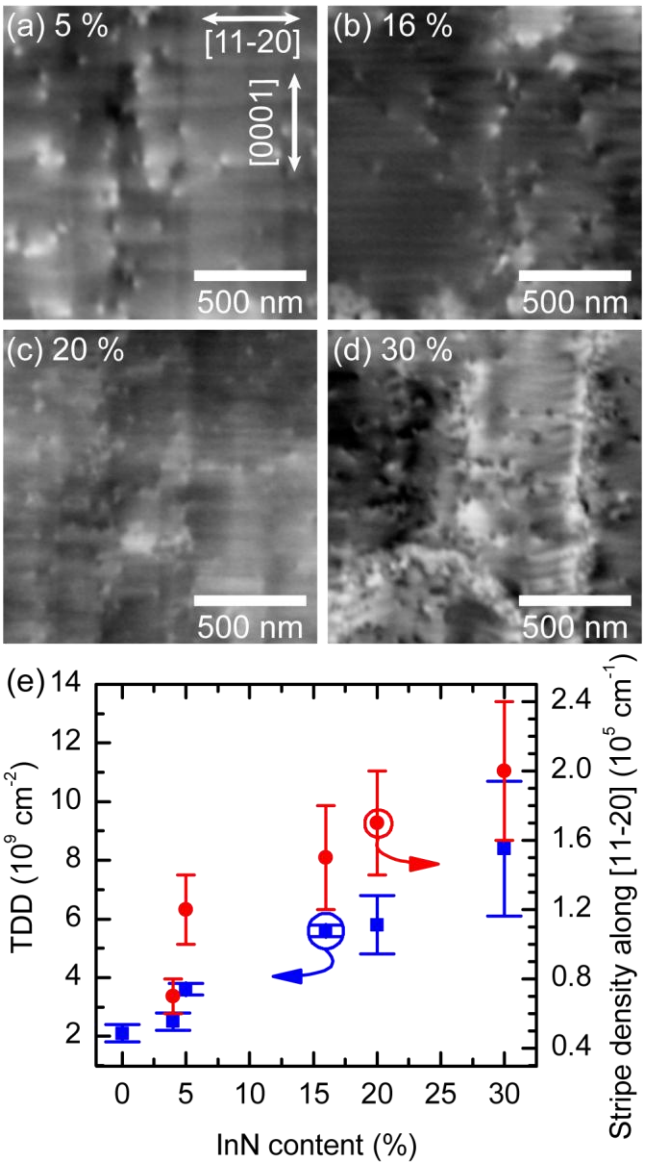

Figure 3.6: (a–d) ECC images showing TDs and striated features along [0001] and [11-20]. The stripes direction in (a) and (b) are the same as shown in (c) and (d). (e) Graph showing the increase of TDs and stripe density with error bars as InN % is increased. The values are calculated from electron channelling contrast images.

Figures 3.6 a-d show electron channelling contrast images for InGaN/GaN MQWs with 5%, 16%, 20%, and 30% InN content, respectively. In Fig. 3.6e, the average TD density values are plotted against the InN fraction, with the 0% InN fraction representing the GaN buffer layer. As the InN fraction increases, higher numbers of TDs are observed which are of the order of $\approx 5–7 \times 10^{9}$ cm^{-2} for MQWs with 20–30 % of InN. The obvious increase in TD density for the MQW samples shows that additional defects are generated during the MQW growth. A reduced growth temperature and larger lattice strain may be responsible for the decrease in crystal quality. Since it was not possible to identify BSFs in MQW samples with InN contents above about 5%, the possibility that these defects are caused by an increase in BSF density, which would also result in more PDs also cannot be ruled out. Feng et al. recently performed cross–sectional TEM analysis of m–plane $In_{0.26}Ga_{0.74}N$/GaN MQWs and found that BSFs are formed within the MQWs [134].

The stripe densities along [11-20] were also determined from both SEM and AFM images, which are of the order of $1 – 2 \times 10^{5}$ cm^{-1}. This increase in the stripe densities along [11-20] is probably related to changes in the growth conditions required for higher InN incorporation in the MQWs [137].

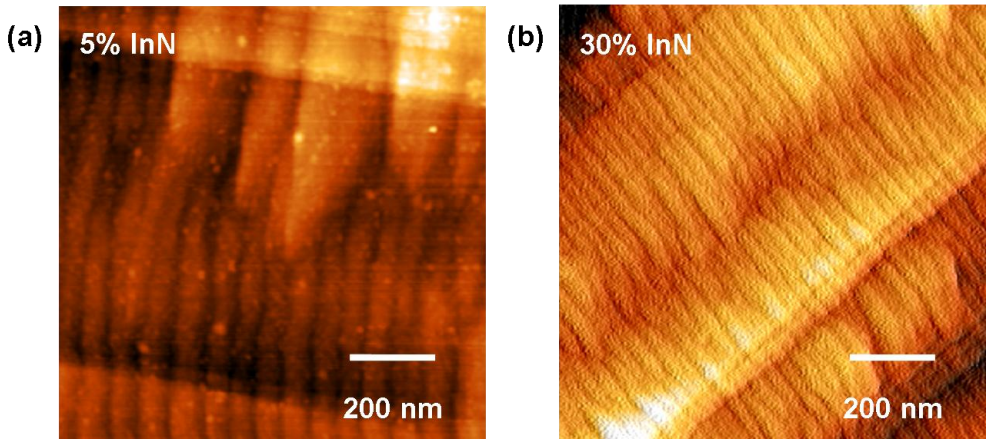

Figure 3.7 (a) AFM image showing the striated features for InGaN MQW with 5%InN and (b) with 30%InN. The increase in the density of the striated features can be seen clearly (*Courtesy of Dr. Christof Mauder*).

3.6 Summary:

In summary it was demonstrated that ECCI is an excellent technique for rapid and non–destructive quantification of TD and SF densities in non–polar nitrides when compared to the presently available techniques. To the best of my knowledge, this is the first report on determining statistically reliable TD and BSF densities for non–polar nitrides. TEM measurements show that, the observed BSFs are predominantly of I_1–type. The production of reasonable quality MOVPE InGaN/GaN MQW structures (InN content ≈ 20%) grown on γ–$LiAlO_2$ with TD densities in the order of ≈ 5×10^9 cm^{-2} is shown to be possible. ECCI technique will be of great benefit for the development of high quality semiconductor materials and is particularly useful for the detection and quantification—and thereby eventual reduction—of stacking faults in nonpolar materials.

Chapter 4

Characterisation of InAlN/GaN heterostructures

4.1 Introduction:

InAlN possesses the widest bandgap range in the nitride system and thus becomes a potential material for applications in LEDs, LDs and solar cells operating from the UV to the near infrared [139, 140]. In addition to this, $InAl_{1-x}N$/GaN heterostructures can either be tensile or compressively strained depending on the InN composition, which cannot be implemented in $Al_xGa_{1-x}N$/GaN heterostructures. The possibility of polarisation engineering makes InAlN more attractive for high frequency transistor applications [141]. InAlN can also be latticed matched with GaN when the InN composition is ≈ 18% which makes it a strong candidate for high electron mobility transistors (HEMTs) [142], and distributed Bragg reflectors (DBRs) [140]. Among its applications, lattice matched InAlN HEMTs and DBRs seem to be the most attractive and viable device applications.

Although the first ever growth of polycrystalline InAlN was in 1981 [143], the production of this technologically important material is still challenging. It is difficult to make high quality InAlN due to the different optimum growth temperatures for InN and AlN and because of difference in the InN and AlN covalent bonds, leading to phase separation and fluctuation in the InN composition. Poor growth conditions also lead to highly defective and cracked layers. However,

improvements in MBE [144, 145] and MOVPE [146-148] growth techniques have made it possible to improve the crystalline quality of the InAlN thin films. Generally MOVPE produces higher crystallinity InAlN thin films when compared to MBE [140].

In this chapter structural characterisation of InAlN/GaN and InAlN/AlN/GaN heterostructures for HEMT applications will be discussed. The effects of including an AlN interlayer between the InAlN top layer and the GaN and the role of the buffer layers and substrates on the HEMTs properties are also discussed. Finally, the effect of substrates on TDs densities on InAlN/GaN DBRs will also be discussed. The samples discussed in this chapter are from the EU–ITN project known as RAINBOW whose aim was to grow and optimise high InN containing semiconductors.

4.1.1 HEMTs and DBRs:

A junction formed between two different materials is described as a heterojunction and the structure used to make such a junction is known as a heterostructure. HEMTs are a special kind of transistor which uses electric fields to enhance the mobility of electrons at a heterojunction between materials of different band gaps (e.g.: InAlN/GaN, AlN/GaN). Due to the large polarisation difference at the heterostructure interface and also due to the piezoelectric fields, a high density sheet of electrons is formed at the interface, which is commonly referred to as a two dimensional electron gas (2–DEG) [149]. HEMTs have applications in electronic devices such as mobile phones and computer processers.

DBRs are structures with multiple layers of alternating materials with varying refractive index [150]. Each interface between the two materials contributes a Fresnel reflection and the constructive interference from the Fresnel reflection gives a strong light output. DBRs are used to produce high quality laser diodes which could have future applications in the area of optical fiber communications, optical metrology and high–resolution spectroscopy [150].

4.2 InAlN/GaN, InAlN/AlN/GaN heterostructures for HEMT applications:

HEMT samples were grown by Dr. Hannes Behmenburg from Aixtron in Aachen. The samples were grown by the MOVPE technique using an AIXTRON CCS reactor using TMGa, TMAl, and TMIn and NH_3 as precursors for Ga, Al, In, and N respectively. More details on growth conditions are given in the refernces [151, 152]. Figure 4.1 shows the schematic of a basic InAlN/GaN HEMT structure. The interface between the InAlN and GaN region is highlighted in Fig. 4.1 where a 2–DEG is formed.

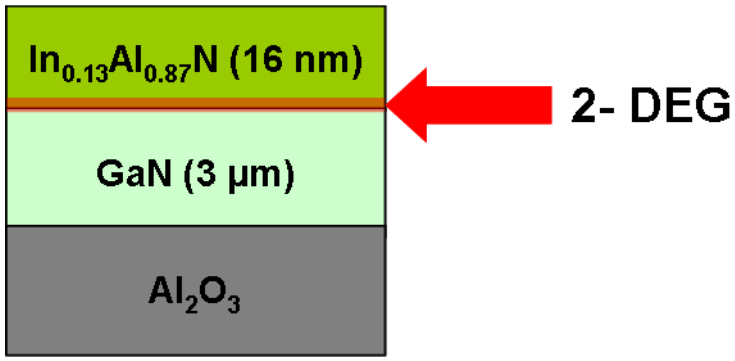

Figure 4.1 Schematic of a simple HEMT structure showing the 2–DEG region. The nominal InN composition is of ≈ 13 %.

4.2.1 Effect of AlN interlayer:

When a thin intermediate AlN layer is inserted between the GaN and the InAlN layer, alloy scattering is reduced due to the formation of a smooth interface between InAlN and GaN [153], and this makes the 2–DEG density increase. It was theoretically predicted that with an intermediate AlN layer thickness of ≈ 7 nm, the 2–DEG density reaches close to the polarisation limit [154], but at such thicknesses the InAlN layer develops cracks which leads to poor quality device structures. Figure 4.2 shows a schematic of the samples used in the present work to study the effect of AlN interlayer on the structural properties of the HEMT structures. ECCI results from these samples were compared to those obtained from the sample with no AlN interlayer shown in Fig. 4.1.

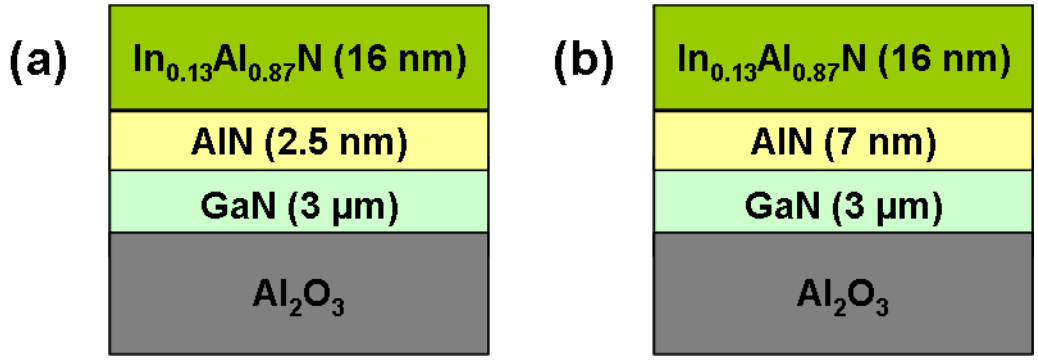

Figure 4.2 Schematic of sample structures with different AlN interlayer thicknesses. The sample thickness and the nominal InN composition is maintained similar to the sample without an AlN interlayer (see Fig. 4.1).

In addition to ECCI, a number of other complimentary techniques were used to assess the quality of the samples, namely AFM and TEM. AFM was performed to check the surface morphology and to estimate the roughness of the grown heterostructures. AFM measurements were performed by Dr. Arantxa Vilalta–Clemente from CIMAP, using a Digital Instruments Nanoscope III operating under tapping mode. Root mean square roughness of the sample surfaces was determined for areas of 5 µm × 5 µm. Figure 4.3 shows AFM images of samples with no AlN interlayer (see Fig 4.1), 2.5 nm and 7 nm AlN interlayer (see Fig. 4.2) respectively. Samples with no AlN and a 2.5 nm AlN interlayer show a honey comb or tiny grain like morphology which is typical for InAlN thin films [139]. High magnification images are shown in the inset of Fig. 4.3a and Fig. 4.3b, which clearly reveal the grain like morphology. However, these layers are smooth enough to perform ECCI, but the sample with the 7 nm AlN interlayer does show surface cracks. Electron

channelling contrast image confirm the presence of surface cracks (See Fig. 4.6c). In addition to surface cracks, V–pits (V–defects) are also observed.

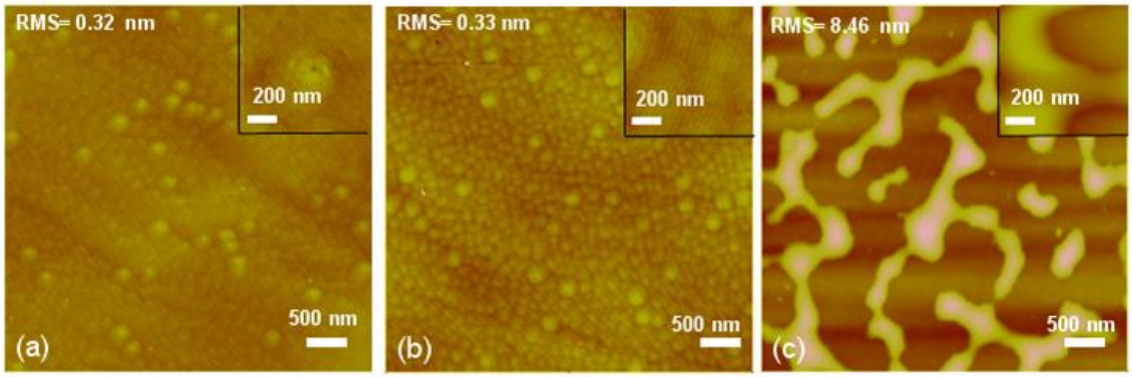

Figure 4.3 AFM images revealing the surface morphology and root mean square roughness of the samples with no AlN (a), with 2.5 nm (b) and 7 nm AlN (c) interlayer respectively. The inset shows high magnification images (*courtesy of Arantxa Vilalta–Clemente*).

V–defects are commonly observed topographic defects in In containing nitrides [155]. In cross–section TEM images, these defects look like V–shape opening, and hence the name. The origin of V–defects is not yet completely understood, they appear to be connected with TDs, but in some cases they can also form without TDs. V–defects typically comprise an open inverted hexagonal pyramid shape normal to (0001) and {10-11} facets. Figure 4.4 shows a schematic of a V–defect, where a TD opens up at the apex of the inverted pyramid structure. Clustering of such V–defects are seen on the surface of the InAlN layer with 7 nm AlN interlayer as shown in the SE image (see Fig. 4.5).

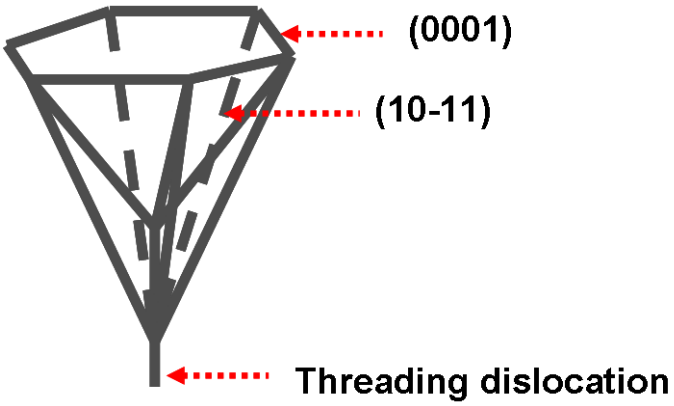

Figure 4.4 Schematic showing a V–defect where a TD terminates at the apex of the open hexagonal inverted pyramid.

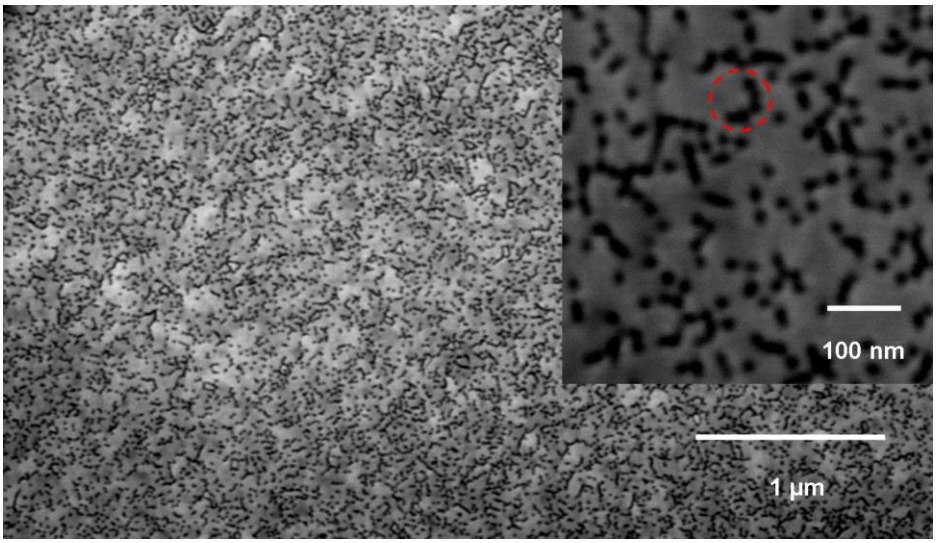

Figure 4.5 Secondary electron images acquired at 5 keV of a 7 nm AlN interlayer sample revealing clustering of V–defects highlighted by red circle in the inset.

Although these V–defects seem to originate from TDs, which are formed during the growth, not all types of TD (screw, edge and mixed) have equal

probability in opening into a V–defect. Mixed TDs have a higher probability of forming a V–defect when compared to pure screw or edge dislocations [155]. It is also found that these V–defects were detrimental to device performances, similar to TDs [156]. These kinds of defects can also amalgamate together and appear as trenches, as shown in the inset of Fig. 4.5. More information on V–defects can be found elsewhere [155-157].

In order to compare the distribution of TDs on varying the AlN interlayer thickness, ECCI was performed. Figure 4.6 shows electron channelling contrast images for samples without an AlN interlayer, a 2.5 nm and a 7 nm AlN interlayer. TDs are counted from electron channelling contrast images with an imaging area of ≈ 25 μm^2. Several images were acquired to obtain a reliable TDs density. For the sample with no AlN interlayer, the TD density was estimated to be $2.5 \pm 0.6 \times 10^8$ cm^{-2} and for the 2.5 nm interlayer AlN sample, the TD density was estimated to be $3 \pm 0.5 \times 10^8$ cm^{-2}. There is no appreciable change in the TD density between these two samples.

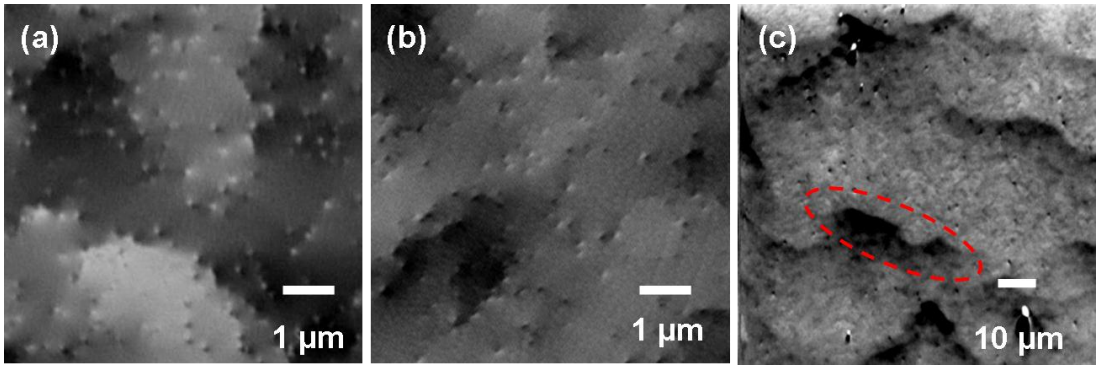

Figure 4.6 electron channelling contrast images for the samples with no AlN (a), with 2.5 nm (b) and 7 nm AlN (c) interlayer respectively.

However, on increasing the AlN interlayer to 7 nm, the V–defect density estimated from SE images (see inset of Fig. 5.3) was found to be $3 \pm 0.8 \times 10^{10}$ cm^{-2}. The increase in the V–defect density by two orders of magnitude is attributed to the change in the growth mode from 2–D to 3–D, causing micro cracks [13]. Figure 4.6c shows ECCI from 7 nm AlN interlayer sample, where a micro crack is highlighted by a red ellipse and the layer morphology clearly reveals the 3–D growth mode.

TD densities from ECCI were also compared with plan view TEM images acquired by Dr. Arantxa Vilalta–Clemente from CIMAP, using a JEOL 2010 transmission electron microscope operated at 200 keV. Plan view and cross–section samples were prepared by polishing techniques followed by Ar ion milling for electron transparency at liquid nitrogen temperature. Figure 4.7 shows plan view TEM images for samples without AlN, and with a 2.5 nm and 7 nm AlN interlayer respectively. For the sample with no AlN interlayer, the TD density was estimated to be $\approx 3 \times 10^{8}$ cm^{-2} and for the 2.5 nm AlN interlayer sample, the TD density was estimated to be $\approx 1.9 \times 10^{8}$ cm^{-2}. TD densities from plan view TEM images were fewer in number when compared with electron channelling contrast images. The difference in TD densities between ECCI and TEM can be attributed to the variation in the probing area combined with the localised information obtained from TEM images. However, the TDs densities are in the same order of magnitude (in the range of $\approx 10^{8}$ cm^{-2}).

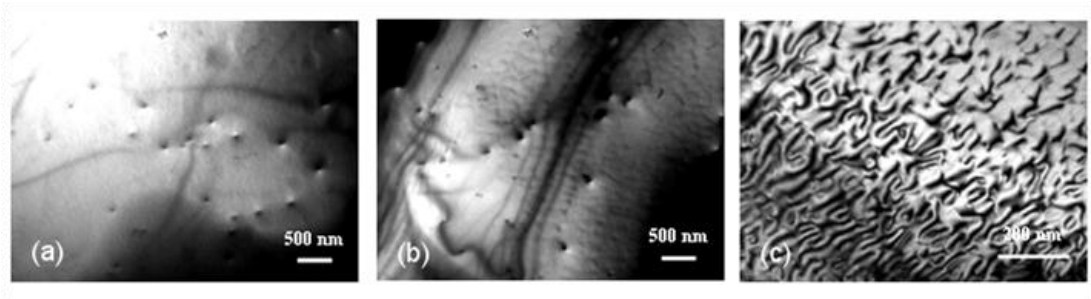

Figure 4.7 plan view TEM images for the samples with 0 nm, 2.5 nm and 7.5 nm AlN interlayer respectively. (*Courtesy of Dr. Arantxa Vilalta–Clemente)*

Although the samples were smooth enough to perform ECCI, they were not smooth enough to record ECPs. For samples where ECPs are not available, cross section TEM becomes necessary to indentify individual dislocation types. The relative number of different types of TDs was investigated by recording dark field weak beam images under (0002) and (10-10) reflections (images not shown here). By using the invisibility criteria as explained in *chapter two* for identifying individual TD types, ratios of screw, edge and mixed dislocations were estimated. For the sample with no AlN interlayer, ≈ 9 % of screw, ≈ 30 % edge and ≈ 61% of mixed dislocations were found. The sample with the 2.5 nm AlN interlayer had no screw dislocations in the analysed area, whereas ≈ 32 % of edge and ≈ 68% of mixed dislocations were found. In the case of the 7.5 nm AlN interlayer sample, there was ≈ 8 % of screw, ≈ 34 % edge and ≈ 58% of mixed dislocations. As mentioned earlier in *chapter two*, the formation energy of pure screw dislocation is higher when compared to pure edge and mixed dislocations and hence generally there are fewer screw dislocations than edge or mixed. The ratio of the dislocation types gives some information on the quality of the grown samples. Generally samples with fewer

screw dislocations are considered best for device applications as pure screw dislocation are claimed to be most detrimental to device performance [103,104,157]. Thus the sample with 2.5 nm AlN interlayer was identified as the most suitable structure for HEMT applications when compared to the other two samples. Electrical conductivity and mobility measurements performed elsewhere also show a small increase in electron mobility for this sample [152]. Note that this can also be due to the optimised growth interface of the AlN interlayer. Table 4.1 summaries the results from various characterisation techniques to compare the effect of AlN interlayer on structural and electrical properties of InAlN based HEMTs.

Table 4.1 summary of the results from various characterisation techniques to compare the effect of AlN interlayer on structural and electrical properties of InAlN based HEMTs (*courtesy of Dr. Arantxa Vilalta–Clemente and Saurabh Pandey*)

AlN interlayer thickness	**AFM** – RMS for 5 x5μm^2 (nm)	**ECCI** TDs x 10^8 (cm^{-2})	**TEM** -TDs x 10^8 (cm^{-2})				**Hall mobility** x 10^3 (cm^{2}v^{-1}s^{-1})
			Plan view	cross section (TDs %)			
				edge	screw	mixed	
Nil	0.32	2.5 ± 0.6	1.3	30	9	61	0.8
2.5	0.33	3 ± 0.5	1.9	32	0	68	1.2
7	8.46	3 ± 0.8 x 10^{10} (from **SEM**)	222	34	8	58	0.4

4.2.2 Effect of buffer layer:

Strain also plays a major role in determining the quality of the InAlN layers [139,151,158-161]. In order to minimise the strain in the top InAlN layer used for device fabrication, high crystalline quality buffer layers are a prerequisite. For this purpose, a thick AlN buffer is often grown on top of the sapphire substrate [139] as the lattice mismatch between sapphire and GaN is 14.8 % where as it is only 12.5 % for AlN [3].

Figure 4.8 shows the schematic of a sample which is similar to those shown in Fig. 4.2 but with an additional AlN buffer layer. For this sample the InAlN layer thickness was also slightly increased in order to find appropriate growth conditions to grow thick epilayers for other applications such as LEDs and LDs.

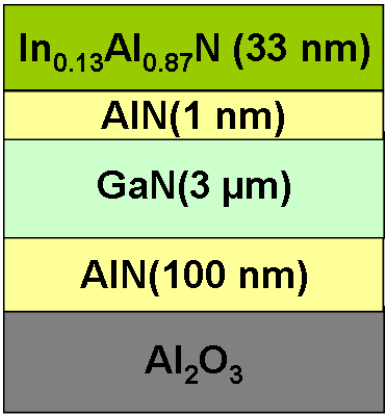

Figure 4.8 Schematic of the sample structure with 100 nm AlN buffer on top of sapphire. The nominal InN composition is of ≈13 % with the intermediate AlN thickness of 1 nm.

The surface morphology of this sample has been analysed using AFM and SE images. Reasonably smooth surface morphology can be seen from the AFM images but the sample has V–defects similar to the sample structure with the 7 nm AlN interlayer. However, there are no surface cracks in this sample. The inset of the SE image shown in Fig. 4.9 shows a high magnification image with the V–defects typically of 20–30 nm in diameter. The total V–defect density from the SE images was estimated to be $2 \pm 0.6 \times 10^{9}$ cm^{-2}.

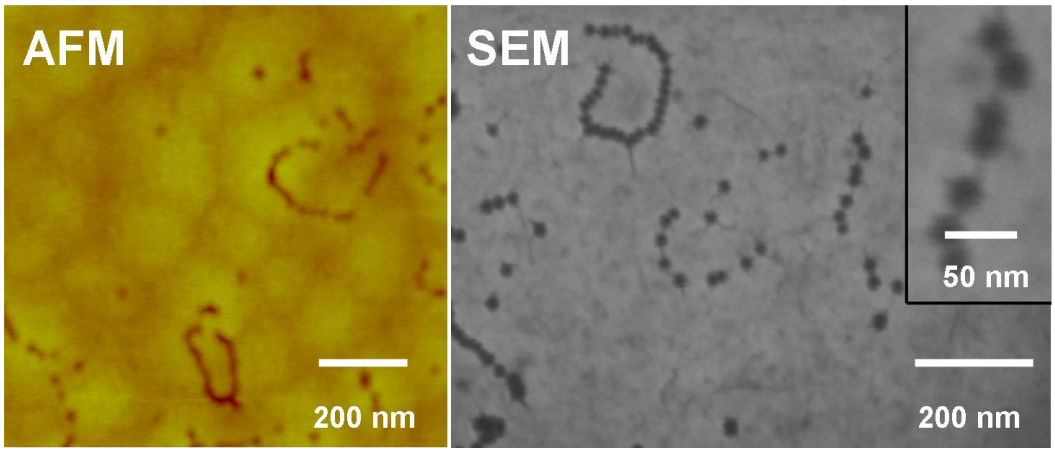

Figure 4.9 AFM and SE images acquired at 5 keV for the InAlN heterostructure with a 100 nm AlN buffer layer. Both AFM and SEM images reveal the V–defects. High magnification plan view V–defect is shown in the inset of the SEM image. (*AFM image- courtesy of Dr. Arantxa Vilalta–Clemente*).

Figure 4.10 shows an electron channelling contrast image revealing low angle tilt or rotation boundaries with V–defects decorating the boundaries and also inside the grains. Cross–section TEM images were acquired for identifying individual dislocation types connected to the bottom of the V–defects. The sample structure was viewed using 2–beam dark field cross–section TEM image with (0002) reflections as shown in Fig. 4.11a and a TD propagating to the surface connected to a V–defect was imaged using a (10-10) reflection (see Fig. 4.11b).

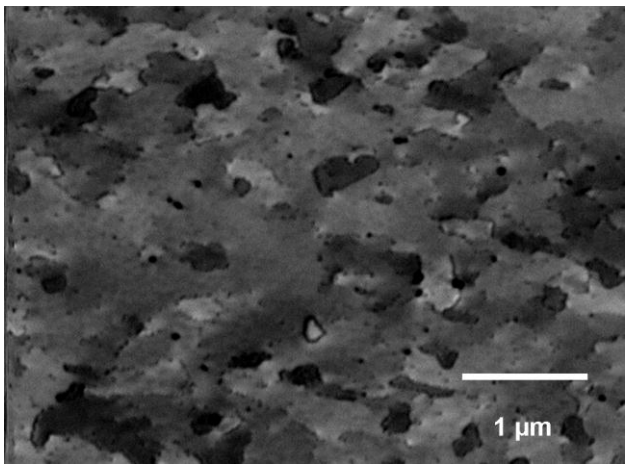

Figure 4.10 electron channelling contrast images for 33 nm thick InAlN layer with 1 nm intermediate AlN interlayer and 100 nm AlN buffer layer.

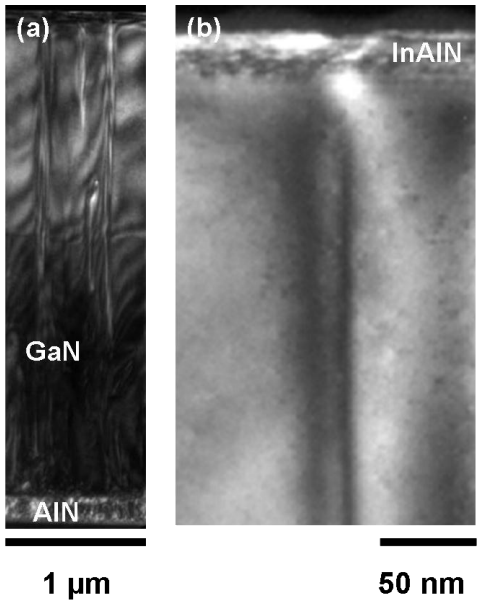

Figure 4.11 cross section TEM images for the sample structure with 100 nm AlN buffer grown on top of sapphire substrate. (a) 2–beam dark field image at 0002 reflections revealing the AlN buffer layer (b) 10-10 reflections showing a TD propagating to the surface and connected to a V–defect.

Many areas of the sample were analysed by cross–section TEM images and it was found that there are ≈ 50% of pure edge dislocations and ≈ 50% of mixed dislocations. No pure screw dislocations were found in the analysed area. Even though the V–defect density is an order of magnitude higher for this sample, the Hall mobility was measured to be $0.9 \times 10^3 cm^2V^{-1}s^{-1}$ [17]. This can be attributed either due to lesser strain on the InAlN layer or the absence of pure screw dislocations.

4.2.3 Effect of substrates:

In order to investigate the role of substrates on structural quality, two InAlN/AlN/GaN HEMT structures grown by Piero Gamarra at III–V labs in France using a low pressure–MOVPE method using an AIXTRON AIX200RF horizontal reactor were characterised using ECCI and cross–sectional TEM. TMGa, TMAl, and TMIn and NH_3 are used as precursors for Ga, Al, In, and N respectively. One of the samples was grown on a 2 inch, 4H–SiC wafer and the other was grown on a 2 inch sapphire wafer. The thickness of the non–intentionally doped GaN buffer layer was 1.6 µm for the sample grown on SiC and 3 µm for sample grown on sapphire. On top of the GaN, a thin AlN interlayer was grown at 1200°C using H_2 as carrier gas. The temperature was then reduced to 865°C for the growth of InAlN barrier layer under nitrogen atmosphere. The schematic of the samples structure is shown in Fig. 4.12.

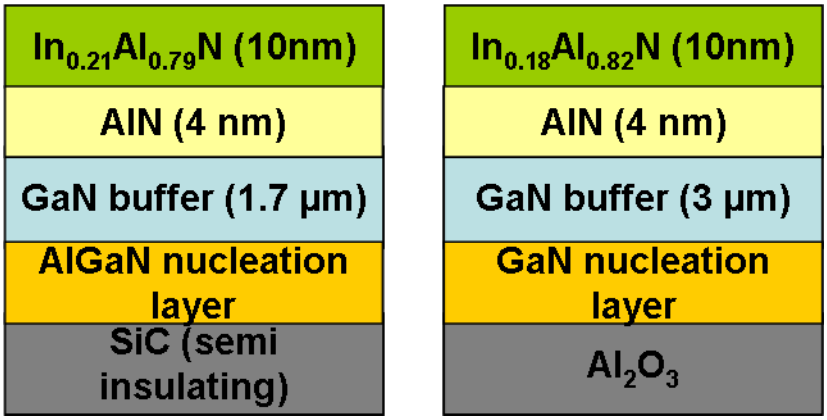

Figure 4.12 Schematic of the sample structure. InAlN on SiC and InAlN on Sapphire.

InAlN heterostructures grown on SiC and sapphire with ≈ 21% and ≈ 18% of InN respectively (estimated by XRD) were investigated using ECCI and cross–sectional TEM respectively for TD densities and their types. In the first case for the heterostructure grown on SiC the InAlN layer is compressively strained whereas for the heterostructure grown on sapphire, it is near lattice matched to the GaN. As discussed previously in this chapter, when the AlN interlayer is of ≈ 7 nm, the surface layer cracks which leads to poor quality device structures. Hence for these structures a 4 nm AlN interlayer is used which has resulted in an electron mobility of 1240 $cm^2V^{-1}s^{-1}$ and 1050 $cm^2V^{-1}s^{-1}$ for the HEMT structure grown on SiC and sapphire substrates respectively [162]. Figure 4.13a shows an electron channelling contrast image of the heterostructure grown on SiC which has a TD density of $1.4 \pm 0.2 \times 10^9 cm^{-2}$ whereas the heterostructure grown on sapphire shows a TD density of $2.4 \pm 0.5 \times 10^9 cm^{-2}$ (see Fig. 4.13b). Note that this is the total TDs density (all the three types of TDs) in the sample. Figure 4.13c and 4.13d are cross–sectional

TEM images acquired in a weak beam (0002) dark field condition which show that the dislocations present in the InAlN layer have propagated from the GaN buffer layers. In these images, only screw and mixed–type dislocations are visible.

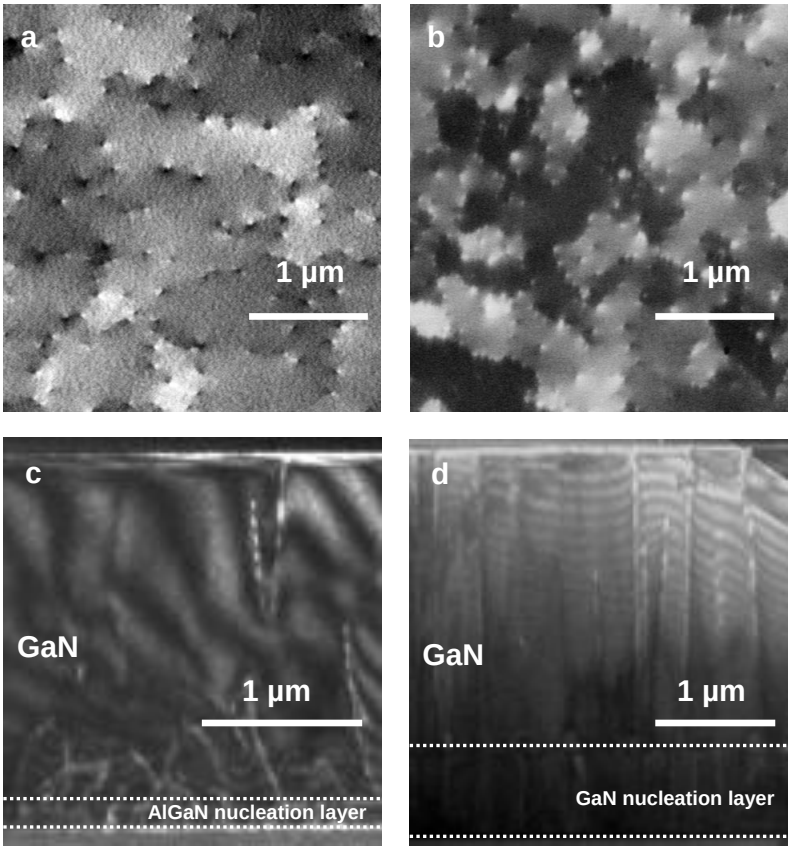

Figure 4.13: (a) ECCI of InAlN on SiC, (b) on sapphire showing tilt and rotation boundaries (high and low contrast regions are due to variation in tilt and rotation across the film), (c) cross section TEM of InAlN on SiC, (d) on sapphire

The HEMT structure grown on SiC contains a negligible fraction of pure screw dislocations (≈ 1%), followed by mixed (≈ 42%) and edge (≈5 7%) respectively. The

structure grown on sapphire exhibits more pure screw dislocations (≈ 10%), followed by mixed (≈ 39%) and edge (≈ 51%) dislocations. A two fold increase in the total TD density for the layers grown on sapphire is attributed to the quality of the GaN buffer layer, which presents a high lattice mismatch with the substrate when compared to SiC. The structure with the higher TD density and more pure screw dislocations has lower electron mobility.

4.3 InAlN/GaN heterostructures for DBRs applications:

The DBR samples were provided by Gatien Cosendy from EPFL Lausanne in Switzerland. For the present work, two samples, one grown on sapphire and the other on free standing GaN were characterised using ECCI to study the influence of substrates on the TDs density for InAlN–based DBRs. Schematic diagrams of (I) near lattice matched $In_{0.18}Al_{0.82}N$/GaN bilayers (40 pairs) of about 3.2 µm in thickness grown on sapphire substrate with a 2 µm GaN buffer layer and (II) $In_{0.20}Al_{0.80}N$/GaN bilayers (42 pairs) with a total thickness of about 3.8 µm grown on a 2 inch c–plane free standing GaN substrate with a 1 µm GaN buffer are shown in Fig. 4.14. The samples were grown in an AIXTRON 200/4 RF–S MOVPE reactor. Detailed description of the growth conditions and the sample optical properties can be found elsewhere [12].

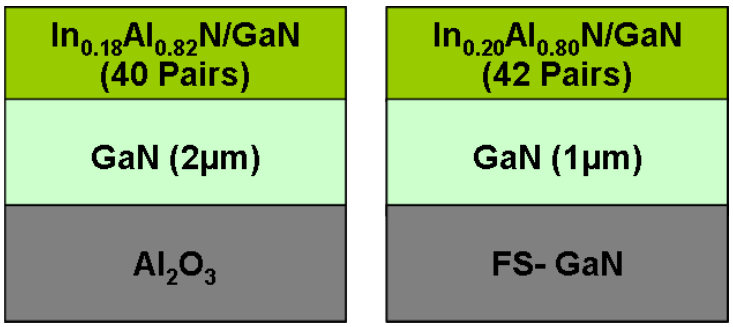

Figure 4.14: Schematic of the DBR sample structure, InAlN on Sapphire and InAlN on free standing GaN.

The free standing GaN was commercially purchased from Lumilog with an estimated TD density of $\approx 4 \times 10^7 cm^{-2}$ (as provided by the manufacturer). In order to compare the difference between TD density of the InAlN DBRs grown on sapphire and free standing GaN and to see if any additional TDs are formed during the growth on free standing GaN, ECCI has been performed on these samples. Figure 4.15 shows electron channelling contrast images for the InAlN grown on sapphire and free standing GaN respectively. Figure 4.15a shows typical features such as TDs, grain boundaries and atomic steps for InAlN DBRs grown on top of sapphire. The total TD density was estimated to be $2.5 \pm 0.5 \times 10^9$ cm^{-2}. For InAlN grown on free standing GaN, the TD density was estimated to be $5 \pm 2 \times 10^7$ cm^{-2} (see Fig. 4.15b). Note the difference in scale bar in Fig. 4.15b when compared to Fig. 4.15a. The free standing GaN template is commercially grown by HVPE where sometimes TDs are not randomly distributed [163]. Hence acquiring images with a larger field of view for TD analysis becomes necessary. The TD density is two orders of magnitude less for the InAlN grown on free standing GaN when compared to InAlN grown on

sapphire. On comparing the TDs densities from ECCI and from the wafer manufacturers, it becomes evident that no additional TDs are formed during DBRs growth on top of free standing GaN. Hence it is important to start the growth with a substrate with fewer TDs.

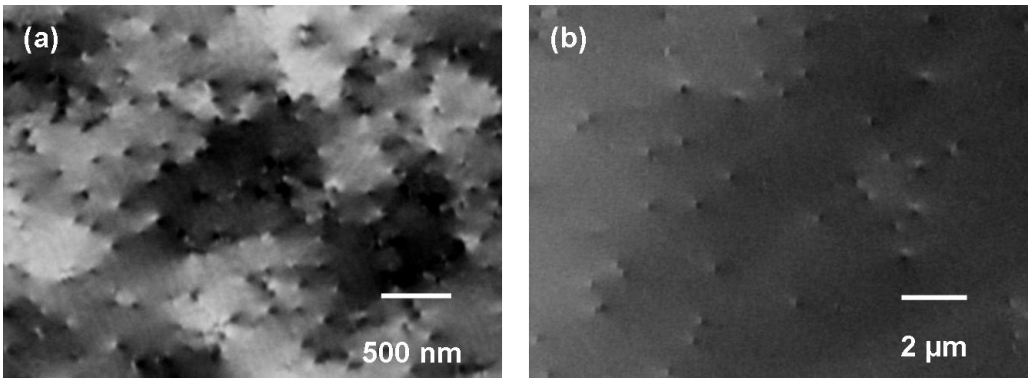

Figure 4.15: (a) ECCI of InAlN on sapphire and (b) on free standing GaN. Note the scale bar in (b) as this sample is grown by HVPE with fewer TDs.

From the knowledge of TDs propagation in HEMT structures gained by cross–section TEM analysis, it is clear that all the TDs appear on InAlN surface have propagated from the underlying substrate and buffer layers and its more probable the same holds good for the DBRs as well. Thus it becomes necessary to optimise the growth of free standing GaN growth process to reduce the total TD densities.

4.4 Summary:

The effect of the AlN interlayer, buffer layers and the role of substrates in determining the quality of the InAlN layers characterised by ECCI is discussed in this chapter. By altering the growth conditions, the V–defects can be eliminated from

the InAlN samples. It appears that dislocations with screw component seem to be more detrimental in undermining the electrical mobility of HEMT structures. It is increasingly important to optimise the growth conditions to reduce pure screw dislocations as well as to reduce the overall TD densities. Additional care has to be taken while growing AlN interlayer to form a smooth interface between InAlN and GaN which confines the 2–DEG and increases the electron mobility. InAlN DBRs grown on free standing GaN shows superior crystal quality in terms of lower TDs density when compared to InAlN/Sapphire. As far as I am aware this is the first ever report on using ECCI for characterising InAlN heterostructures.

Chapter 5

ECCI of GaN thin films grown by nano pendeo coalescence overgrowth

5.1 Introduction:

Technologies for growing high crystalline quality nitrides have improved significantly in recent years. One of the best established methods to grow nitrides with low dislocation densities is the ELOG [164-168] process, which is one of the commercial growth technologies used to produce high quality nitride thin films with TD densities in the range of 10^6 cm^{-2} in the laterally overgrown regions [167-172]. In recent times, the incorporation of nano–rods for the growth of dislocation free nitrides has also attracted significant interest among thin film growers [173]. A promising new technology known as nano pendeo epitaxy (NPE), where the growth on nano–scale patterned substrates such as Si [174-178 SiC [179] Sapphire [180,181] using MOVPE [174, 175, 177, 179] and MBE [176] to produce low dislocation density thin films, has become a popular topic of research amongst the nitrides growth community.

In the present chapter, preliminary results on the application of ECCI for the characterisation of NPE samples are described. ECCI was performed on c–plane GaN grown by nano pendeo coalescence overgrowth using MOVPE to study the effect of various growth parameters involved in NPE, such as the height of the nano–

rods, etch back time of the nano–rod tips and the growth steps of the nano–pyramids which are grown on top of the nano–rods to achieve coalescence overgrowth. TD densities were estimated for all of these samples using ECCI and possible routes for producing high quality NPE thin films are also discussed.

5.2 ELOG:

As mentioned previously ELOG is one of the best growth techniques for producing high crystalline quality nitride thin films with lower dislocation densities [182]. This technique has also been used to produce GaAs thin films and has also been used in Si technology [183, 184]. The fundamental idea of the ELOG technique is the filtering and blocking of extended defects propagating to the thin film surface [185]. Figure 5.2 shows a schematic of typical GaN–ELOG sample structure.

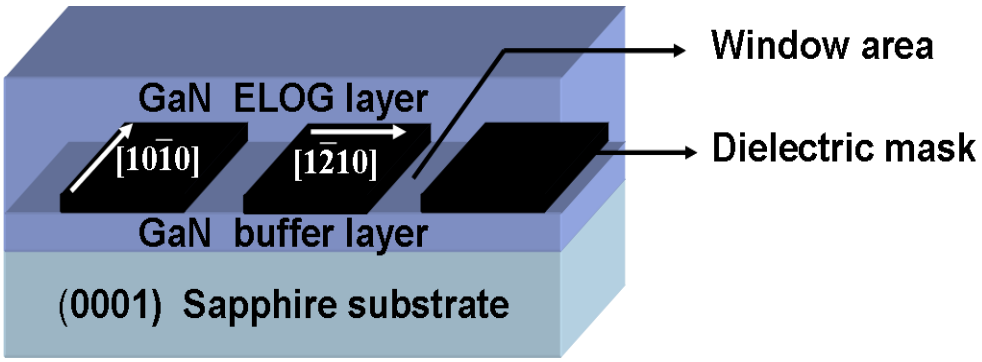

Figure 5.1: Schematic of a GaN–ELOG template showing the wing area and the dielectric mask.

ELOG technology for GaN can be explained as follows: first, GaN layers of a few μm thicknesses are grown on a substrate followed by deposition of a dielectric mask such as SiO_2 or SiN_x. Using photolithographic techniques, a set of parallel stripes separated by window areas is opened in the masks. After this step, regrowth only occurs in the opened regions (window areas) of the mask and no deposition will be observed on the mask. This process is generally referred to as selective area epitaxy or selective area growth. Under appropriate growth conditions, the GaN regrown film reaches the top of the stripes where epitaxial lateral growth takes place over the mask region and finally leads to full coalescence to produce a smooth surface suitable for device fabrication.

Although ELOG technique produces thin films with lower TDs due to blocking of TDs below the mask region, there is also some disadvantage in this approach. TDs originating from the window regions can propagate to the sample surface and hence thick GaN layers (of the order of tens of microns) are necessary to reduce the additional TDs formed in the window regions [3]. This could increase the additional material cost for producing commercially viable devices. In order to overcome this difficulty, NPE method is currently under development.

5.3 NPE:

Pendeo is a Latin word which means to hang or to suspend [174]. Nano heteroepitaxy is a growth method which exploits three–dimensional stress relief mechanisms available with the production of three–dimensional nanoscale features, for instance nano–columns or nano–rods. This allows the minimisation of the strain energy in lattice–mismatched materials [186]. The crucial part in any epitaxy

technique is to achieve good coalescence of grown layers and nano pendeo coalescence is one such approach to produce high quality thin films. There are different schemes that can be used to perform NPE growth. The major schemes that are under investigation are as follows.

1. Performing selective area growth through small holes (in nano–scale dimensions) using a thin dielectric (SiO_2) layer.
2. Etching the nano–rods from a template (GaN/Sapphire) and coalescence of the nano–rods to form continuous layers.
3. Overgrowing nano–pyramids on top of nano–rods and coalescence of the nano–pyramids to form continuous layers.

5.3.1 Selective area growth through small holes:

This method is also known as nano–ELOG where nano–sized patterns typically of hundreds of nm in dimensions are made on the template (buffer layer on a substrate). This allows high quality GaN layers due to the nano–sized growth window that allows three dimensional, prismatic (perpendicular to the base) GaN growth. In principle these layers should be free of defects due to the three–dimensional strain minimising shape of GaN [186]. Following the prismatic growth, the growth temperature can be varied for enhancing the lateral epitaxial growth for coalescence. This step is similar to the normal ELOG method and hence the name nano–ELOG is given to this growth method. The dimensions of the patterns and the growth temperature for the coalescence are the crucial factors in growing good quality GaN layers. Figure 5.2 shows the various steps involved in nano–ELOG method.

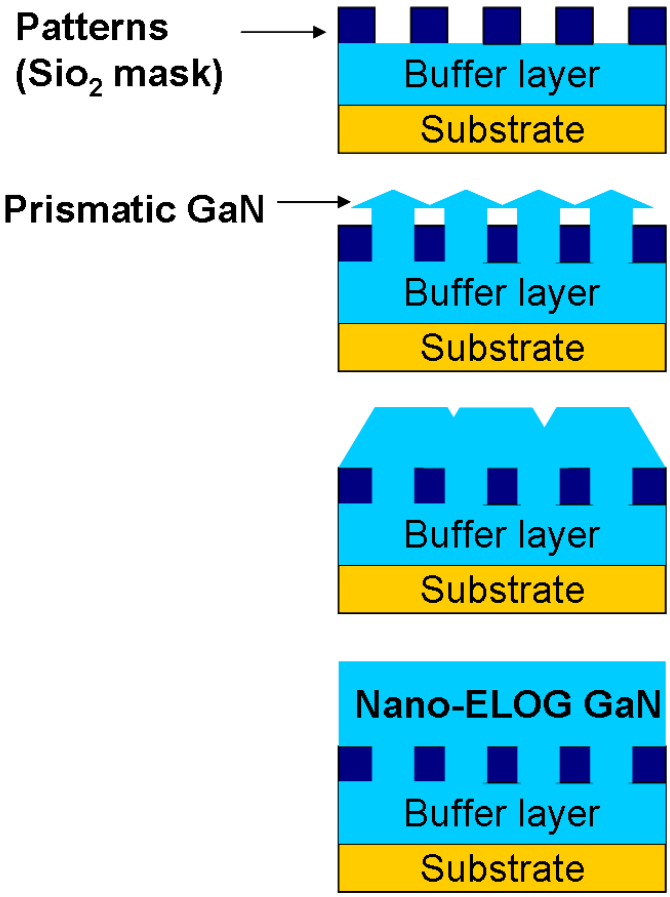

Figure 5.2: Schematic diagrams of steps involved in grown GaN nano–ELOG.

5.3.2 Coalescence of nano–rods to form continuous layers:

In this approach, a GaN template (GaN on a substrate) is used as a starting material. A thin layer of SiO_2 and then a Ni layer is deposited on top of the template. By annealing the sample, Ni nano–dots are formed. The Ni/SiO_2 acts as a mask for preventing the etching of underlying GaN when reactive ion etching and inductively coupled plasma etching is performed to form nano–rods as a next step. The height of the nano–rods can be varied by changing the etching rate. The masks are then

cleaned and thus GaN nano–rods are formed. This is different from the previous approach (see section 5.3.1) where patterned masks were used to form nano–shaped features. The growth conditions such as temperature and the reactor pressure were then altered to form continuous layers by coalescence of the nano–rods. Figure 5.3 shows the various steps involved in the coalescence of the nano–rods to form continuous GaN layers.

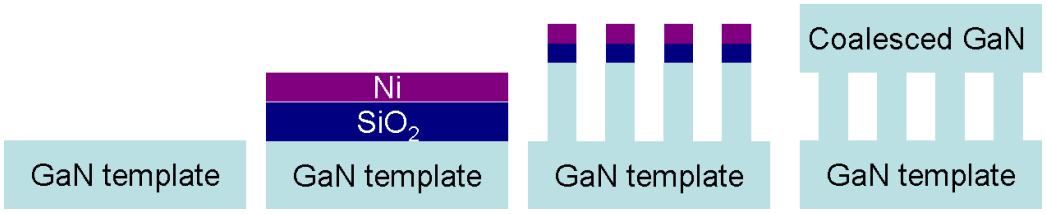

Figure 5.3: Schematic diagrams showing the steps involved in the coalescence of nano–rods to form continuous layers.

5.3.3 Coalescence of nano–pyramids to form continuous layers:

Coalescence of nano–pyramids can be achieved by forming nano–rods using two different approaches as mentioned in section 5.3.1 and 5.3.2. Once the nano–rods are grown, nano–pyramids are grown on top of them and then coalescence of nano–pyramids takes place.

In the present work, the coalesced nano– pyramid samples were grown by depositing masks using electron beam lithography to grow nano–rods and thereafter to further grow nano–pyramids on top of them. Based on the size of the nano features, the mechanism of coalescence differs and hence different approaches are being used. In order to obtain continuous high quality epitaxial layer, a pulsed

growth technique (varying the III–V ratio in pulse mode) is used in both coalescence of nano–rods and nano–pyramids. Figure 5.4 shows the SEM image which shows the etched nano–rods and nano–pyramids grown on top of the nano–rods.

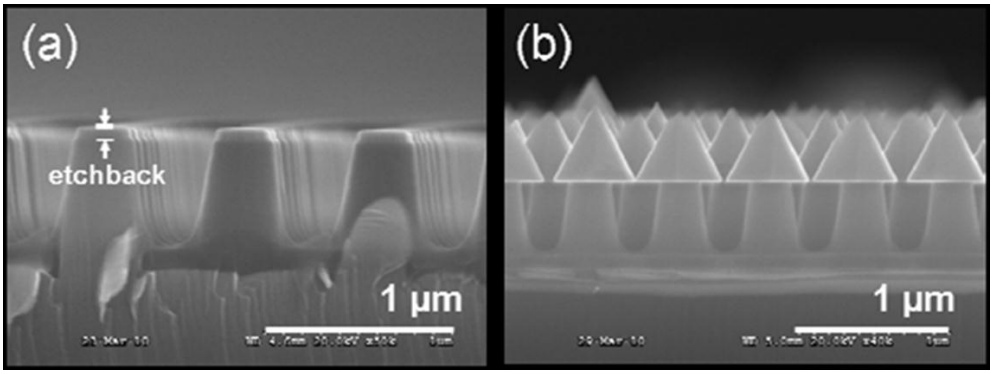

Figure 5.4: Secondary electron images showing (a) the nano–rods and (b) the nano pyramids on top of the nano–rods. [From Ref. 180].

The ratio between the lateral and vertical growth rate is four times larger for NPE when compared with standard ELOG methods [188] which shows the advantage of using NPE but with a drawback; a wavy surface morphology (see section 5.4.1) can be formed due to coalescence boundary misregistry between laterally growing fronts [189]. However, by adjusting growth parameters, GaN layers with fewer dislocations can be produced. This growth technique is in its initial stages of development and it is believed that it will lead to create high quality thin films in near future [180, 185]. More information on NPE growth techniques are given in the references [190-192].

5.4 ECCI of NPE samples:

In the present work, ECCI were performed on samples grown by all the three strategies (see section 5.3) used for growing GaN samples by NPE. The samples were provided by Dr. Philip Shields from the University of Bath and from industrial collaborations (commercial in confidence).

5.4.1 ECCI of nano–ELOG sample:

In order to check if ECCI could be performed on NPE samples, a preliminary sample was grown by nano–ELOG method using an Aixtron 200/4 HT RF–S MOVPE system was investigated. Note that this sample still contains the SiO_2 mask in the grown layers (masks not removed). Figure 5.5 shows an SE image revealing the buried masks region. To see where the TDs are formed in relation to the mask, ECCI was performed on this structure. There are few regions on this sample which are not fully coalesced; however the sample is smooth enough to perform ECCI. Electron channelling contrast images were taken from the fully coalesced regions which are shown in Fig. 5.6.

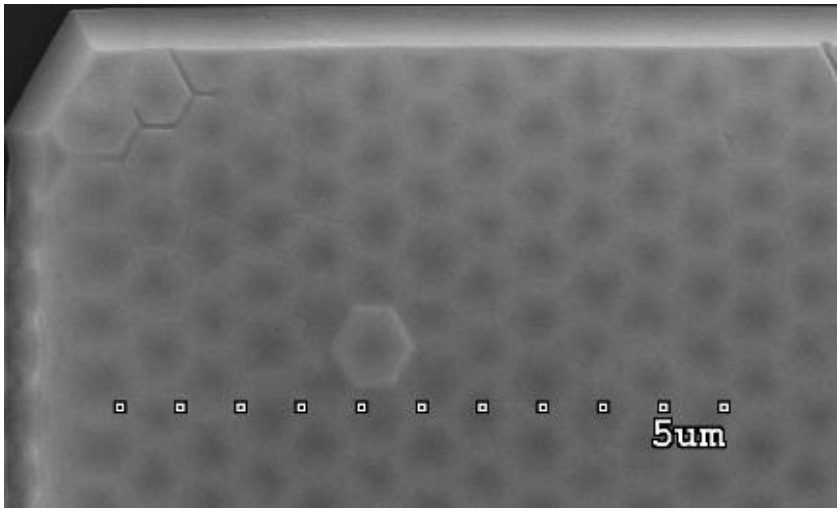

Figure 5.5: Secondary electron image of a nano–ELOG GaN over grown layer revealing the buried masks regions. (*courtesy of Dr. Philip Shields*).

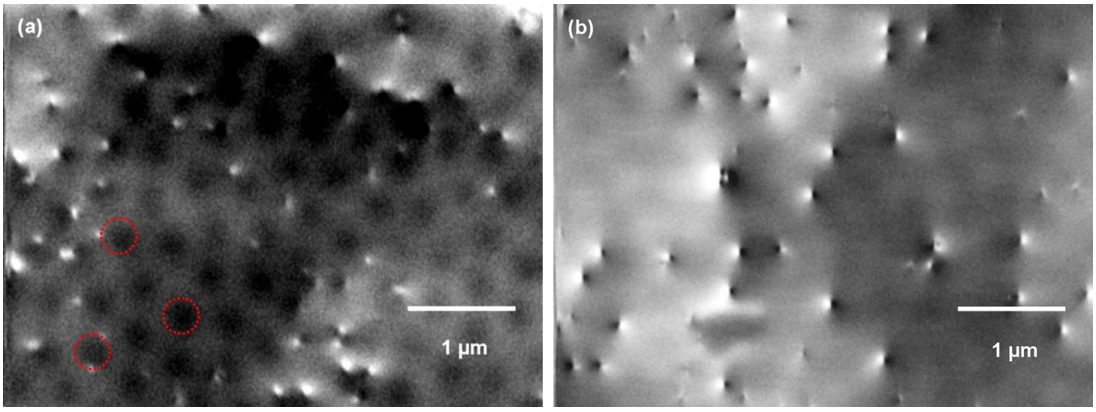

Figure 5.6: Electron channelling contrast images of the nano–ELOG sample (a) showing both buried mask regions and TDs (b) Showing TDs with enhanced channelling contrast for a different channelling condition from the image shown in (a). The mask region is highlighted by dotted red circles. Note that the images are not from the same part of the sample.

Appropriate imaging conditions were selected to reveal the buried mask and to reveal the TDs through channelling contrast. Figure 5.6a shows an electron channelling contrast image revealing the buried mask and also TDs. The imaging conditions were carefully chosen to reveal the underlying mask so that information about the position of the TDs with respect to the buried mask could be obtained. It was found that TDs are not formed in the region above the masked area; the majority of the TDs appear to be formed at the periphery of the mask region. This is shown in Fig. 5.6a where the masks regions are highlighted by dotted red circles. Note that there are also regions where TDs are not formed along the periphery of the mask region. The exact reason for this behaviour is still under investigation.

In order to estimate the total TDs density on the coalesced layers, channelling conditions were changed (different from the channelling image shown in Fig. 5.6a) to reveal TDs with enhanced contrast. The TD density for this sample was estimated to be $3.3 \pm 0.4 \times 10^{8}$ cm^{-2} from the channelling images similar to the one shown in Fig. 5.6b.

5.4.2 Effect of nano rods height:

To investigate the effect of the nano–rod height on the TD densities, samples with different nano–rod heights (50 nm, 200 nm and 325 nm) were grown by using the second approach, i.e. etching the nano–rods from a template (GaN/Sapphire) and coalescence of the nano–rods to form continuous layers. The samples were grown using an Aixtron 200/4 HT RF–S MOVPE system. More information on the growth procedure can be found elsewhere [192].

Figure 5.7 shows cross–sectional SE images showing nano–rods with heights of 50 nm, 200 nm and 350 nm respectively. Plan view SE electron images for these samples reveal the wavy surface morphology which is typical for NPE growth. This is shown in Fig. 5.8; the wavy morphology is best seen in Fig. 5.8a highlighted by the black circle.

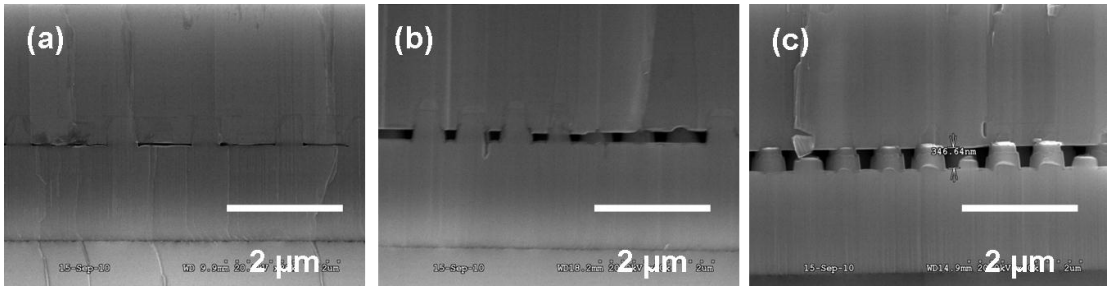

Figure 5.7: Cross section SE images showing nano–rods of different heights (a) 50 nm, (b) 200 nm and (c) 350 nm (*courtesy of sample provider*).

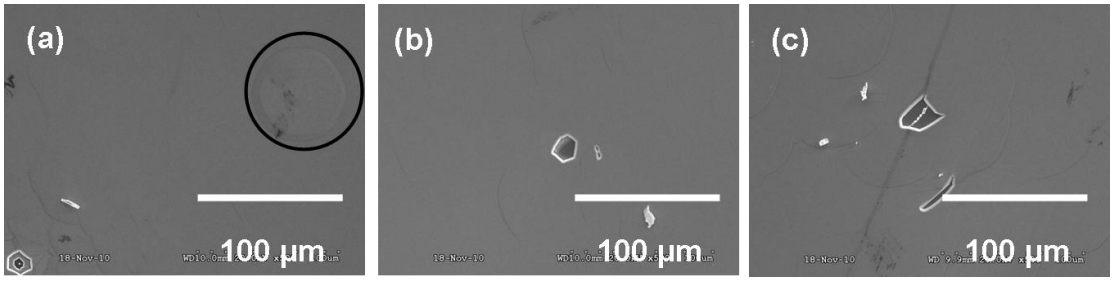

Figure 5.8: plan view SE images showing the surface features for the samples with nano–rods of different heights (a) 50 nm, (b) 200 nm and (c) 350 nm. The black circle highlights the wavy surface morphology *(courtesy of sample provider).*

ECCI were performed on these samples to estimate the TD densities on the sample surface. Figure 5.9 shows the electron channelling contrast images revealing TDs and atomic steps for the samples with nano–rods heights of 50 nm, 200 nm and 350 nm respectively. The TD densities for the sample with nano–rods height of 50 nm was estimated to be $4.5 \pm 0.6 \times 10^8$ cm^{-2} and the TD densities for the sample with 200 nm and 350 nm nano–rods heights was estimated to be $3.5 \pm 0.5 \times 10^8$ cm^{-2} and $3.3 \pm 0.3 \times 10^8$ cm^{-2} respectively. There is no appreciable change in the TD densities for the sample with 200 nm and 350 nm nano–rod heights. Samples with longer nano rods (typically greater 200 nm in height) shows fewer TDs when compared to the sample with shorter nano–rods (50 nm).

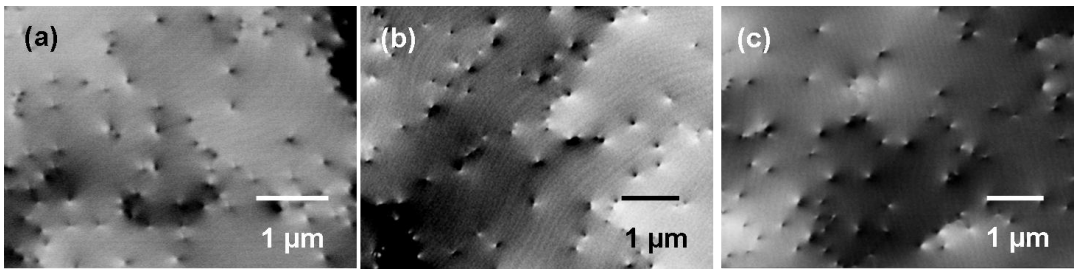

Figure 5.9: Electron channelling contrast images revealing TDs and atomic steps for the samples with different nano–rods height (a) 50 nm, (b) 200 nm and (c) 350 nm.

5.4.3 Effect of nano–rod etching time and growth steps for nano–pyramids:

The third method to achieve good quality NPE samples (by overgrowing nano–pyramids on top of nano–rods and coalescence of the nano–pyramids) was also investigated in the present work. In order to selectively overgrow the nano–pyramids

on top of the nano–rods, the nano–rods have to be etched and passivated. To see if there is any effect of etching time of the nano–rods on the TD density; ECCI was performed on two samples with 90 and 150 seconds etch back time. More information on nano–rods fabrication of these samples can be found elsewhere [180]. Figure 5.10a and 5.10b show plan view SE images for these samples. Both these samples have voids (see Fig.5.10a) which may be due to incomplete growth in some areas and the wavy surface morphology as described earlier (see Fig.5.10b). However, there are areas with fully coalesced regions with smooth surface morphology from which it was possible to acquire electron channelling contrast images.

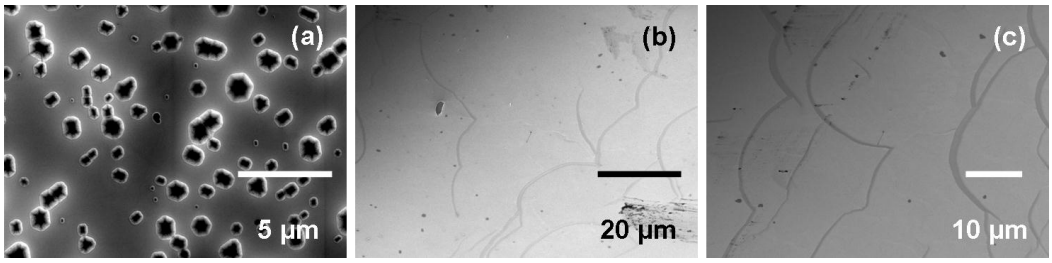

Figure 5.10: Plan view SE images taken at 5 keV showing the surface features for the samples with different etch back time for the nano–rod and different nano–pyramid growth step (a) 90 seconds etch back time and 500 nm growth step (b) 150 seconds etch back time and 500 nm growth and (c) nano–pyramid growth step of 600 nm and etch back time of 90 seconds.

ECCI were performed on these samples to estimate the TD densities. Figure 5.11a and 5.11b shows the electron channelling contrast images for the samples with 90 seconds and 150 seconds etch back time where the TD densities was estimated to

be 4.5 ± 0.6 × 10^8 cm^{-2} and 3.5 ± 0.4 × 10^8 cm^{-2} respectively. The longer etch back time (150 seconds) sample exhibits a lower TD density and thus it becomes clear that the etching time is an important factor in determining the sample quality in terms of TD densities.

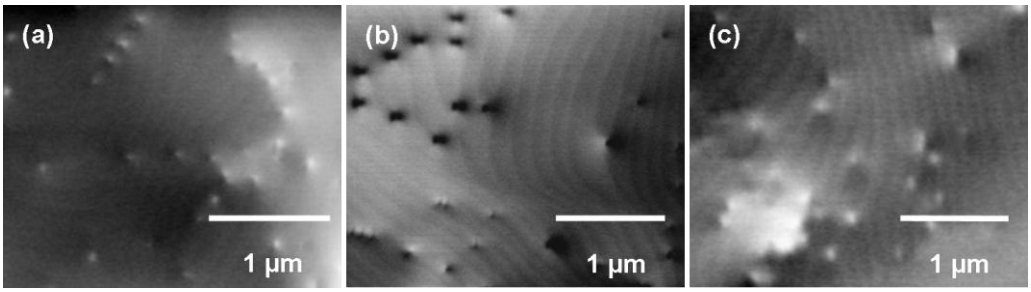

Figure 5.11: Electron channelling contrast images revealing TDs and atomic steps for the samples with different etch back time and nano–pyramid growth step (a) 90 seconds etch back time and 500 nm growth step (b) 150 seconds etch back time and 500 nm growth and (c) nano–pyramid growth step of 600 nm and etch back time of 90 seconds.

The distance between centres of the nano–pyramids is known as the growth step. In order to see if there is any effect on the growth step on the TD density, ECCI was performed on two samples with 500 nm and 600 nm growth steps. Note the nano–rods etch back time is maintained the same for these samples (90 seconds). Figure 5.10a and 5.10c show plan view SE images for these samples.

ECCI were performed on these samples to estimate the TD densities. Figure 5.11a and 5.11c shows the electron channelling contrast images for the samples with 500 nm and 600 nm growth steps where the TD densities was estimated to be 4.5 ± 0.6 × 10^8 cm^{-2} and 3.3 ± 0.4 × 10^8 cm^{-2} respectively. Larger growth step (600

nm) sample shows fewer TD densities and thus it becomes clear that the growth step is also one of the important factors in determining the sample quality in terms of TD densities.

5.5 Summary:

The application of ECCI for determining the TDs density in coalesced GaN epitaxial layers obtained through a new type of growth method namely NPE is demonstrated in this chapter. From this preliminary study, it becomes clear that by varying the important parameters such as etch back time of the nano–rods and growth steps for nano–pyramids, TDs density can be reduced. To grow samples with fewer TD densities, longer nano–rods with longer etch back time and larger growth steps for nano–pyramids should be preferred. Although the TD densities in the order of be $3–4 \times 10^{8}$ cm^{-2} for the samples grown by all the three different approaches of NPE , it is a promising technique for producing high quality nitride thin films in near future. This can be realised by optimising various growth parameters and more work is in progress by the thin film growers on this topic.

Chapter 6

Coincident ECCI and CL imaging of TDs in GaN

6.1 Introduction:

In spite of TDs being detrimental to optoelectronic device performance, nitride devices with TDs in the range of 10^8 cm^{-2} still operate, which is not the case for arsenide or phosphide structures [193-195]. This interesting property of nitrides attracts both the experimentalist and the theorist to investigate the role of defects in optical and electronic properties of nitride based semiconductor devices.

In this chapter, combining ECCI with CL imaging in a scanning electron microscope is demonstrated for the first time. Images from exactly the same micron–scale region of a Si doped GaN thin film sample were acquired. This allows a simple and direct investigation of the influence of extended defects on the light emission from nitride based semiconductors. The preliminary results from those coincident ECCI–CL measurements are discussed and a detailed description of CL–hyperspectral imaging and the Strathclyde CL facility is also presented.

6.2 Defect analysis using CL spectroscopy/imaging:

When an incident electron beam interacts with the sample under investigation, electron–hole pairs are generated due to impact ionization. The carriers generated in the semiconductor could undergo diffusion and/or drift followed by recombination which gives rise to CL emission. This is the basic principle of CL [196-198]. Recombination of electron–hole pairs may also occur in a non–radiative process (no emission of light), for instance, direct conversion of the emitted electron energy into heat [199] and recombination due to surface states (electronic states at the surface of the material) or at defects.

In CL imaging, defects can appear as dark contrast due to enhanced non–radiative recombination. Thus defective areas in the crystal can be readily identified [199]. It has been suggested that, defects could introduce two types of energy levels into the band gap, namely narrow energy bands and shallow trapping potentials [200-202]. Generally narrow energy bands appear near the middle of the gap and are possibly associated with the dangling bonds while shallow trapping potentials are introduced by the localised deformation potential due to the elastic strain field around dislocations [202, 203]. TDs frequently appear as dark spots showing two types of contrast. Dark dot contrast is seen for lightly doped semiconductors, while dot and halo contrast is seen in more heavily doped materials [199].

The important question to be answered while analysing dislocation contrast in CL imaging is to determine whether the recombination is due to the inherent structure of the dislocation itself (i.e. bonds associated with the electronic structure of the dislocation core) or the presence of point defects (i.e. impurities or vacancies) at or around the dislocation. Experimentally it was found that both dislocation core

and point defect effects might be involved in the observed dislocation CL contrast [200]. Thus in order to compare the luminescence features, knowledge of defect concentrations becomes essential.

It has been suggested that TDs are one of the main types of extended defects that cause the non–radiative recombination in nitrides [199, 203]. Although TDs are observed to cause non–radiative recombination, there is an increased speculation about how a specific type of dislocation (edge, screw or mixed) quench the luminescence in nitride semiconductors [38, 204-206]. It has been argued that all types of TDs act as non–radiative recombination centers in GaN [207], however there are also reports of only screw type dislocations acting as non–radiative recombination centers [208, 209]. Possible reasons for this ambiguity can be due to the analysed samples themselves (e.g. growth method, quality of the samples, impurities) or the characterisation techniques used to correlate TDs with luminescence properties. Some characterisation techniques require sample preparation which might also change the environment of the dislocation features, while others give only indirect information on dislocations.

CL is one of the most widely used techniques to study defects in nitride semiconductors [210] and variations in the CL emission features can be related to, for example, alloying, strain, and doping or carrier concentration [199, 210]. CL can be used to obtain both spectrally and spatially resolved luminescence properties of materials. The spectral distribution of the emitted light signals is referred to as CL spectroscopy and when the intensity of the light emission is mapped in 2–D space, the technique becomes CL microscopy or imaging. CL imaging is often combined with other defect characterisation techniques such as electron beam induced current

[211], SE imaging in SEM [156], AFM [212], TEM [207] or STEM [201] to correlate between structural and optical properties. Most of these methods either require sample preparation or need two different instruments to have a direct correlation between TDs and luminescence properties of the material under investigation.

In order to overcome these practical difficulties, a simple and rapid approach has to be employed to correlate TDs and their luminescence properties. To fulfill this ambition, CL imaging has been performed in the same FE–SEM system where ECCI (*see chapter two*) was performed.

6.3 CL spectroscopy and hyperspectral imaging system at the University of Strathclyde:

The most common way to perform CL experiments is by using a scanning electron microscope, equipped with suitable light collection and detection systems [199]. Figure 6.1 shows the picture of the modified SEM–CL set up and Fig. 6.2 shows the schematic of the same used in the present work. This modified SEM–CL set up was built by Dr. Paul Edwards from the Semiconductor Devices and Spectroscopy research group, University of Strathclyde. The sample surface is kept at 45° to the incident electron beam and the emitted light is collected and collimated by a reflecting objective (NA 0.28) which is then directed to a 90° off–axis paraboloidal aluminium mirror through a quartz vacuum window. The paraboloidal mirror directs and focuses the collimated light to the entrance slit (25 μm or 100 μm) of 12.5 cm focal length (Oriel MS125) spectrograph. A 1 inch length electron multiplied (EM) charge coupled device (CCD) (Andor Newton) camera used for the

CL imaging. The EMCCD array employs better electronics than the normal CCD with lower signal to noise ratio and reduces the time required to acquire each spectrum (in the range of tens of milliseconds) and the complete spectroscopic information is acquired using a single electron beam scan, reduce the possibility of sample damage due to electron beam irradiation. The CCD on the FE–SEM has 1600 pixels with each pixel of width 16 μm. Note that the reflecting objective is inside the scanning electron microscope chamber and the other components are outside the SEM chamber.

Figure 6.1: Photograph of the modified FESEM–CL set up at the University of Strathclyde.

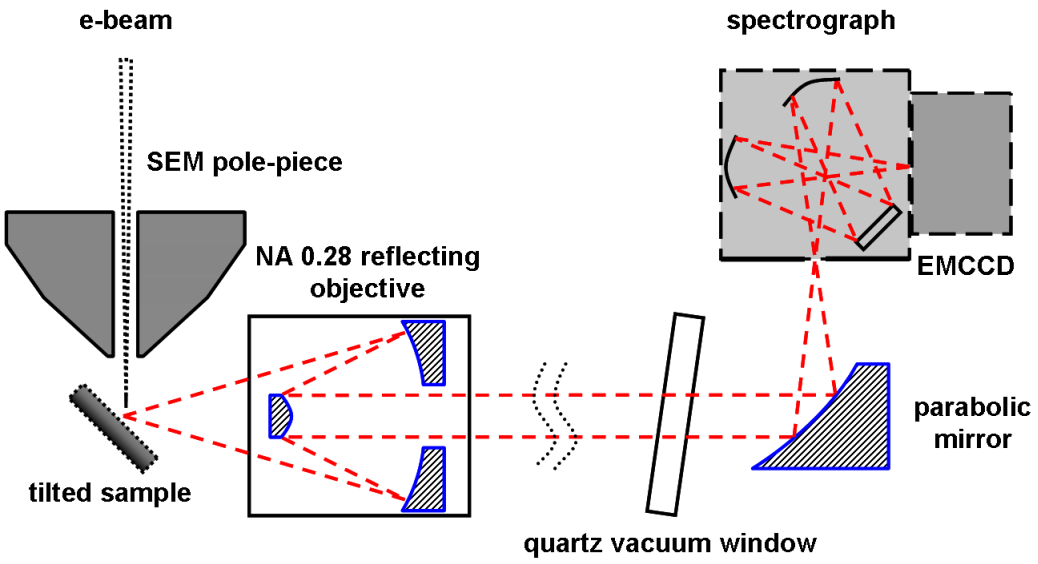

Figure 6.2: Schematic of the modified FESEM–CL set up with various components. The sample is tilted at 45° to the incident beam.

One of the important aspects in any characterisation technique is its acquisition and data analysis system. In CL–hyperspectral imaging, the electron beam is scanned across the sample surface while simultaneously a CL spectrum is acquired from each point on the surface resulting in a multi–dimensional data set [213]. This hyperspectral image is also referred to as a spectrum image, or a spectrum map [213, 214]. A typical hyperspectral image is of 256 × 256 pixels acquired using in–house developed software known as CHIMP developed by Dr. Paul Edwards [156, 210, 214]. CL can also be performed as a function of the electron beam voltage, current or sample temperature. In the present experimental setup, only room temperature CL can be performed. Thus all the CL images shown in this chapter are from room temperature measurements.

6.4 Sample description:

The c–plane GaN thin film was provided by Dr. Rachel Oliver from the University of Cambridge. The Si doped GaN thin film was grown by MOVPE technique in a 6 × 2″ Thomas Swan close–coupled showerhead reactor, using TMG, SiH_4 at 50 ppm in H_2, and NH_3 as precursors and H_2 as a carrier gas. Figure 6.3 shows the schematic of the sample used in the present work. This multilayered sample structure was prepared by the growers to demonstrate the application of scanning capacitance microscopy for analysing carrier concentrations. The Si concentration in the top layer was estimated to vary between 3×10^{18}–1×10^{19} cm^{-3} using secondary ion mass spectrometry and scanning capacitance microscopy measurements [212]. Optimum electron beam conditions were chosen to make sure that luminescence information is obtained from the top 200 nm GaN layer. Thus one

can consider that the CL and ECCI are obtained from the Si doped GaN layer. More information on the sample and its growth conditions can be found elsewhere [212].

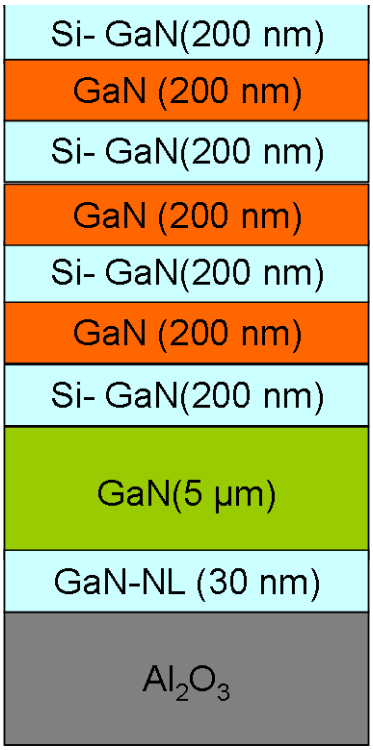

Figure 6.3: Schematic of the sample structure. A nucleation layer (NL) is grown prior growing the other layers to promote the 3–D growth. Please note that the top layer is Si doped.

6.5 ECCI of c–GaN:

As mentioned earlier in this chapter, in order to understand the luminescence intensities of the sample under investigation, knowledge of defect concentration becomes important. In order to achieve statistically reliable TD densities, ECCI was

performed. In ECCI, vertical TDs generally appear as spots with B–W contrast as explained in *chapter two*. Figure 6.4 shows a typical electron channelling contrast image of the GaN film, the inset shows one of the TDs with a higher magnification. The total TD density was estimated to be $5.1 \pm 0.4 \times 10^{8}$ cm^{-2}. By following the procedure which exploits differences observed in the direction of the B–W contrast for screw, edge and mixed dislocations for two electron channelling contrast images acquired from two symmetrically equivalent crystal planes, the ratio of individual dislocations types were estimated (*see chapter two*). It was determined that 60 % of TDs observed in the GaN film are edge type, 38 % are mixed and 2% are screw type.

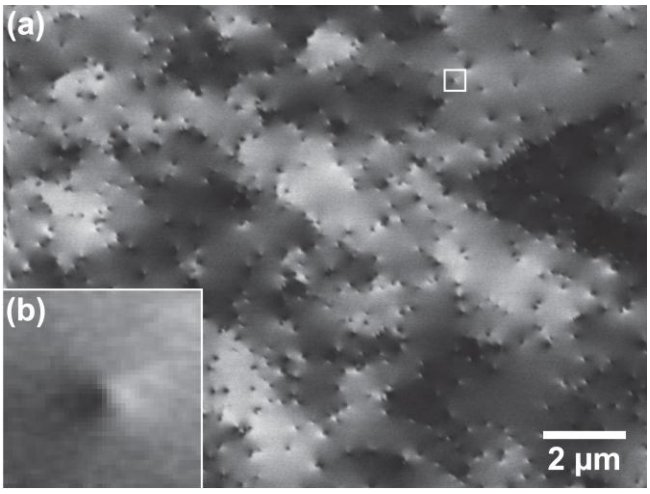

Figure 6.4: (a) Electron channelling contrast image of GaN thin film revealing TDs and areas of different tilt and rotation of the crystal and are seen as regions with different grey scales (grains). (b) The inset shows a magnification of the marked TD displaying the typical B–W contrast for a TD. The area of the inset is 500 × 500 nm^2 area.

6.6 CL imaging of c–GaN:

The electron beam energy (acceleration voltage) is a crucial parameter that can be varied to excite different parts of the sample, i.e. lower accelerating voltage excites the sampling area closer to the surface and higher accelerating voltage excites deeper in to the sample [215]. In the present work, CL imaging was performed with an electron beam spot size of ≈ 17 nm, a beam current of ≈ 6 nA and accelerating voltage of 5 keV. At these conditions the electron beam energy deposition will be within ≈ 200 nm thickness as estimated by using Monte Carlo simulations [216]. Thus the luminescence information will be from the top 200 nm GaN layer.

In the case of the GaN, the main emission peaks originate from the band edge emission [217]. Figure 6.5a shows a CL peak intensity map for GaN near band edge emission showing dark spots which are associated with TDs. Some of the dark spots are small and others are strong (intense darker spot) and large. The larger spots can be due to two or more dislocations clustered together. Thus obtaining a statistically reliable TD density becomes difficult [218]. Figure 6.5b displays the CL peak energy map extracted from the CL hyperspectral image of the same area exhibiting variations in the peak energy, which is probably due to strain and/or variation in Si doping in the sample during the growth. The CL maps were gained by numerically fitting each individual spectrum in the hyperspectral data set using a pseudo–Voigt function for the GaN emission peak. The band edge energy for a bulk un–strained wurtzite GaN is 3.42 eV [219]. When compared to this value, the band edge energy of the c–GaN used in the present work is 3.43 eV, thus there is an energy change in the order of 10 meV, showing that the sample is slightly under compressive strain.

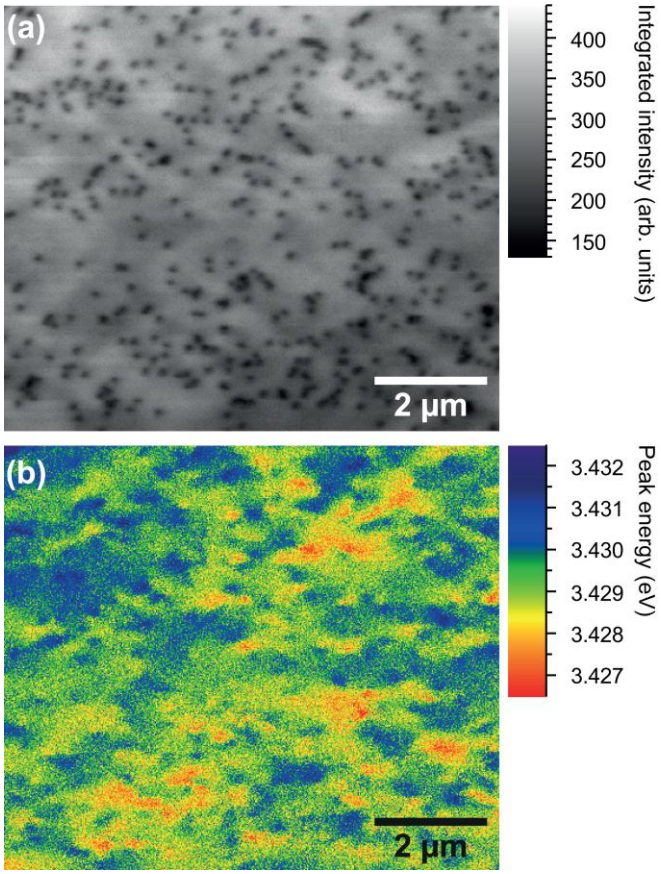

Figure 6.5: (a) Peak intensity map and (b) CL energy map of the GaN near band edge emission acquired at 5 KeV. The CL maps were gained by numerically fitting each individual spectrum in the hyperspectral data set using a pseudo–Voigt function for the GaN emission peak. TDs are shown as dark spots of reduced intensity. The energy map (b) reveals small shifts in energy due to strain variations or doping in the sample *(courtesy of Jochen Bruckbauer).*

6.7 Coincident ECCI and CL hyperspectral imaging:

In order to find out if all the type of TDs act as non–radiative recombination centers for this particular sample, it becomes necessary to compare CL with ECCI. Figure 6.6 shows an ECCI and CL intensity image acquired from exactly the same micron–scale area. For the sake of clarity only a smaller area is showed in the present work. The original data set is of ≈ 150 μm^2 in area with ≈ 750 dislocations where ≈ 400 dislocations were found to be isolated and the remaining are clustered (more than two dislocations near to each other). Note that ECCI measurements were performed before CL imaging to avoid any surface contamination which reduces the clarity of channelling images. The images were aligned to match the same area due to the difference in geometries involved in ECCI and CL imaging.

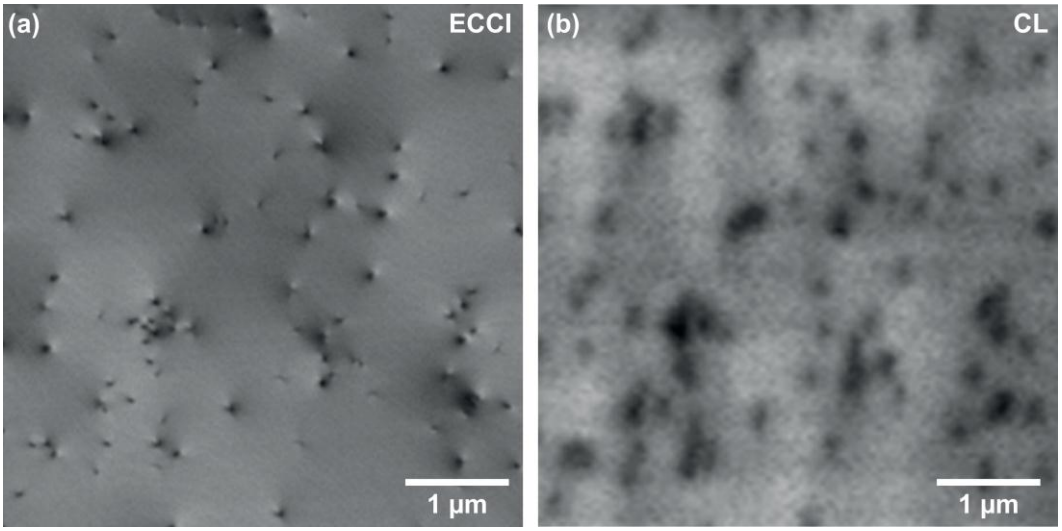

Figure 6.6: (a) Electron channeling images and (b) CL intensity imaging from the same micron–scale area. TDs appearing as spot with B–W contrast in ECCI appear as dark spots in CL revealing a direct correlation of TDs between both techniques.

A comparison of both images shows a one–to–one correlation for isolated TDs in ECCI and with dark spots in CL imaging. Fig. 6.6a displays regions of TDs, where more TDs are clustered together. In those regions, it was not possible to unambiguously determine if all the dislocations in the clusters corresponds to the larger dark spots in the CL image. The larger dark spots areas in the CL image are shown in Fig. 6.6b. AFM images were also acquired from the same part of the sample (images not shown here) revealing that isolated dislocations are of both edge and screw/mixed character. Thus one may come to the conclusion that pure edge dislocations and dislocations with screw component appear to act as non–radiative recombination centers for the analysed sample.

6.8 Summary:

The application of ECCI for imaging TDs and comparing the same using CL hyperspectral imaging in a scanning electron microscope is demonstrated for the first time. A one–to–one correlation between isolated TDs as seen as B–W contrast in ECCI and as black spots in CL imaging is observed in the case of Si doped c–plane GaN layer. This gives reliable information on TDs acting as non–radiative recombination centers in the analysed sample. This new approach of combining ECCI and CL imaging can be used for other nitrides alloys and semiconductor materials with different dopants and doping concentration to understand the role of extended defects on optical properties.

Chapter 7

Conclusions and suggestions for further work

7.1 Introduction:

This thesis presents the results of a three–year investigation into the scanning electron microscopy technique of electron channelling contrast imaging. The aim of the project was to develop a rapid and non–destructive structural characterisation technique for characterising extended defects in nitride semiconductors. In this chapter, section 7.2 summaries the thesis chapter by chapter, highlighting key results and conclusions. Section 7.3 discusses areas where more work could be performed which may possibly open up new areas for further study.

7.2 General conclusions and comments:

The use of electron channelling contrast imaging in the scanning electron microscope to rapidly and reliably image and identify TDs in materials with the wurtzite crystal structure (e.g. GaN) was discussed in *chapter two*. In electron channelling contrast imaging, vertical TDs are revealed as spots with a B–W contrast. A simple geometric procedure was developed which exploits the differences observed in the direction of this B–W contrast for screw, edge, and mixed dislocations for two electron channelling contrast images acquired from two symmetrically equivalent crystal planes whose $\boldsymbol{g}$ vectors are at 120° to each other.

This approach allows unambiguous identification of all TDs without the need to compare results with dynamical simulations of channelling contrast. An order of magnitude reduction in the time required to obtain quantitative information on dislocations is envisaged compared to presently available techniques.

In *chapter three*, it was demonstrated that electron channelling contrast imaging is an excellent technique for rapid and non–destructive quantification of PDs and SF densities in non–polar nitrides. SFs and PDs were visualized for the first time in non–polar nitrides and statistically significant information was obtained using ECCI.

The application of ECCI technique for characterising InAlN/AlN/GaN, InAlN/GaN heterostructures for HEMTs and DBRs respectively was discussed in *chapter four*. It appears that dislocations with a screw component are detrimental in undermining the electrical mobility of HEMT structures and hence it becomes increasingly important to optimise the growth conditions to reduce screw dislocations as well as to reduce the overall threading dislocation densities.

The use of ECCI to characterise GaN grown by a relatively new growth technique, namely NPE where the thin film growth initiates from nano–rods is demonstrated in *chapter five*. These preliminary studies indicates that by varying the parameters such as etch back time of the nano–rods and growth steps for nano–pyramids, TD densities can be reduced. To grow samples with fewer TD densities, longer nano–rods with longer etch back time and larger growth steps for nano–pyramids appear to be advantageous.

In *chapter six*, a new approach of combining ECCI and CL imaging has been demonstrated for the first time. A direct correlation between TDs revealed by ECCI

appearing a B–W spots and black spots in CL imaging was obtained. Electron channelling contrast images and CL images can be acquired over a large area giving statistically significant information on TDs acting as non–radiative recombination centers. The correlation of ECCI and CL imaging allows the effect of TDs on light emission to be directly observed all in one instrument.

7.3 suggestions for further work:

There are two broad areas where future work could be directed. Applying ECCI to a wide range of materials and the improvement of the technique itself.

1. ECCI could be used to characterise the full range of nitride materials i.e. AlN, InN, AlGaN, and InAlGaN grown on different growth planes and substrates and by different growth techniques.
2. ECCI could be performed in a variable pressure FE–SEM for high Al containing samples, thus avoiding charging effects which presently limits the characterisation of AlN.
3. ECCI could also be applied to characterising other semiconductor materials with the wurtzite crystal structure such as ZnO. Its application could also be extended for materials with other crystal structures such as diamond and zincblende structures [85].
4. Coincident CL imaging and ECCI for semiconductor thin films with different dopants and doping concentration could be performed. This would help in understanding the influence of dislocations with different dopants on light emission characteristics.

5. New possibilities for using ECCI for semiconductor devices failure analysis could also be explored i.e.: role of screw type dislocations on device performance.
6. Beam divergence is one of the factors that limit the resolution of electron channelling in a scanning electron microscope, hence experiments need to be performed with different aperture sizes and beam parameters which could help in improving the resolution of ECCI.
7. Energy dependent ECCI can be performed which may give more information on the depth dependence of defects on the samples under investigation.
8. ECCI could also be coupled with other SEM modes such as wavelength dispersive X–ray analysis and EBIC in addition to CL to have a direct correlation of structural, composition, electrical and optical properties of semiconductors all in the same instrument.
9. ECCI could also be coupled with EBSD to investigate the low angle grain boundaries as revealed by ECCI and quantify tilt and rotations in thin film structures.
10. *Rocking* the sample or the electron beam becomes necessary for acquiring selected area channelling patterns [220]. This opens up a new area for quantification of defects in nano structures and for samples where large area ECPs could not be acquired due to poor sample quality.

11. Automated TDs counting will reduce the data analysis time, thus new software programmes need to be developed to address this issue.

12. Finally, dynamical simulation for channelling contrast [43, 83] could be performed to compare the experimental images to that of the simulated images to improve the reliability in the analysis of extended defects for materials with different crystal structures.

References

1. F. Schubert, *Light–emitting diodes*, Cambridge University press, London (2003).
2. S. P. DenBaars, *Introduction to Nitride Semiconductor Blue Lasers and Light Emitting Diodes*, CRC press, Newyork (2000).
3. H. Morkoc, *Handbook of Nitride Semiconductors and Devices*, Wiley-VCH, Germany (2008).
4. P. Ruterana, M. Albrecht and J. Neugebauer, *Nitride Semiconductors Handbook on Materials and Devices*, Wiley-VCH, Weinheim (2003).
5. H. M. Ng, A. Chowdhuri, *Ill-Nitride Semiconductor Materials*, Imperial college press, London (2006).
6. T. D. Veal, C. F. McConville and W. J. Schaff, *Indium Nitride and related alloys*, CRC press, Newyork, 2009).
7. H. Xia, Q. Xia and A. L. Ruoff, Phy. Rev. B, **45**, 12925 (1993).
8. B. Gil, *Group III Nitride Semiconductor Compounds: Physics and Applications*, Oxford University Press, London (1998).
9. S. F. Chichibu, Y. Kawakami and T. Sota, *Introduction to nitride semiconductor blue lasers and light emitting diode*, CRC Press, New York (1999).
10. S. Shionoya, *Luminescence of Solids*, Plenum Press, New York (1998).
11. S. Nishimura, S. Matsumoto, K. Terashima, Opt. Mat. **19**, 223 (2002).
12. W. C. Johnson, J. B. Parson, M. C. Crew, J. Phys. Chem. **36**, 2651 (1932).
13. J. I. Pankove, E. A. Miller, J. E. Berkeyheiser, J. Luminescence **5**, 84 (1972).

14. H. Amano, M. Kito, K. Hiramatsu and I. Akasaki, Jpn. J. Appl. Phys. **28**, 2112 (1989).

15. G. F. S. Nakamura, *The Blue Laser Diode*, Springer, Newyork (1997).

16. S. J. Pearton, *GaN and Related Materials*, Gordon & Breach science publishers, Newyork (1997)

17. M. Henini, III-V reviews, **9**, 32 (1996).

18. R. Davis, A. Roskowski, E. Preble, J. Speck, B. Heying, J. Freitas, E. Glaser, W. Carlos, Proc. IEEE **90**, 993 (2004).

19. N. Nakamura, MRS Bulletin Warrendale, 1145 (1998).

20. A. Alam, O. Schon, B. Schineller, M. Heuken, H. Jurgensen, Phys. Stat. Sol. A **180**, 109 (2000).

21. J. Redwing, T. Kuech, *Properties, Processing and Applications of GaN Nitride and Related Semiconductors*, IEE INSPEC, London, **416** (1999).

22. F. Ren, J. Zolper, *Wide Energy Bandgap Electronic Devices*, world scientific publishers, New Jersey (2003).

23. T. Paskova, Phys. Status Solidi B, **245**, 1011(2008).

24. D. B. Holt and B. G. Yacobi, *Extended defects in semiconductors*, Cambridge university press, Newyork, (2007).

25. *http://courses.eas.ualberta.ca/eas421/diagramspublic/bergerslarge.gif* (date of access-09/04/2012).

26. C. Stampfl and C. G .Van de Walle, Phys. Rev. B **57**, 15052 (1998).

27. L. Kirste, S. Moller, R. Kiefer, R. Quay, K. K¨ohler, N. Herres, Appl. Surf. Science **253**, 209 (2006).

28. Y. Wu, M. Moore, A. Abrahamsen, M. Jacob-Mitos, P. Parikh, S. Heikman, A. Burk, *IEDM Technical Digest*, Washington DC, **405** (2007).

29. D. Look, Phys. Stat. Sol. B **228**, 293 (2001).

30. A.Wickenden et al., J. Electron. Mater. **29**, 21 (2000).

31. T. B. Wei et al., J. of Crys. Growth **314**, 41 (2011).

32. F. A. Ponce, D. Cherns, W. T. Young and J. W. Steeds, Appl. Phys. Lett. **69**, 770 (1996).

33. D. M. Follstaedt, N. A. Missert, D. D. Koleske, C. C. Mitchell and K. C. Cross, Appl. Phys. Lett. **83**, 4797 (2003).

34. R. Datta, M. J. Kappers, J. S. Barnard and C. J. Humphreys, Appl. Phys. Lett. **85**, 3411 (2004).

35. M. A. Crimp, B. A. Simpkin and B. C. Ng, Phil. Mag. Lett. **81**, 833 (2001).

36. J. L. Weyher et al., J. of Crys. Growth **210**, 151 (2000).

37. R. A. Oliver, M. Kappers, J. J. Sumner, R. Datta and C. J. Humphreys, J. of Crys. Growth **289,** 506 (2006).

38. T. Hino et al., Appl. Phys. Lett. **76,** 3421 (2000).

39. C. W. Oatley, J. Appl. Phys. **53**, R1 (1982).

40. J. I. Goldstein et al, *Scanning Electron Microscopy and X-Ray Microanalysis-third edition*, Springer, Newyork (1992).

41. C. W. Oatley, *The Scanning Electron Microscope part I. The instrument*, Cambridge University press, Cambridge (1972).

42. G. R. Booker, *Modern Diffraction and Imaging Techniques in Material Science*, North Holland, Amsterdam, (1970).

43. L. Reimer, *Scanning electron microscopy- Physics of image formation and microanalysis*, Springer, Newyork (1998).

44. D. B. Holt and D. C. Joy, *SEM microcharacterization of semiconductors*, Academic press, London (1989).

45. J. R. A. Cleaver and K. C. A. Smith, Scanning Electron Micro., **49** (1973).

46. C. collix and C. Mory, Biol. Cell **80**, 175, (1994).

47. G.S. Cargill, Nature **286**, 691, (1980).

48. D. G. Daves, Phil.trans. R.Soc. London A **320**, 243 (1986).

49. D. B. Holt, *Quantitative scanning electron microscopy*, academic press, London (1974).

50. B. G. Yacobi and D. B. Holt, *Cathodoluminescence Microscopy of Inorganic Solids*, Plenum press, Newyork (1990).

51. P. Hovington, D. Drouin and R. Gauvin, Scanning **19**, 1, (1997).

52. D. Drouin, P. Hovington and R. Gauvin, Scanning **19**, 20, (1997).

53. P. Hovington, D. Drouin and R. Gauvin, D. C. Joy, and N. Evans, Scanning **19**, 29, (1997).

54. C. Davisson,L.H. Germer, The Physical Review, **30**, 705 (1927).

55. *http://www.nobelprize.org/nobel_prizes/physics/laureates/1937/* (date of access- 09/04/2012).

56. S. Kikuchi, Imperial academy of Japan, **4**, 457, (1928).

57. S. Nishikawa and S. Kikuchi, Nature, **122**, 726, (1928).

58. A. J. Wilkinson, G. Meaden, D. J. Dingley Ultramicroscopy **106**, 307 (2006).

59. A.Winkelmann, C. Trager-Cowan, F. Sweeney, A. P. Day, P. J. Parbrook Ultramicroscopy **107**, 414 (2007).

60. D. C. Look and J. R Sizelove, Phys. Rev. Lett. **82**, 1237 (1999).

61. X. H. Wu *et al*., J Appl. Phys. **80**, 3228 (1996).

62. W. R. Liu, W. F. Hsieh, C. H. Hsu, K. S. Liang and F. S. Chien. J. of Appl. Cryst. **40**, 924 (2007).

63. G. Naresh-Kumar et al., Phys. Rev. Lett., **108**, 135503 (2012).

64. A. P. Laponsky and N. R. Whetten Phys. Rev. Lett., **3**, 510, (1959).

65. A. J. Dekker Phys. Rev. Lett., **4**, 55, (1960).

66. G. R. Booker, A. M. B. Shaw, M. J. Whelan, P. B. Hirsch Phil.Mag., **16**, 1185, (1967).

67. D. G. Coates Phil. Mag., **16**, 1179, (1967).

68. D. C. Joy, D. E. Newbury and D. L. Davidson, J. Appl. Phys. **53**, 81 (1982).

69. D. C. Joy, G. R. Booker, E. O. Fearon and M. Bevis, In 4 th Ann. SEM symposium, Chicago, **497** (1971).

70. D. B. Holt and D. C. Joy, *SEM microcharacterization of semiconductors*, academic press, London (1989).

71. O. C. Wells, *scanning electron microscopy*, McGraw Hill, Newyork (1974).

72. E. M. Schulson, J. Mater. Sci., **12**, 1071 (1977).

73. S. H. Vale, *Micro beam analysis,* San Francisco press, San Francisco (1985)

74. D. R. Clarke, Phil. Mag., **24,** 973, (1971).

75. R**.** M Stern, T. Ichinochawa, S. Takashima, H. Hashimoto, and S. Kimoto, Phil. Mag., **26**, 1495, (1972).

76. M. Pitaval, P. Morin, J. Baudry and G. Fontaine, Emag., **75**, 20, (1975).

77. M. Pitaval, P. Morin, J. Baudry and G. Fontaine, Microsc. Spectrosc. Electron., **2**, 185, (1977).

78. M. Pitaval, P. Morin, J. Baudry, G. Fontaine and E. Vicario, Scanning Electron Microscopy, **b**, 439, (1977).

79. P. Morin, M. Pitaval, D. Besnard and G. Fontaine, Phil. Mag. A, **4**, 511, (1979).

80. A. J. Wilkinson, G. R. Anstis, J. T. Czernuszka, N. J. Long and P. B. Hirsch, Phil. Mag. A **68**, 59, (1993).

81. A. J. Wilkinson and P. B. Hirsch, Micron **28**, 279 (1997).

82. C. Trager-Cowan. et al., Phy. Rev. B **75**, 085301 (2007).

83. Y. N. Picard and M. E. Twigg, J. Appl. Phys. **104**, 124906 (2008).

84. Y. N. Picard et al., Scripta Materialia **61**, 773 (2009).

85. R. J. Kamaladasa et al., Jour. Of Microscopy, **244**, 311, (2011).

86. R. J. Kamaladasa , W. Jiang, Y. Picard Journal of Elec. Mat., **40**, 11, (2011).

87. M. Brunner, H. J. Kohl and H. Niedrig, Beitr. Elektronen Mikroskop. Direktabb. Oberfl., **8**, 230 (1975).

88. M. Brunner Scanning Electron Microscopy, **1**, 385 (1981).

89. D. B. Williams and C. B. Carter. *Transmission electron microscopy: A textbook for materials science*, Springer, New York (2009).

90. R.J. Kamaladasa and Y.N. Picard, Microscopy: Science, Technology, Education and Applications, **4**, 1583 (2011).

91. D. A. Wood, P. J. Parbrook, P. A. Lynch, M. Lada and A. G. Cullis, phys. stat. sol. a **188**, 641 (2001).

92. J. I. Goldstein et al., *Scanning Electron Microscopy and X-ray microanalysis*, Plenum press, New York (1981).

93. J. P. Spencer, C. J. Humphreys and P. B. Hirsch, Phil. Mag., **26**, 193 (1972).

94. B. A. Simpkin and M. A. Crimp, Ultramicroscopy **77**, 65 (1999).

95. L. M. Peng, S. L. Dudarev and M. J. Whelan. *High Energy Electron Diffraction and Microscopy*, Oxford Univ. Press, Oxford (2003).
96. H. Watanabe, N. Kuroda, H. Sunakawa, and A. Usui, Appl. Phys. Lett. **77**, 1786 (2000).
97. N. Osakabe, Y. Tanishiro, K. Yagi, and G. Honjo, Surface Science **102**, 424 (1981).
98. R. A. Oliver, M. Kappers, J. J. Sumner, R. Datta and C. J. Humphreys, J. of Crys. Growth **289**, 506 (2006).
99. W. J. Tunstall, P. B. Hirsch and J. Steeds, Phil. Mag. **97**, 99 (1963).
100. Y. N. Picard *et al*., Appl. Phys. Lett. **91**, 094106 (2007).
101. J. W. P. Hsu, M. J. Manfra, R. J. Molnar, B. Heying, and J. S. Speck, Appl. Phys. Lett. **81**, 79 (2002).
102. B. S. Simpkins, E. T. Yu, P. Waltereit and J. S. Speck, J. Appl. Phys. **94**, 1448 (2003).
103. S. I. Maximenko, *et al*., J. Appl. Phys. **108**, 013708 (2010).
104. S. H. Lim, D. Shindo, H. B. Kang, K. Nakamura, J. of Crys. Growth **225**, 202 (2001).
105. J. W. Edington, *Practical electron microscopy in materials science*, Macmillan, London (1976).
106. E. Ruedl, P. Delavignette and S. Amelinckx, J. Nucl. Mat. **6**, 46 (1962).
107. T. A. Lafford, P. J. Parbrook, and B. K. Tanner, phys. stat. sol. c **1**, 542 (2002).
108. S. Nakumura et al., Jpn. J. Appl. Phys. **35**, 74 (1996).
109. F. A Ponce and D. P. Bour, Nature **386**, 351 (1997).
110. A. Khan, K. Balakrishnan and T. Katona, Nature Photonics **2**, 77 (2008).
111. P. Waltereit et al., Nature, **406**, 865 (2000).

112. J. S. Speck et al., MRS Bulletin, **34**, 304 (2009).

113. Y. J. Sun, O. Brandt, U. Jahn, T. Y. Liu, A. Trampert, S. Croneneberg, S. Dhar and K. H. Ploog J. Appl.Phys. **92,** 5714 (2002).

114. M. D. Craven, F. Wu, A. Chakraborty, B. Imer, U. K. Mishra, S. P. Denbaars and J. S. Speck, Appl. Phys. Lett. **84** 1281(2004).

115. N. Onojima, J. Suda and H. Matsunami ,J. J. Appl.Phys. **41** L1348 (2002).

116. M. B. Mc Laurin, T. E. Mates and J. S. Speck, Appl. Phys.Lett. **86** 262104 (2005).

117. M. D. Craven, S. H. Lim, F. Wu, J. S. Speck and S. P. DenBaars, Appl. Phys. Lett. **81**, 469 (2002).

118. R. Armitrage and H. Hirayama, Appl. Phys.Lett. **92** 092121(2008).

119. T. J. Baker, B. A. Haskell, F. Wu, J. S. Speck and S. Nakamura J. J. Appl. Phys. **45** L154 (2006).

120. R. R. Vanfleet, J. A. Simmons, H. P. Maruska, D. W. Hill, M. M. C. Chou and B. H. Chai, Appl. Phys. Lett. **83**, 1139 (2003).

121. K. Xu, J. Xu, P. Deng, R. Qiu and Z. Fang, phys. stat. sol. (a) **176**, 589 (1999).

122. C. Q. Chen et al., Appl. Phys. Lett. **81**, 3194 (2002).

123. E. Kuokstis et al., Appl. Phys. Lett. **81**, 4130 (2002).

124. Y. J. Sun, O. Brandt and K. H. Ploog, J. Vac. Sci. Tech. B **21**, 1350 (2003).

125. M. D. Reed, O. M. Kryliouk, M. A. Mastro and T. J. Anderson, J. Crys. Growth **274**, 14 (2005).

126. S. Nakamura et al., Science **281**, 956 (1998).

127. K. H. Baik et al., IEEE Photon. Tech. Lett., **22**, 595(2010).

128. J. Kioseoglou et al., J. Appl. Phys. **109**, 083511 (2011).

129. V. M. Kaganer, O. Brandt, A. Trampert, & K. H. Ploog, Phys. Rev. B **72**, 045423 (2005).

130. M. B. Mclaurin et al., Jpn. J. Appl. Phys. **47**, 5429 (2008).

131. M. A. Moram et al., J. Appl. Phys. **105**, 113501 (2009).

132. F. A. Ponce, D. Cherns, W. T. Young, and J. W. Steeds, Appl. Phys. Lett. **69,** 770 (1996).

133. D. M. Follstaedt et al., Appl. Phys. Lett. **83**, 4797 (2003).

134. F. Wu et al., Appl. Phys. Lett. **96**, 231912 (2010).

135. K. Suzuki, M. Ichihara and S. Takeuchi, Jpn. J. Appl. Phys. **33**, 1114 (1994).

136. C. Mauder et al., J. Cryst. Growth **315**, 246 (2011).

137. C. Mauder et al., J. Cryst. Growth **312**, 1823 (2010).

138. K. R. Wang et al., Appl. Phys. Lett **96**, 231914 (2010).

139. R Butte et al., J. Phys. D: Appl. Phys. **40**, 6328 (2007).

140. A. Castiglia, E. Feltin, G. Cosendey, A. Altoukhov, J.-F. Carlin, R. Bute and N. Grandjean, Appl. Phys. Lett. **94**, 193506 (2009).

141. S. Choi, H. J. Kim, Z. Lochner, Y. Zhang, Y. C. Lee, S. C. Shen, J. H. Ryou and R. D. Dupuis Appl. Phys. Lett. **96**, 243506 (2010).

142. M. Gonschorek, J.-F. Carlin, E. Feltin, M. A. Py, and Grandjean, Appl. Phys.Lett. **89**, 062106 (2006).

143. K. Starosta, Phys. Status Solidi A **68**, K55 (1981).

144. M. J. Lukitsch, Y. V. Danylyuk, V. M. Naik, C. Huang, G. W.Auner, L. Rimai, R. Naik, Appl. Phys. Lett. **79**, 632 (2001).

145. M. Higashiwaki, T. Matsui, J. Cryst. Growth **251**, 494 (2003).

146. Z. T. Chen, Y. Sakai, and T. Egawa Appl. Phys. Lett. **96**, 191911 (2010).

147. X. D. Pu, J. Chen, W. Z. Shen, H. Ogawa, Q. X. Guo, J. Appl. Phys. **98**, 033527 (2005).

148. E. IIopoulos, A. Adikimenakis, C. Giesen, M. Heuken, A. Georgakilas, Appl. Phys. Lett. **92**, 191907 (2008).

149. E. T. Yu, G. J. Sullivan, P. M. Asbeck, C. D. Wang, D. Qiao, and S. S. Lau, Appl. Phys.Lett. **71**, 2794 (1997).

150. G. Cosendey, J-F Carlin, N. A. K. Kaufmann, R.Butte, and N.Grandjean Appl. Phys. Lett. **98**, 181111 (2011).

151. A. Vilalta-Clemente, M. A. Poisson, H. Behmenburg, C. Giesen, M. Heuken, and P. Ruterana Phys. Status Solidi A **1**, 1 (2010).

152. S. Pandey, B. Fraboni, D. Cavalcoli, A. Minj, and A. Cavallini Appl. Phys. Lett. **99**, 012111 (2011).

153. M. Miyoshi, H. Ishikawa, T. Egawa, K. Asai, M. Mouri, T. Shibata, M. Tanaka, and O. Oda Appl. Phys. Lett. **85**, 1710 (2004).

154. Y. Cao and D. Jena, Appl. Phys. Lett. **90**, 182112 (2007).

155. X. H. Wu et al, Appl. Phys.Lett. **72**, 6 (1998).

156. J. Bruckbauer, P. R. Edwards, T. Wang, and R. W. Martin, Appl. Phys. Lett. **98**, 141908 (2011).

157. H. K. Cho, J. Y. Lee, G. M. Yang and C. S. Kim, Appl. Phys. Lett. **79**, 215 (2001).

158. J. W. P. Hsu, M. J. Manfra, R. J. Molnar, B. Heying, and J. S. Speck, Appl. Phys. Lett. **81**, 79 (2002).

159. B. S. Simpkins, E. T. Yu, P. Waltereit and J. S. Speck, J. Appl. Phys. **94**, 1448 (2003).

160. J. Piprek , *Nitride Semiconductor Devices Principles and Simulation*, Weinheim: Wiley-VCH, Berlin (2007).

161. F. Medjdoub, J.F. Carlin, C. Gaquiere, N. Grandjean and E. Kohn, The Open Elec. and Electr. Eng. Jour., **2**, 1 (2008).

162. G. Naresh-Kumar et al., Phys. Stat. Sol. A, **209**, 424 (2012).

163. B. A. Haskell, A. Chakraborty, F. Wu, H. Sasano, P. T. Finl, S. P. Denbaars, J. S. Speck and S. Nakumura, Journal of Elec. Mat., **34**, 4 (2005).

164. D. Kapolnek, S. Keller, R. Vetury, R. Underwood, P. Kozodoy, S. Denbaars, U. Mishra, Appl. Phys. Lett. **71**, 1204 (1997).

165. Y. Kato, S. Kitamura, K. Hiramatsu, N. Sawaki, J.Crystal Growth **144**, 133 (1994).

166. O. Nam, M. Bremser, B. Ward, R. Nemanich, R. Davis, Mat. Res. Soc. Symp. Proc. **449**, 107 (1997).

167. O. Nam, M. Bremser, B. Ward, R. Nemanich, R. Davis, Jpn. J. Appl. Phys. **36**, L532 (1997).

168. H. Sakai, A. Sunakawa, Usui, Appl. Phys. Lett. **73**, 481 (1998).

169. H. Marchand, X. Wu, J. Ibbetson, P. Fini, P. Kozodoy, S. Keller, J. Speck, S. Denbaars, U. Mishra, Appl. Phys. Lett. **73**, 747 (1998).

170. T. Zheleva, O. Nam, M. Bremser, R. Davis, Appl. Phys.Lett. **71**, 2472 (1997).

171. O. Nam, T. Zheleva, M. Bremser, R. Davis, Appl. Phys. Lett. 71 2638 (1997).

172. H. Zhong, M. Johnson, T. McNulty, J. Brown, J. Cook Jr., J. Schetzina, Mater. Internet J. Nitride Semicon. Res. **3**, 6 (1998).

173. Kumano H and Suemune, *Wide Bandgap Semiconductors Fundamental properties and modern photonic and electronic devices*, Springer, Heidelberg (2007).

174. D. Zubia, S. H. Zaidi, S. R. J. Brueck, and S. D. Hersee, Appl. Phys. Lett. **76**, 858 (2000).

175. K.Y. Zang, Y. D. Wang, L.S. Wang, S. Tripathy, S.J. Chua, and C.V. Thompson, Thin Solid Films **515**, 4505 (2007).

176. J. Liang, S.-K. Hong, N. Kouklin, R. Beresford, and J. M. Xu, Appl. Phys. Lett. **83**, 1572 (2003).

177. L.S. Wang, S. Tripathy, B.Z. Wang, and S.J. Chua, Appl. Surf. Sci. **253**, 214 (2006).

178. S. D. Hersee et al., IEEE J. Quantum. Electron. **38**, 1017 (2002).

179. X. Y. Sun, R. Bommena, D. Burckel, A. Frauenglass, M.N. Fairchild, S.R.J. Brueck, G.A. Garrett, M. Wraback, and S.D. Hersee, J. Appl .Phys. **95**, 1450 (2004).

180. P. Shields et al., Phys. Status Solidi C **8**, 2334 (2011).

181. P. Shields et al., Phys. Status Solidi C **9**, 631 (2012).

182. S. Nakamura et al., Appl. Phys. Lett. **72**, 211 (1998).

183. R. W. McClelland, C. O. Bolzer and J. C. C. Fan Appl. Phys. Lett. **37**, 560 (1980).

184. L. Jastrzebski J. Cryst. Growth **63**, 493 (1983).

185. P. Gibart, B .Beaumont and P. Vennegues 2003 *Nitride Semiconductors handbook on materials and devices* Edited by Ruterana P, Albrecht M, J. Neugebauer, Wiley-VCH, Weinheim (2003).

186. D. Zubia and S. D. Hersee, J. Appl. Phys. **85**, 6492 (1999).

187. T.-Y. Tang, C.-H. Lin, Y.-S. Chen, W.-Y. Shiao, W.-M. Chang, C.-H. Liao, K.-C. Shen, C.-C. Yang, M.-C. Hsu, J. - H. Yeh, and T.-C. Hsu, IEEE Trans. Electron Dev. **57**, 1 (2010).

188. T. S. Zheleva, W.M. Ashmawi, and K. A. Jones, Phys. Stat. Sol. (a) **176**, 545 (1999).

189. I. H. Kim, C. Sone, O. H. Nam, Y. J. Park, and T. Kim, Appl. Phys. Lett. **75**, 4109 (1999).

190. R. F. Davis, T. Gehrke, K. J. Linthicum, T. S. Zheleva, E. A. Preble, P. Rajagopal, C. A. Zorman, and M. Mehregany, J. Cryst. Growth **225**, 134 (2001).

191. R. F. Davis, T. Gehrke, K. J. Linthicum, P. Rajagopal, A.M. Roskowski, T. Zheleva, E. A. Preble, C. A. Zorman, M. Mehregany, U. Schwarz, J. Schuck, and R. Grober, MRS Internet J. Nitride Semicond. Res. **6**, 14 (2001).

192. C. Liu, W. N. Wang, S. Denchitcharoen, A. Gott, P. A. Shields, and D. W. E. Allsopp, Phys. Status Solidi C **6**, S527 (2009).

193. S. D. Lester, F. A. Ponce, M. G. Craford, and D. A. Steigerwald, Appl. Phys. Lett. **66**, 1249 (1995).

194. O. Ueda, S. Isozumi, T. Kotani, and T. Yamaoka, J. Appl. Phys. **48**, 3950 (1977).

195. P. M. Petroff, O. G. Lorimor, and J. M. Ralston, J. Appl. Phys. **47**, 1583 (1976).

196. B. G. Yacobi and D. B. Holt, *Cathodoluminescence microscopy of inorganic solids*, Plenum press, New York (1990).

197. M. R. Philips, Microchim. Acta **155**, 51 (2006).

198. C. M .Parish and P. E. Russell, *Advances in imaging and electron physics*, Elsevier Amsterdam (2007).

199. D. B. Holt and D. C. Joy, *SEM microcharacterization of semiconductors*, academic press, London (1989).

200. S. M. Davidson J. Microscopy, **110**, 177 (1977).

201. P. M. Petroff, R. A. Logan and A. Savage J. Microscopy, **118**, 255 (1980).

202. D. B. Holt and F. M. Saba , Scanning electron microscopy, **3**, 1023 (1985).

203. K. Lohnert and E. Kubalek Phys. Stat. sol A , **79**, 131(1984).

204. M. Albrecht et al, Appl. Phys. Lett. **92**, 231909 (2008).

205. E. G. Brazel, M. A. Chin, and V. Narayanamurti, Appl. Phys. Lett. **74**, 2367 (1999).

206. K. X. Chen et al., Appl. Phys. Lett. **93**, 192108 (2008).

207. T. Sugahara et al, Jpn. J. Appl. Phys., **37**, 398 (1998).

208. I. Arslan and N. D. Browning, Phys. Rev. B **65**, 075310 (2002).

209. J. Kioseoglou et al. J. Appl. Phys. **110**, 053715 (2011).

210. R. W. Martin, P. R. Edwards, K. P. O'Donnell, M. D. Dawson, C.-W. Jeon, C. Liu, G. R. Rice, and I. M. Watson, phys. stat. sol. a **201**, 665 (2004).

211. M. A. Falkenberg, H. Schuhmann, M. Seibt, and V. Radisch, Rev. Sci. Instrum. **81**, 063705 (2010).

212. S. D. Bakshi, J. Sumner, M. J. Kappers and R. A. Oliver, J. of Crys. Growth **311**, 232 (2009).

213. J. Christen, M. Grundmann and D. Bimberg, J. Vac. Sci.Technol. B **9**, 2358 (1991).

214. P. R. Edwards and R. W. Martin, Semicond. Sci.and Technol. **26**, 064005 (2011).

215. C. M .Parish and P. E. Russell, *Advances in imaging and electron physics***,** Elsevier, Amsterdam (2007).

216. K. J. Lethy, *Characterisation of nanostructured light emitters*, PhD thesis, University of Strathclyde (2012).

217. N. Yamamoto, H. Itoh, and V. Grillo, S. F. Chichibu, S. Keller, J. S. Speck, S. P. DenBaars, U. K. Mishra, S. Nakamura, and G. Salviati, J. Appl. Phys. **94**, 4315 (2003).

218. E. Meissner, S. Schweigard, J. Friedrich, T. Paskova, K. Udwary, G. Leibiger, F. Habel. J. of Crys. Growth **340**, 78 (2012).

219. S. W. Lee et al, Appl. Phys. Lett. **94**, 082105 (2009).

220. Y. N. Picard et al., Microscopy Today, **20**, 12 (2012).

Appendix A: List of Figures

Figure 2.7: (a) Experimental ECP [same as that shown in Fig. 2.3b], (b) Dynamical simulation of ECP and (c) kinematical simulation of ECP from c–GaN (for incident electron beam energy of 30 keV).

Figure 2.8: 2–beam ECC image and ECP revealing dislocation types: (a) & (b) show electron channelling contrast images from the same part of the sample acquired at g of (31–4–3) and (–1–34–3), respectively. The circle indicates a screw dislocation, the rectangle an edge dislocation, and the octagon a mixed dislocation. The black and white arrows highlight the change of contrast for sub grains when g is changed. (c) & (d) show the ECPs which correspond to the ECC images shown in (a) & (b). The cross shows the position of the PC, the black dotted lines highlight the diffracting planes and the red arrow shows the direction of g.

Figure 2.9: Possible B–W contrast directions for TDs: High magnification electron channelling images showing B–W contrast directions for screw (a-d), edge (e-f) and mixed (g-h) dislocations. (i-k) shows the possible directions of the B–W contrast of screw (i), edge (j) and mixed dislocations (k) for a g of (3 1 -4 -3). The dotted red arrow denotes the direction of g.

Figure 2.10: Six B–W contrast directions for edge dislocations for the given g. The red arrow denotes the direction of g.

Figure 2.11: Twelve B–W contrast directions for mixed dislocations for the given g. The red arrow denotes the direction of g.

Figure 3.1: Possible GaN growth alignments on γ–$LiAlO_2$. Note that the diagram also shows it is possible for c–plane nitrides growth on γ–$LiAlO_2$.

Figure 6.4: (a) Electron channelling contrast image of GaN thin film revealing TDs and areas of different tilt and rotation of the crystal and are seen as regions with different grey scales (grains). (b) The inset shows a magnification of the marked TD displaying the typical B–W contrast for a TD. The area of the inset is 500×500 nm^2 area.

Figure 6.5: (a) Peak intensity map and (b) CL energy map of the GaN near band edge emission acquired at 5 KeV. The CL maps were gained by numerically fitting each individual spectrum in the hyperspectral data set using a pseudo–Voigt function for the GaN emission peak. TDs are shown as dark spots of reduced intensity. The energy map (b) reveals small shifts in energy due to strain variations or doping in the sample.

Figure 6.6: (a) Electron channeling images and (b) CL intensity imaging from the same micron–scale area. TDs appearing as spot with B–W contrast in ECCI appear as dark spots in CL revealing a direct correlation of TDs between both techniques.

Appendix B: List of tables

Appendix C: Publications

1. G. Naresh- Kumar et al, “Imaging and identifying defects in nitride semiconductor thin films using a scanning electron microscope”, *Phys. Status Solidi A*, 1–3 (2012).
2. G. Naresh- Kumar et al, “Rapid nondestructive analysis of threading dislocations in wurtzite materials using the scanning electron microscope”, *Phys. Rev. Lett.*,108, 135503 (2012).
3. G. Naresh- Kumar et al, “Imaging stacking faults and partial dislocations by electron channeling contrast imaging in a scanning electron microscope”, *under review in Phy. Rev. B* (2012).
4. G. Naresh- Kumar et al, “Combing electron channeling and cathodoluminescence using scanning electron microscopy”, *manuscript under preparation* (2012).

Patents:

1. Carol Trager-Cowan et al, “Rapid, non-destructive analysis of threading dislocations in wurtzite materials using the scanning electron microscope” (*GB1111272.9, submitted on July 2011*)

Appendix D: Conferences and meetings

Poster presentation:

1. G. Naresh-Kumar et al., “Electron Channelling Contrast Imaging of Defects in Nitride Semiconductor Thin Films”, EMRS, Poland, September 2009.
2. G. Naresh-Kumar et al., “Structural analysis of InAlN heterostructures using electron channelling contrast imaging in a scanning electron microscope”, ICNS 9, Scotland, July 2011.
3. G. Naresh-Kumar et al., “Applications of electron channelling contrast imaging for characterizing nitride semiconductor thin films in a scanning electron microscope”, UKNC, England, July 2012.

Oral presentation:

1. G. Naresh-Kumar et al., “Structural Analysis of InAlN/AlN/GaN hetrostructures and m-plane GaN using Electron Channelling Contrast Imaging, Atomic Force Microscopy and Transmission Electron Microscopy”, RMS-EBSD, England, March 2010.
2. G. Naresh-Kumar et al., “Structural Analysis of InAlN/AlN/GaN hetrostructures and m-plane GaN using Electron Channelling Contrast Imaging, Atomic Force Microscopy and Transmission Electron Microscopy”, BIAMS, Germany, July 2010.

3. G. Naresh-Kumar et al., “Structural characterisation of InAlN/AlN/GaN heterostructures for high electron mobility transistors”, UKNC, England, January 2011.
4. G. Naresh-Kumar et al., “Correlating structural and luminescence properties of nitride semiconductor structures using electron channelling contrast imaging and cathodoluminescence hyperspectral imaging”, RMS-EBSD, Germany, March 2011.
5. G. Naresh-Kumar et al., “Structural analysis of InAlN heterostructures using electron channelling contrast imaging in a scanning electron microscope”, EMRS, France, May 2011.
6. G. Naresh-Kumar et al., “Structural, luminescence and electrical characterisation of InAlN/AlN/GaN heterostructures”, MRS, Boston, USA, November 2011.
7. G. Naresh-Kumar et al., “Applications of electron channelling contrast imaging for characterising nitride semiconductor thin films”, UKNC, England, January 2012.
8. G. Naresh-Kumar et al., “Applications of electron channelling contrast imaging for characterising nitride semiconductor thin films”, RMS-EBSD, England, March 2012.